Translation efficiency covariation across cell types is a conserved organizing principle of mammalian transcriptomes

Yue Liu[a], Shilpa Rao[a], Ian Hoskins[a], Michael Geng[a], Qiuxia Zhao[a], Jonathan Chacko[a], Vighnesh Ghatpande[a], Kangsheng Qi[a], Logan Persyn[a], Jun Wang[b], Dinghai Zheng[b], Yochen Zhong[a], Dayea Park[a], Elif Sarinay Cenik[a], Vikram Agarwal[b] , Hakan Ozadam[a,c], Can Cenik*

Affiliations:

[a] Department of Molecular Biosciences, University of Texas at Austin, Austin, TX 78712, USA

[b] mRNA Center of Excellence, Sanofi, Waltham, MA 02451, USA

[c] Present address: Sail Biomedicines, Cambridge, MA, 02141, USA

* Corresponding author**:** ccenik@austin.utexas.edu

ABSTRACT

Characterization of shared patterns of RNA expression between genes across conditions has led to the discovery of regulatory networks and novel biological functions. However, it is unclear if such coordination extends to translation, a critical step in gene expression. Here, we uniformly analyzed 3,819 ribosome profiling datasets from 117 human and 94 mouse tissues and cell lines. We introduce the concept of *Translation Efficiency Covariation* (TEC), identifying coordinated translation patterns across cell types. We nominate potential mechanisms driving shared patterns of translation regulation. TEC is conserved across human and mouse cells and helps uncover gene functions. Moreover, our observations indicate that proteins that physically interact are highly enriched for positive covariation at both translational and transcriptional levels. Our findings establish translational covariation as a conserved organizing principle of mammalian transcriptomes.

Keywords: Translation efficiency, Translational regulation, Ribosome profiling, Translation efficiency covariation, Gene functions, Regulatory networks

INTRODUCTION

In the last three decades, technological advances have progressively revealed the expression of RNAs with increasing spatial and cellular resolution[1–7]. These measurements have spurred conceptual advances, driven by computational approaches. Foremost among these is the concept of RNA co-expression, which quantifies the similarities in RNA expression changes among groups of genes across conditions[8–11].

RNA co-expression analysis across biological contexts reveals shared biological functions, informing us about underlying mechanisms and interactions[12–15]. By applying the principle of guilt-by-association, new functions for genes with previously unknown roles can be inferred by the similarity of RNA expression patterns with genes of known function[9,12,16]. Furthermore, RNA co-expression between transcripts is predictive of protein-protein interactions[17,18], and can indicate genes that are likely regulated by the same transcription factors, suggesting common regulatory mechanisms[19,20].

These findings suggest that RNA co-expression may serve as a proxy for the proteomic organization of cells. However, it is only recently that quantification of protein abundance across numerous cell types and conditions has become possible, allowing this assumption to be explicitly tested. Mass spectrometry-based measurements across hundreds of cell types have revealed that proteins similarly exhibit shared patterns of abundance, organized according to their functions and physical interactions[21–23]. Surprisingly, much of the proteome-level organization of co-abundance patterns are not detected at the RNA level[21,22]. Furthermore, physically interacting proteins are much more likely to have coordinated protein abundance than RNA co-expression[21,22,24]. RNA co-expression in both mouse and human cells often arises from the chromosomal proximity of genes even when they are functionally unrelated[25,26]. This likely unproductive co-expression pattern is absent at the protein level[27,28], suggesting that post-transcriptional regulation plays a significant role in proteome organization.

Translation regulation, a crucial post-transcriptional process, may bridge this gap, given its vital roles in development, maintaining cellular homeostasis, and responding to environmental changes[29–35]. There are three lines of evidence that suggest the possibility of coordinated translation of functionally and physically associated proteins across different biological contexts.

First, mammalian mRNAs bind various proteins to form ribonucleoproteins that influence their lifecycle from export to translation[36]. The set of proteins interacting with an mRNA varies with time and context, significantly altering the duration, efficiency, and localization of protein production. These observations led to the proposal of the post-transcriptional RNA regulon model over two decades ago, positing that functionally related mRNAs are regulated together post-transcriptionally[37,38]. Supporting this model, Puf3, a Pumilio family member in yeast, represses the translation of sequence-specific mRNAs encoding mitochondrial proteins[38]. Similarly, in human cells, CSDE1/UNR regulates the translation of mRNAs involved in epithelial-to-mesenchymal transition[39]. However, it remains to be determined if translation of functionally related mRNAs is coordinately regulated across different conditions.

Second, in both *E. coli* and yeast, proteins within multiprotein complexes are synthesized in

stoichiometric proportions needed for assembly[40,41]. This translational regulation likely tunes protein production to minimize the synthesis of excess protein components that would otherwise need to be degraded[42]. However, in human cells, evidence of such proportional synthesis is reported for only two complexes: ribosomes[41,43] and the oxidative phosphorylation machinery[44]. Furthermore, these observations have been made in a very limited number of cell lines, which limits the generalizability of this concept across diverse cell types and other functionally related protein groups.

Third, the formation of many protein complexes is facilitated by the co-translational folding of nascent peptides[40,41,45,46]. For instance, in bacteria, the anti-Shine-Dalgarno sequence induces translational pausing to modulate the co-translational folding of nascent peptides[46]. Co-translational assembly ensures that protein subunits are synthesized near each other, enabling near concurrent interactions, which are crucial for the biogenesis of some complex protein structures[47]. Recent evidence indicates that co-translational assembly may also be relatively common in human cells[48].

Co-translational assembly and stoichiometric synthesis rates of protein complexes suggest coordinated translation of several mRNAs within a given cell type. However, due to the lack of robust, transcriptome-wide translational efficiency (TE) measurements across diverse biological conditions, it remains to be seen whether such coordination extends across different cell types or conditions. To address this, we analyzed thousands of matched ribosome profiling and RNA-seq datasets from >140 human and mouse cell lines and tissues. To quantify the similarity of translation efficiency patterns of transcripts across cell types and tissues, analogously to RNA co-expression, we introduce the concept of Translation Efficiency Covariation (TEC). based on a compositional data analysis approach[49,50] Our findings demonstrate that TEC can reveal gene functions not identified through RNA co-expression analysis alone and uncovered shared motifs for RNA binding proteins (RBPs) among genes exhibiting TEC. Physically interacting proteins are highly enriched for both TEC and RNA co-expression. Further supporting the functional significance of this concept, TEC among genes is highly conserved between humans and mice.

RESULTS

Integrated analysis of thousands of ribosome profiling and RNA-seq measurements enable quantitative assessment of data quality

We undertook a comprehensive, large-scale meta-analysis of ribosome profiling data to quantify TE across different cell lines and tissues. We collected 2,195 ribosome profiling datasets for humans and 1,624 experiments for mice, along with their metadata (Fig. 1a; Methods). Given that metadata is frequently reported in an unstructured manner and lacks a formal verification step, we conducted a manual curation process to rectify inaccuracies and collect missing information, such as experimental conditions and cell types used in experiments. One crucial aspect of our manual curation was pairing between ribosome profiling and corresponding RNA-seq when possible. Overall, 1,282 (58.4%) human and 995 (61.3%) mouse ribosome profiling samples were matched with corresponding RNA-seq data (table S1). The resulting curated metadata facilitated the uniform processing of ribosome profiling and corresponding RNA-seq data using an open-source

pipeline[51]. We call the resulting repository harboring these processed files RiboBase (table S1).

In RiboBase, the top cell types with the most experiments were HEK293T (13.1%) and HeLa (8.1%) for human; in mouse, the leading tissues were brain (9.6%), embryonic fibroblasts (8.3%), and liver (7.7%) (Fig. 1b; table S1). The median number of sequencing reads for ribosome profiling samples was ~43.2 million for humans and ~37.5 million for mice, respectively (ExtendedDataFig. 1a-b; table S2-3; supplementary text). A majority of reads contained adapter sequences included during library preparation (with medians of 82.2% and 79.2% of total reads having adapters for human and mouse, respectively). Due to the substantial presence of ribosomal RNA in ribosome profiling datasets, only around 15% of total reads aligned to the transcript reference (ExtendedDataFig. 1c-d; table S4-5; supplementary text).

The length of ribosome-protected mRNA footprints (RPFs) provides valuable information about data quality, the experimental protocol used, and translational activity[52]. The choice of nuclease impacts the resulting read length distribution of RPFs[53] (ExtendedDataFig. 2a-b). In agreement, we found that the peak position and range of RPF lengths were closely associated with the type of digestion enzymes used in human cancer samples (Fig. 1c). To account for the variability of RPF length distributions across the compendium of experiments, we developed a module that allowed for setting sample-specific RPF read length cutoffs (ExtendedDataFig. 3a; Methods). This dynamic approach proved more effective than using fixed minimum and maximum values for RPF lengths, resulting in a higher retrieval of usable reads (median increase of 10.8% for human and 17.1% for mouse) and an increased proportion of reads within the coding sequence (CDS) region (ExtendedDataFig. 3b).

After selecting a set of RPFs, we assessed the quality of ribosome profiling data within RiboBase using two additional criteria. Given that translating ribosomes should be highly enriched in annotated coding regions, we require that at least 70% of RPFs should be mapped to the CDS. We found that 160 human and 115 mouse samples failed to meet this criterion (Fig. 1d; table S6-7). Subsequently, we required a minimum number of RPFs that map to CDS to ensure sufficient coverage of translated genes (Methods). There were 318 human and 431 mouse samples with less than 0.1X transcript coverage (Fig. 1e; table S6-7). Altogether, 1,794 human samples and 1,134 mouse samples were retained for in-depth analysis. Of these, 1,076 human and 845 mouse samples were paired with matching RNA-seq data. Our results indicate a considerable fraction of publicly available ribosome profiling experiments had suboptimal quality (18.3% of the human and 30.1% of the mouse samples) (Fig. 1f). Interestingly, the data quality appeared to be independent of time (ExtendedDataFig. 4). Additionally, we found that samples that passed our quality thresholds were more likely to exhibit three-nucleotide periodicity compared to those that failed quality control (92.59% vs 78.30% for humans and 91.36% vs 86.73% for mice; ExtendedDataFig. 5; Methods). These findings underscore the necessity of meticulous quality control for the selection of experiments to enable large-scale data analyses.

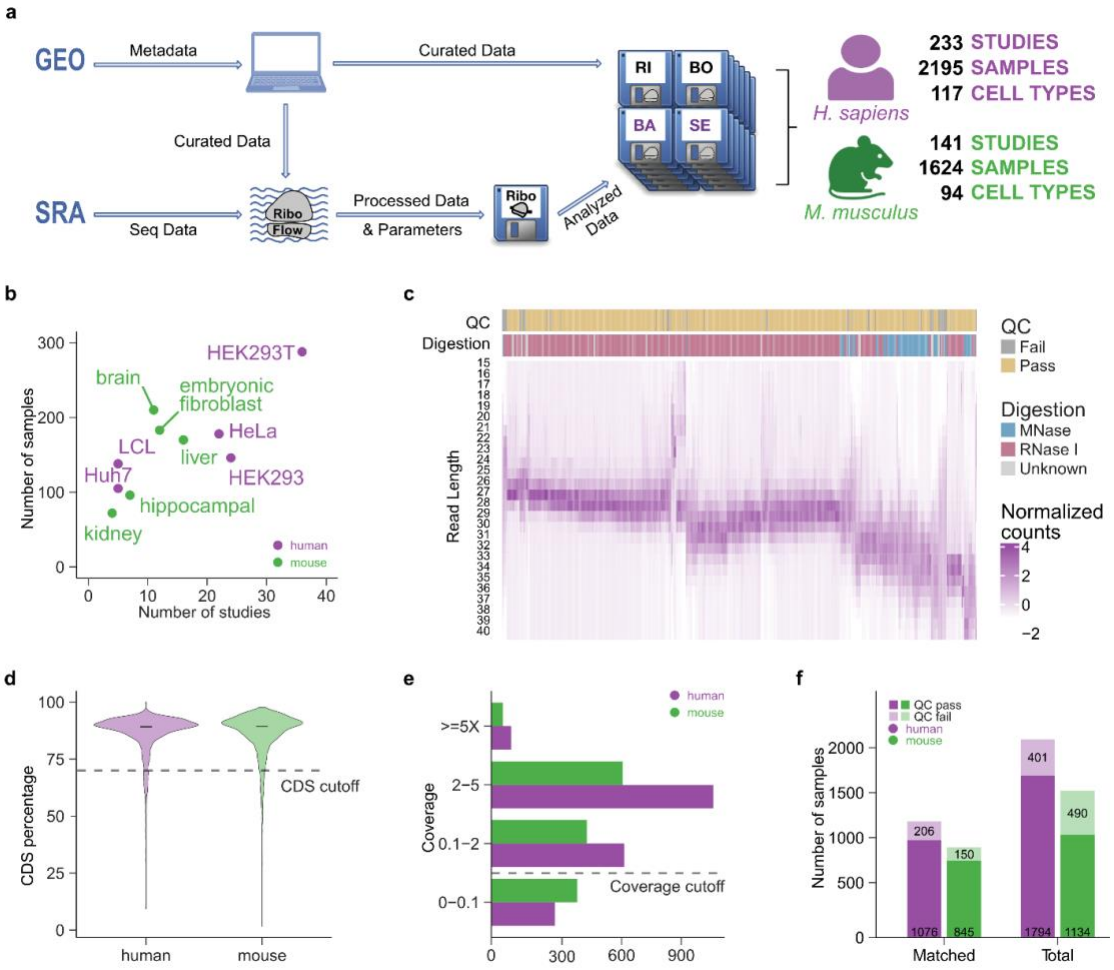

Fig. 1 | RiboBase: a comprehensive ribosome profiling database with thousands of experiments. a, Schematic of RiboBase. We manually curated metadata and processed the sequencing reads using a uniform pipeline (RiboFlow[51]). **b,** Top five most highly represented cell lines or tissues with respect to the number of experiments were plotted. **c,** We determined the ribonuclease used to generate ribosome profiling data for 680 experiments using human cancer cell lines. For each experiment, the read length distribution of RPFs mapping to coding regions was visualized as a heatmap. The color represents the z-score adjusted RPF counts (Methods). Each experiment where the percentage of RPFs mapping to CDS was greater than 70% and achieving sufficient coverage of the transcript (>= 0.1X) was annotated as QC-pass (Methods). **d,** For the 3,819 ribosome profiling experiments in RiboBase, we applied a function to select the range of RPFs for further analysis (Methods). We calculated the proportion of the selected RPFs that map to the coding regions (y-axis). The horizontal line represents the median of the distribution. **e,** Experiments (x-axis) were grouped by the transcript coverage (y-axis). **f,** Among

the ribosome profiling experiments in RiboBase, 2,277 of them had corresponding RNA-seq data (matched). The number of samples that pass quality controls was plotted.

Translation efficiency is conserved across species and is cell-type specific

Ribosome profiling measures ribosome occupancy, a variable influenced by both RNA expression and translation. Thus, estimating translation efficiency necessitates analysis of paired RNA-seq and ribosome profiling data. To assess accurate matching in RiboBase, we first compared the coefficient of determination (R^2) between matched ribosome profiling and RNA-seq data to that from other pairings within the same study. As would be expected from correct matching, we found that matched samples had significantly higher similarity on average (Fig. 2a; Welch two-sided t-test p-value = 2.2×10^{-16} for human and p-value = 2.1×10^{-5} for mouse). We then implemented a scoring system to quantitatively evaluate the correctness of our manual matching information (Methods). 99.2% of human samples and 98.5% of mouse samples had a sufficiently high matching score, demonstrating the effectiveness of our manual curation strategy (ExtendedDataFig. 6a; Methods).

Using the set of matched ribosome profiling and RNA-seq experiments, we next quantified TE, which is typically defined as the ratio of ribosome footprints to RNA-seq reads, normalized as counts per million[54]. However, this approach leads to biased estimates with significant drawbacks[55]. To address this limitation, we calculate TE based on a regression model using a compositional data analysis method[49,50,56], avoiding the mathematical shortcomings of using the canonical log-ratio method (Fig. 2b; ExtendedDataFig. 6a-c, 7; table S8-11; Methods; supplementary text).

We next assessed whether measurement errors due to differences in experimental procedures dominate variability that would otherwise be attributed to biological variables of interest. Specifically, we compared similarities between experiments that used the same cell type or tissue in different studies (ExtendedDataFig. 8a). We found that ribosome profiling or RNA experiments from the same cell type or tissue exhibited higher similarity compared to those from different cell lines or tissues (Fig. 2c). Consistent with this observation, TE values displayed higher Spearman correlation coefficient within the same cell type or tissue (median correlation coefficient of 0.56 and 0.53 in human and mouse, respectively) compared to different cell lines and tissues (median correlation coefficient of 0.49 and 0.45 in human and mouse, respectively) (Fig. 2d).

We expected that a more accurate estimate of TE would show a stronger correlation with protein abundance. We calculated for each transcript the cell type-specific TE by taking the average of TE values across all experiments conducted with that particular cell line. Indeed, our results show that compared to the canonical definition, the TE derived using the regression approach with winsorized read counts (ExtendedDataFig. 8b; ExtendedDataFig. 9-11; supplementary text) is more strongly correlated with protein abundance in seven cancer cell lines (mean Spearman correlation coefficient of 0.465 vs 0.219; Fig. 2e).

Furthermore, TE measurements from cell lines and tissues with the same biological origin (e.g., blood) tended to cluster together, supporting the existence of cell-type-specific in addition to species-specific differences in TE (Fig. 2f). As expected, mean ribosome occupancy and RNA

expression across cell types showed a strong correlation (Spearman correlation: ~0.8), yet mean TE was only weakly associated with RNA expression (Spearman correlation: ~0.2) (Fig. 2g). Taken together, our analyses demonstrate that our compositional regression-based approach to calculating TE ensures more accurate measurements across different cell types and conditions.

Measurements of TE in two species across a large number of cell types enabled us to investigate the conservation of TE, ribosome occupancy, and RNA expression. Transcriptomes, ribosome occupancy, and proteomes exhibit a high degree of conservation across diverse organisms[57,58]. Consistently, we found average ribosome occupancy, RNA expression, and TE across different cell lines and tissues were highly similar between orthologous genes in human and mouse (Fig. 2g; table S12). Specifically, the Spearman correlation coefficient of mean TE across cell types and tissues between human and mouse was 0.9 (Fig. 2h), which is comparable to the mean RNA expression correlation between human and mouse (~0.86, ExtendedDataFig. 12a). Using a 95% prediction interval to identify outlier genes, we found that outlier genes with higher mean TE in humans compared to mice were enriched in the gene ontology term 'RNA binding function' (Fig. 2i). In contrast, genes with elevated mean TE in mice were enriched for having functions related to extracellular matrix and collagen-containing components (Fig. 2i). The enrichment of genes with higher TE in mice, particularly those from the extracellular matrix and collagen-containing components, may be due to the fact that many samples in mouse studies are derived from the early developmental stage[59].

Despite the high correlation of mean TE across various cell lines and tissues between human and mouse, TE distinctly exhibits cell-type specificity. While several studies compared the conservation of TE between the same tissues of mammalians or model organisms[58,60,61], our dataset uniquely enabled us to determine the conservation of variability of TE for transcripts across different cell types. Intriguingly, we observed a moderately high similarity between the variability of TE of orthologous genes in human and mouse (Spearman partial correlation coefficient = 0.63; Fig. 2j; ExtendedDataFig. 12b-d; Methods). Our results reveal that certain genes exhibit higher variability of TE across cell types and this is a conserved property between human and mouse.

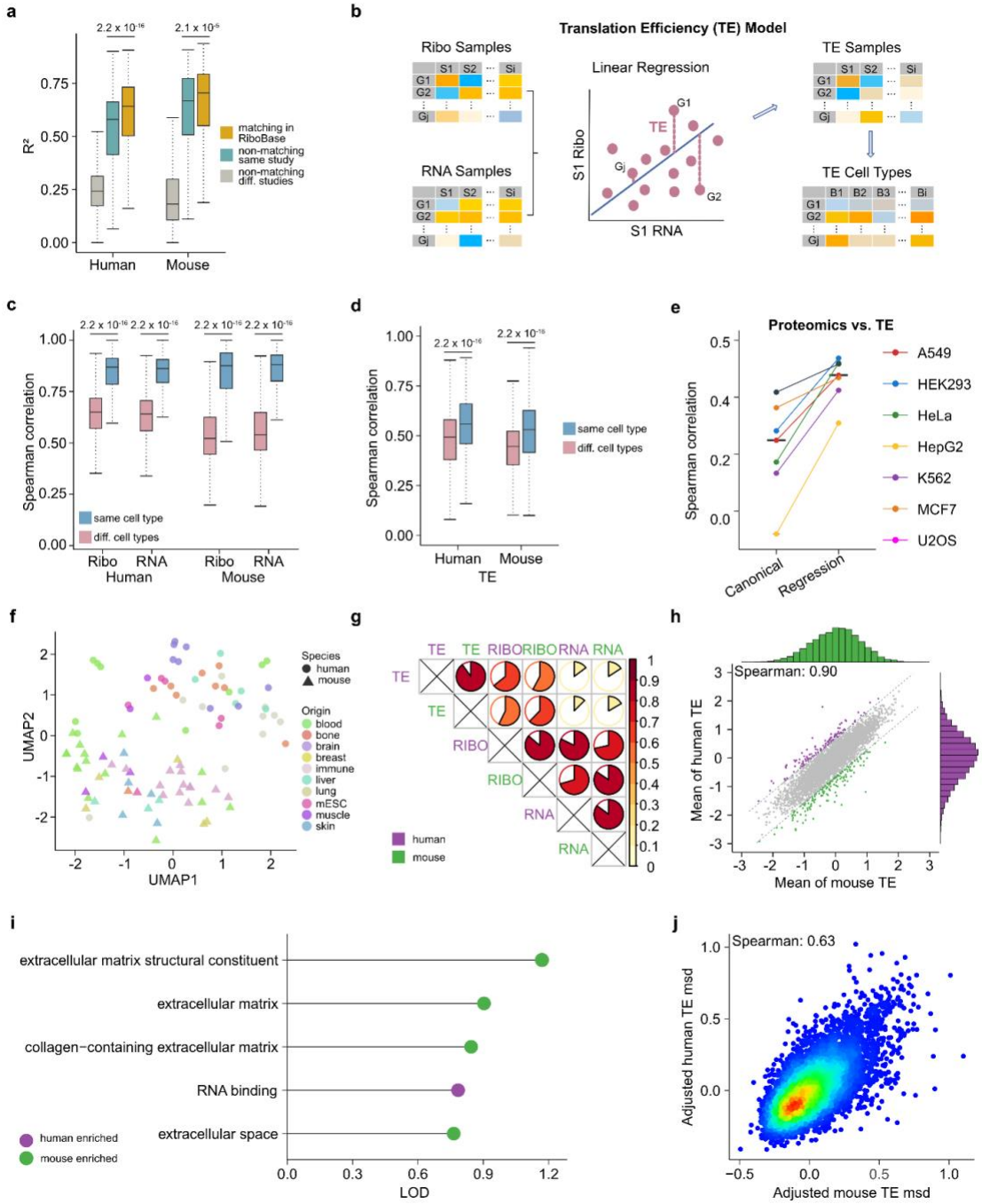

Fig. 2 | TE defined using a compositional linear regression model is conserved across cell types and species. a, The distribution of coefficient of determination (R^2, y-axis) between ribosome profiling data and RNA-seq in RiboBase was compared to random matching within the same study and across different studies. In each figure panel containing boxplots, the horizontal line corresponds to the median. The box represents the interquartile range (IQR) and the whiskers

extend to the largest value within 1.5 times the IQR. The significant p-value shown in this figure was calculated using the two-sided Wilcoxon test. **b,** Schematic of TE calculation using the linear regression model with compositional data (CLR transformed; Methods; ExtendedDataFig. 7). **c,** Distribution of correlations of TE (linear regression model) across experiments. **d,** The distribution of Spearman correlations between experiments (y-axis) was calculated based on whether they originated from identical or different cell lines or tissues.**e,** Correlation between TE and protein abundance from seven human cell lines[62] was calculated using log-ratio of ribosome profiling and RNA expression or compositional regression method. The horizontal line corresponds to the median. **f,** We used UMAP to cluster the TE values of all genes across different cell types, c onsidering only those origins with at least five distinct cell types. **g,** The Spearman correlation of 9,194 orthologous genes between human and mouse across TE, ribosome profiling, and RNA-seq levels. The circles represent the value of the Spearman correlation between groups. **h,** TE values were averaged across cell types and tissues for either human and mouse. Each dot represents a gene, and a 95% prediction interval was plotted to identify outlier genes (highlighted in purple and green). **i,** We conducted GO term enrichment analysis for outlier genes from panel H. We ranked the GO terms (y-axis) by the logarithm of the odds (LOD; x-axis). **j,** The correlation of the standard deviation of TE (quantified with adjusted metric standard deviation (msd); Methods; ExtendedDataFig. 12c-d) for orthologous genes across different cell types between human and mouse.

Translation efficiency covariation (TEC) is conserved between human and mouse

Uniform quantification of TE enabled us to investigate the similarities in TE patterns across cell types. Given the usefulness of RNA co-expression in identifying shared regulation and biological functions, we aimed to establish an analogous method to detect patterns of translation efficiency similarity among genes. To achieve this, we employed the proportionality score (rho)[50,56], a statistical method that quantifies the consistency of how relative TE changes across different contexts (Methods). Recent work suggested that the proportionality score enhances cluster identification in high-dimensional single-cell RNA co-expression data[10]. Consistent with these findings, our analysis revealed its particular effectiveness in quantifying ribosome occupancy covariation (ExtendedDataFig. 13; Methods). We calculated rho scores for all pairs of human or mouse genes where a high absolute rho score indicates significant translation efficiency covariation (TEC) between pairs (Fig. 3a).

Previous studies have indicated that RNA co-expression between genes is conserved in mammals[57,63,64]. To assess the potential evolutionary significance of the newly introduced TEC concept, we evaluated its conservation across human and mouse transcripts. Indeed, TEC was highly similar for orthologous gene pairs in humans and mice (Fig. 3b, Pearson correlation coefficient 0.41), compared to a negligible correlation in TEC derived from shuffled TE values (ExtendedDataFig. 14, Pearson correlation coefficient 0.00022). Our findings imply that translation efficiency patterns are evolutionarily preserved, paralleling the conservation of RNA co-expression.

There are few known examples of transcript sets with shared translational control across cell types, including those with 5′ terminal oligopyrimidine (TOP) motifs[65] and transcripts regulated by

CSDE1[39]. We hypothesized that these sets of transcripts would exhibit significantly higher TEC compared to a control set, and this was indeed observed (Extended Data Fig. 15a; Wilcoxon p-value < 2.2e-16). These findings highlight that TEC effectively captures previously established patterns of shared translational regulation among transcripts.

RNA co-expression analyses led to the discovery of regulatory motifs and shared transcription factor binding sites[66]. We hypothesized that TEC among genes may nominate RNA binding proteins (RBPs) as potential drivers of TEC[67]. We identified groups of transcripts whose TE is correlated with the RNA expression of experimentally determined RBPs[68] (1274 human and 1762 mouse RBPs; Methods; https://zenodo.org/uploads/11359114). We refer to transcripts whose TE is significantly correlated with an RBP's expression as the RBP's TE regulon. We note that a RBP's broader regulon may include genes that are affected at the level of RNA synthesis, stability, and RNA and protein modifications.

Interestingly, some RBP TE regulons were dominated by positive or negative correlations (Fig. 3c-d). For example, the RNA expression of ZC3H10 has largely positive correlations with TE (71% of RBP TE regulon) (Fig. 3c). Conversely, the RNA expression of subunits of ubiquinone oxidoreductase (Ndufa7, Ndufv3) is negatively correlated with TE for many genes in mice (Fig. 3c). We found that the RNA expression of ribosomal protein genes is negatively correlated with TE of many other transcripts (https://zenodo.org/uploads/11359114). This may indicate that transcriptome-wide TE is tempered during ribosome biogenesis, perhaps as a result of competition for ribosomes and other biosynthetic resources (tRNAs, amino acids) devoted to synthesizing new ribosomal proteins. Given the high abundance of ribosomal protein genes and their coordinated translational regulation[69], this result may reflect the impact of global differences in translation on measured TE.

To identify evolutionarily conserved RBP TE regulons, we examined the intersection of significant RBP-gene correlations between human and mouse. At least some activating RBP functions may be evolutionarily conserved, as there was a correspondence between human and mouse in the proportion of TE regulon genes with positive correlations (Pearson correlation 0.44; Fig. 3d). To nominate RBPs that may modulate TE, we calculated the proportionality score of genes in each TE regulon and selected regulons that had high absolute scores, reasoning that directional impacts on TE might be more likely if the RBP engages these transcripts. We found 85 RBPs where genes in the RBP's TE regulon had high TEC (mean absolute pairwise rho >90th percentile; ExtendedDataFig. 15b; supplementary text). Some of these RBPs were previously recognized as regulators of TE, including VIM[70], a transcript whose own TE is likely controlled via its 5′TOP motif [65,71]. However, we were unable to independently validate three such putative TE regulons (ExtendedDataFig. 16), which may be due to several limitations including cell-type specificity, efficiency of knockout, and limited replicates (supplementary text). Taken together, our analyses nominate RBPs that may coordinate the TEC of evolutionarily conserved networks.

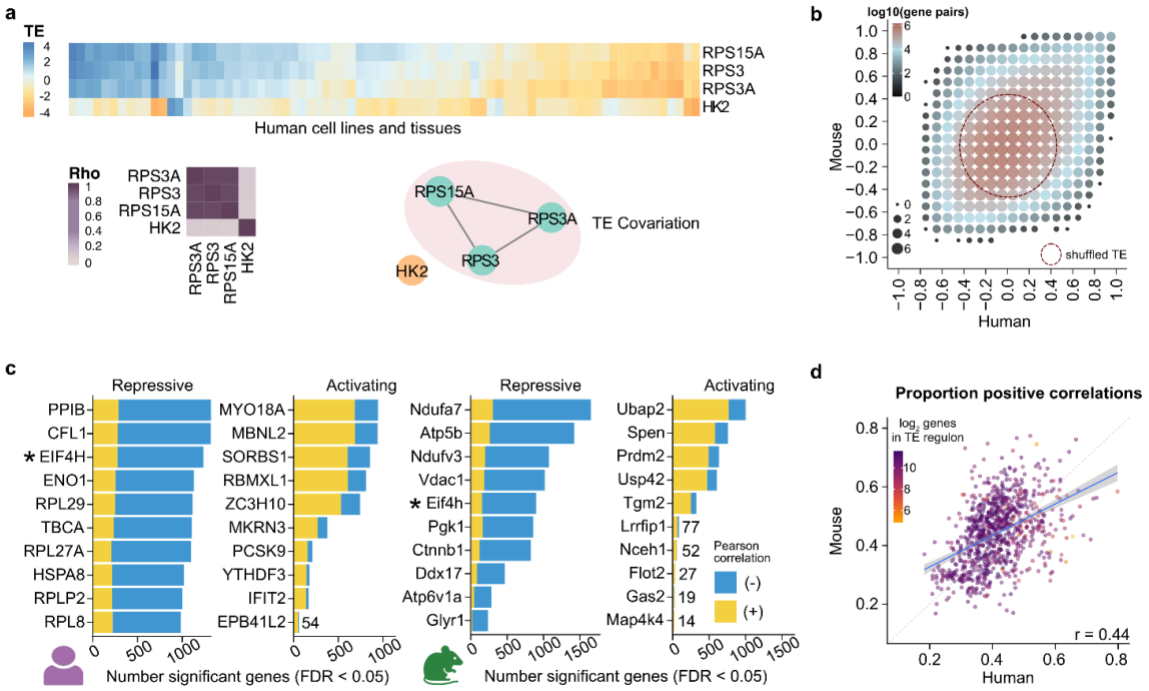

Fig. 3 | Translation efficiency covariation is conserved between human and mouse. a, Example illustrating TEC between genes. The top section presents TE patterns across cell types in human. The bottom left part displays the similarity of the pattern between these genes quantified using proportionality scores. **b,** We calculated the TEC for gene pairs and compared their differences for the same orthologous gene pairs between human and mouse. In the figure panel, each dot size represents the aggregated $\log_{10}$-transformed counts of gene pairs falling within specified ranges. We also calculated TEC using randomized TE for each gene (shuffled). The red dashed line in the figure captures the 95% gene pair TEC values obtained with shuffled TE (ExtendedDataFig. 14). **c,** The top ten RBPs with the highest number of genes showing significant correlations between transcript TE and RBP RNA expression are displayed. An asterisk marks genes in the top ten in both species. **d,** For all RBPs (each dot), we plotted the proportion of positive correlations between TE for genes in its TE regulon and the RNA expression of the RBP. Blue line is a linear fit with 95% confidence intervals in gray. Pearson correlation coefficient is shown.

TEC between transcripts across cell lines and tissues is associated with shared biological functions

Given that co-expression at the RNA level is predictive of shared biological functions[11,72,73], we next assessed whether TEC indicates common biological roles among genes. We calculated the area under the receiver operating characteristic curve (AUROC) to measure the ability of TEC in distinguishing genes with the same biological functions (Methods). Genes that are annotated with a common GO term exhibited a similar degree of RNA co-expression and TEC, both of which

were significantly higher than would be expected by chance (Median AUROC across GO terms calculated with TEC: 0.63 for human, 0.65 for mouse; RNA co-expression RNA: 0.66 for human, 0.69 for mouse; Fig. 4a; table S13-14; Methods). These findings demonstrate that TEC, similar to RNA co-expression, serves as an indicator of shared biological functions among genes.

Furthermore, we observed that biological functions whose members exhibit a high degree of RNA co-expression were also likely to have TEC. Specifically, the Spearman correlation between the AUROC scores calculated using TEC and RNA co-expression was ~0.64 for human GO terms in contrast to ~-0.02 when random genes were grouped (Fig. 4b). Despite the low correlation between average RNA expression and TE for human genes (Fig. 2g), our results highlight that members of specific biological functions whose RNA expression is coordinated across cell types tend to exhibit consistent translation efficiency patterns. This finding suggests coordinated regulation at both transcriptional and translational levels among functionally related genes.

While many gene functions were predicted accurately with both RNA co-expression and TEC, we noted specific exceptions. Notably, genes in 29 human GO terms demonstrated significantly stronger TEC than RNA co-expression (at least 0.1 higher AUROC; Fig. 4c; ExtendedDataFig. 17-18; supplementary text). An example of such a GO term is 'MAPKKK activity' (Fig. 4d-e). While there is limited evidence of direct translational regulation of the MAPKKK family, the RBP IMP3 may provide a potential mechanism for such regulation[74]. Additionally, there is post-translational regulation through the binding of activated RAS to genes from the MAPKKK family, leading to their activation[75]. These results indicate that some genes with specific biological functions exhibit greater similarity at the translational level.

We hypothesized that genes with shared functions and high TEC may be regulated through a common mechanism, analogous to shared transcription factor binding sites that mediate RNA co-expression[76,77]. Accordingly, we expected these genes to harbor sequence elements bound by RBPs. We identified enriched heptamers in the transcripts of five human and three mouse GO terms with significant TEC and at least 12 genes in the GO term (AUROC measured with TEC > 0.7, difference in AUROC between TEC and RNA co-expression > 0.2; Fig. 4f; ExtendedDataFig. 17b; ExtendedDataFig. 18e; Methods). For example, we found AG-rich motifs in coding regions of human genes with "molecular function inhibitor activity" (Fig. 4f). These motifs match the known binding sites of three RBPs (TRA2A, PABPN1, and SRSF1). In line with the enrichment of these motifs, analysis of eCLIP data revealed increased deposition of these RBPs in the coding sequences of genes in this GO term compared to matched control transcripts (Fig. 4f; Methods). Furthermore, we identified several additional enriched heptamers that currently have no RBP annotations, suggesting these motifs might be targets for RBPs that have not yet been characterized (also see supplementary text for sequence features associated with TEC). In contrast, our analyses indicate miRNA is not a primary driver of TEC (ExtendedDataFig. 19), in agreement with previous literature[78,79].

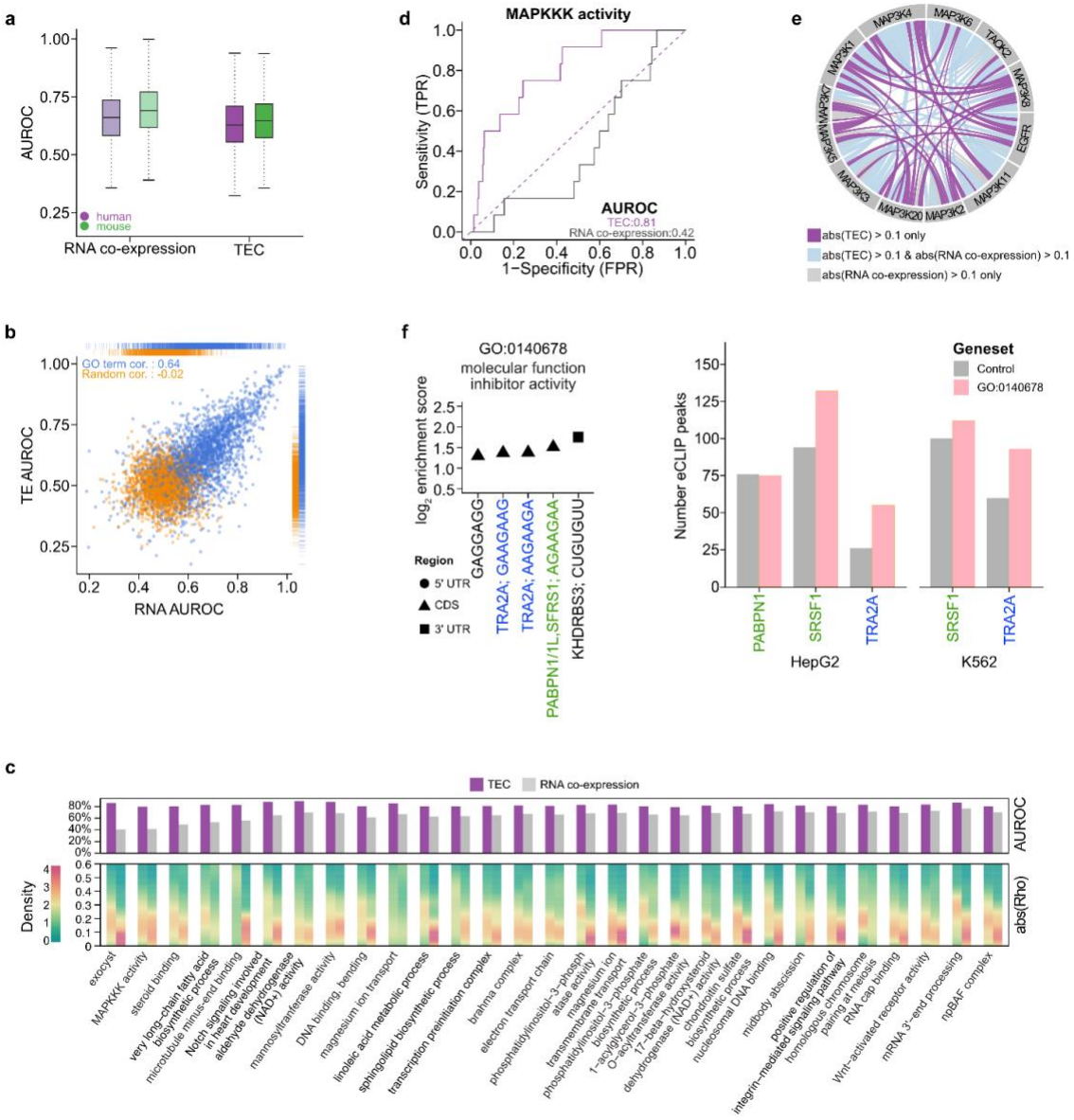

Fig. 4 | Genes associated with certain biological functions exhibit higher similarity patterns in TE than in RNA expression. a, We calculated the similarity of expression (quantified by AUROC; y-axis) among genes within 2,989 human and 3,340 mouse GO terms. In the box plot, the horizontal line corresponds to the median. The box represents the IQR and the whiskers extend to the largest value within 1.5 times the IQR. **b,** Each blue dot represents the AUROC calculated for a given GO term using TEC and RNA co-expression levels. Orange dots represent the same values for random grouping of genes (Methods). **c,** For GO terms where genes exhibit greater similarity at the TE level than at the RNA expression level (AUROC for TEC > 0.8, and difference of AUROC measured with TEC and RNA co-expression > 0.1), we visualized the distribution of

absolute rho scores for gene pairs (bottom; gene pairs with abs(rho) > 0.1). **d,** AUROC plot calculated with genes associated with MAPKKK activity. **e,** In the circle plot, the connections display absolute rho above 0.1 either at TE level alone (purple), at both RNA and TE levels (blue), or RNA level alone (gray) for gene pairs involved in MAPKKK activity. **f,** Motif enrichment (left) for the GO term 'molecular function inhibitor activity' (ExtendedDataFig. 17b). RNA binding proteins (RBPs) matching the motifs from oRNAment[80] or Transite[81] are indicated. Enhanced cross-linking immunoprecipitation (eCLIP) data[82] indicates increased binding of TRA2A and SRSF1 in the CDS of genes for this GO term compared to matched control genes with similar sequence properties (Methods).

TEC nominates gene functions

We next investigated whether gene functions may be predicted by utilizing TEC, given the success of RNA co-expression for this task[72,73]. The functional annotations of human genes are continuously being updated, providing an opportunity to test this hypothesis using recently added information to the knowledge base. Specifically, we used functional annotations from the GO database from January 1, 2021, to determine functional groups that demonstrate strong TEC among its members (AUROC > 0.8) and developed a framework to predict new functional associations with these groups (Methods). By comparing our predictions to annotations from December 4, 2022, we confirmed the predicted association of the *LOX* gene with the GO term 'collagen-containing extracellular matrix'. LOX critically facilitates the formation, development, maturation, and remodeling of the extracellular matrix by catalyzing the cross-linking of collagen fibers, thereby enhancing the structural integrity and stability of tissues[83,84]. Our prediction successfully identified this new addition, as *LOX* exhibits positive similarity in TE with the vast majority of genes in this term (Fig. 5a).

Recognizing the capacity of TEC to elucidate biological functions, we utilized a recent version of GO annotations (December 4, 2022) to systematically predict new associations for genes. To underscore the unique insights gained from TEC, we focused on the 33 human and 31 mouse GO terms that either exhibited significantly higher TEC than RNA co-expression (Table 1) or provided new functional predictions that were only supported by TEC (the ranking of the newly predicted gene with RNA co-expression fell beyond the top 50%, table S15-16; Methods). By focusing on these GO terms, we aimed to identify similarity patterns based on TE, revealing functional associations that would not be detected by RNA co-expression. We conducted a literature search to determine if prior research supported these predictions, finding that 11 have already been corroborated by previous publications, although they have not yet been reflected in the relevant GO term annotations (Table 1; supplementary text). For example, cryo-electron microscopy experiments demonstrated that human DNMT1 binds to hemimethylated DNA in conjunction with ubiquitinated histone H3[85]. This binding facilitates the enzymatic activity of DNMT1 in maintaining genomic DNA methylation. Our analysis revealed that DNMT1 was the highest ranking prediction exhibiting strong TEC with genes associated with nucleosomal DNA binding function. In mouse, we predicted Plekha7 to be a member of the regulation of developmental processes. This prediction was recently validated by the observation of neural progenitor cell delamination upon the disruption of Plekha7[86–90].

The high rate of validation of our predictions in the literature suggested that other predictions based on TEC may reflect new and yet to be confirmed functions. In particular, we observed that the human leucine-rich repeat-containing 28 (*LRRC28*) gene displays strong TEC with glycolytic genes, but is not co-expressed at the RNA level (Fig. 5b-c, table S17). Specifically, *LRRC28* displayed negatively correlated TE with key glycolytic genes including *HK1*, *HK2*, *PFKL*, *PFKM*, *PFKP*, *TPI1*, *PGK1*, *ENO1*, *ENO2*, *PKM*, and two transcription factors *FOXK1* and *FOXK2* that regulate glycolytic genes[91]. Given that the leucine-rich repeat domains typically facilitate protein-protein interactions[92], LRRC28 may interact directly with one or more of the glycolytic proteins. Using AlphaFold2-Multimer[93], we calculated the binding confidence scores between LRRC28 and all glycolysis-associated proteins (Methods) and found that LRRC28 has a very high likelihood of binding to FOXK1 (Fig. 5d-e).

FOXK1 is a member of the forkhead family of transcription factors that share a structurally similar DNA-binding domain[94,95]. Interestingly, LRRC28 likely binds both the non-DNA-binding region and DNA-binding domain of FOXK1 (distance < 4 angstroms; Fig. 5e; ExtendedDataFig. 20a). This observation led us to examine the specificity of the interaction between LRRC28 and FOXK1. We calculated the binding probabilities of LRRC28 with 35 other forkhead family transcription factors, finding that FOXK1 exhibits the strongest evidence of physical interaction with LRRC28 (Fig. 5f). This specificity is potentially due to a unique binding site between LRRC28 and FOXK1's non-DNA-binding region (Fig. 5e). As an additional control, we selected LRRC42, a protein with leucine-rich repeats that does not exhibit TEC with glycolytic genes. As expected, LRRC42 showed a very low likelihood of interaction with any of the glycolytic genes, including FOXK1 (Fig. 5d). These findings suggest that LRRC28 may serve as a regulator of glycolysis by binding to FOXK1, thereby preventing FOXK1 from binding to the promoter regions of glycolytic genes and leading to the downregulation of glycolysis. To experimentally test this prediction, we stably overexpressed LRRC28 in four human cell lines and assessed the glycolytic capacity of the cells by quantifying the extracellular acidification rate (ECAR). Stable overexpression of LRRC28 in Huh 7.5 resulted in slower growth therefore we resorted to transient overexpression strategy for this particular cell line. Congruent to our expectation, ECAR was found to be significantly lower in SH-SY5Y and Huh 7.5 cells overexpressing LRRC28 compared to cells overexpressing a control gene; LRRC42 (Fig. 5g-h). However, HEK293T and MCF-7 showed non-significant changes between the two conditions (ExtendedDataFig. 20b-c). Interestingly, the varied response in presence of LRRC28 likely reflects the metabolic state differences between cell lines and suggests differential dependency on LRRC28. Taken together, TEC reveals shared biological functions and predicts novel associations, providing insights not attainable with RNA co-expression analysis alone.

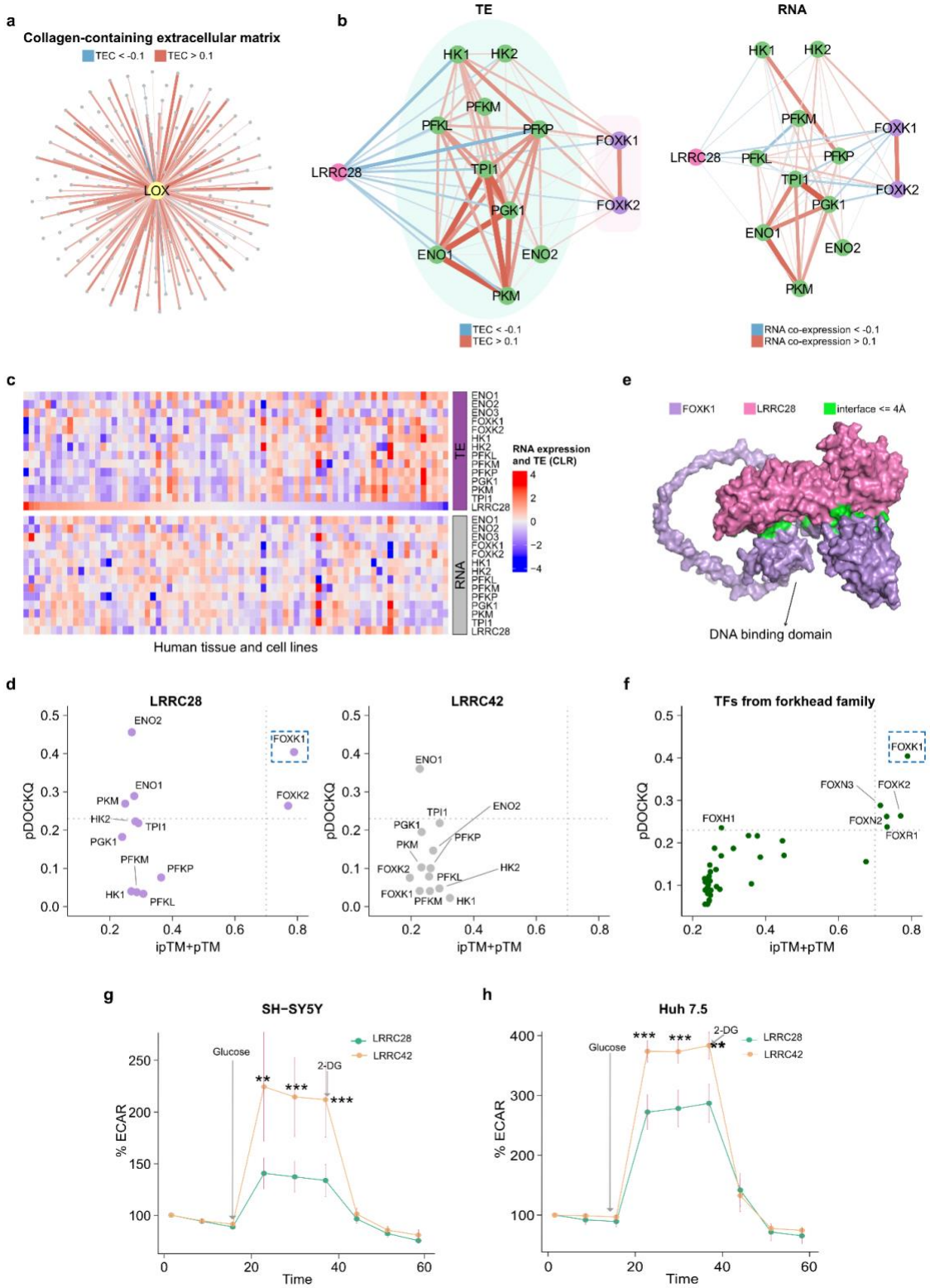
a
Collagen-containing extracellular matrix
TEC < -0.1
TEC > 0.1
LOX
b
TE
HK1
HK2
PFKM
PFKL
PFKP
FOXK1
LRRC28
TPI1
FOXK2
PGK1
ENO1
ENO2
PKM
TEC < -0.1
TEC > 0.1
RNA
RNA co-expression < -0.1
RNA co-expression > 0.1
c
ENO1
ENO2
ENO3
FOXK1
FOXK2
HK1
HK2
PFKL
PFKM
PFKP
PGK1
PKM
TPI1
LRRC28
TE
RNA
RNA expression and TE (CLR)
Human tissue and cell lines
e
FOXK1
LRRC28
interface <= 4Å
DNA binding domain
d
LRRC28
LRRC42
pDOCKQ
ipTM+pTM
f
TFs from forkhead family
FOXN3
FOXK2
FOXH1
FOXN2
FOXR1
g
SH-SY5Y
Glucose
2-DG
LRRC28
LRRC42
% ECAR
Time
h
Huh 7.5

Fig. 5 | TEC enables the prediction of novel gene functions. a, We predicted that LOX belongs to the collagen-containing extracellular matrix using an older version of human GO terms (January 1, 2021) and confirmed this prediction with the newer version (December 4, 2022; Methods). The network displays the similarity in TE between LOX (yellow dot) and other genes (gray dots) from the collagen-containing extracellular matrix. Line weight in figure panels indicates the absolute value of rho from 0.1 to 1. **b,** The networks display the rho between LRRC28 and glycolytic genes at the TE level (on the left) and RNA level (on the right) in humans. Green dots represent genes that belong to the glycolysis pathway, purple nodes are transcription factors that regulate glycolysis. **c,** TE and RNA expression of *LRRC28*, glycolytic genes, and transcription factors regulating glycolysis (*FOXK1*, *FOXK2*) across human cell types and tissues. **d,** We used AlphaFold2-Multimer to calculate the binding probabilities between the proteins LRRC28 or LRRC42 and glycolytic proteins (Methods). We evaluated the models with ipTM+pTM (x-axis) and precision of protein-protein interface binding predictions (pDOCKQ; y-axis). We set a threshold of ipTM+pTM > 0.7[96] and pDOCKQ > 0.23[97,98] as previously suggested to identify confident binding. **e,** 3D model of binding between LRRC28 and FOXK1. For visualization purposes, we removed residues 1-101 and 370-733 in FOXK1 (pLDDT scores below 50). **f,** Binding probabilities between LRRC28 and transcription factors belonging to the forkhead family[99]. The dashed lines represent ipTM+pTM > 0.7 or pDOCKQ > 0.23. Kinetic ECAR response of **g,** SHSY-5Y cell line (n=6, stable overexpression) and **h,** Huh 7.5 cell line (n=6; transient overexpression) overexpressing LRRC28 or LRCC42 to 10 mM glucose and 100 mM 2-DG. Unpaired two-sided Student's *t*-test, ***$P < 0.005$, **$P < 0.05$. Panel g & h shows mean ± s.d.; *n* shows biological independent experiments.

Genes with positive TEC are more likely to physically interact

The predicted binding between LRRC28 and FOXK1 suggests the utility of TEC to reveal physical interactions between proteins. Proteins that physically interact tend to be co-expressed at the RNA level[17,23,100], and many protein complexes are assembled co-translationally[101], leading us to hypothesize that the TE of interacting proteins may be coordinated across cell types. Specifically, we expect that there should be positive covariation between the TE of interacting proteins to ensure their coordinated production[40,41]. To test this hypothesis, we categorized gene pairs by whether they display positive or negative similarity in RNA expression or TE across cell types. Compared to all possible pairs (124,322,500), or those with the same biological function (6,492,564), physically interacting pairs of proteins (1,030,794 from STRING database[100]) were substantially enriched for positive similarity of TE and RNA expression patterns (Fig. 6a; chi-square test $p < 2.2 \times 10^{-16}$ and 1.88-fold enrichment compared to all pairs; table S18). This result aligns with the notion that genes with the same function can be regulated in opposite directions, as indicated by negative rho values, in contrast to physically-interacting proteins[102] which are enriched for positive rho values.

We then examined whether these patterns generalize to the higher-order organization of protein complexes. We observed protein complexes (as defined by hu.MAP[103]) displayed positive TEC and RNA co-expression (Fig. 6b; Methods). Noticeably, while proteins within the same complex generally exhibited similar positive patterns in both TEC and RNA co-expression, certain interactions within protein complexes were particularly evident only at the TE level (Fig. 6c-e).

For instance, members of the exocyst complex showed a strong positive TEC but not RNA co-expression (Fig. 6c-e). The exocyst complex consists of eight subunits in equal stoichiometry, forming two stable four-subunit modules[104,105]. Several known exocyst-binding partners are not required for its assembly and stability, indicating that the molecular details are still unclear[104]. Our finding suggests that translational regulation may play a role in maintaining the proper stoichiometry of the exocyst complex. In summary, physically interacting proteins are likely to have positive TEC in addition to positive RNA co-expression profiles. The positive correlation in RNA abundance and TE among physically interacting proteins may reflect an evolutionary pressure to efficiently utilize energy resources[40,41,106].

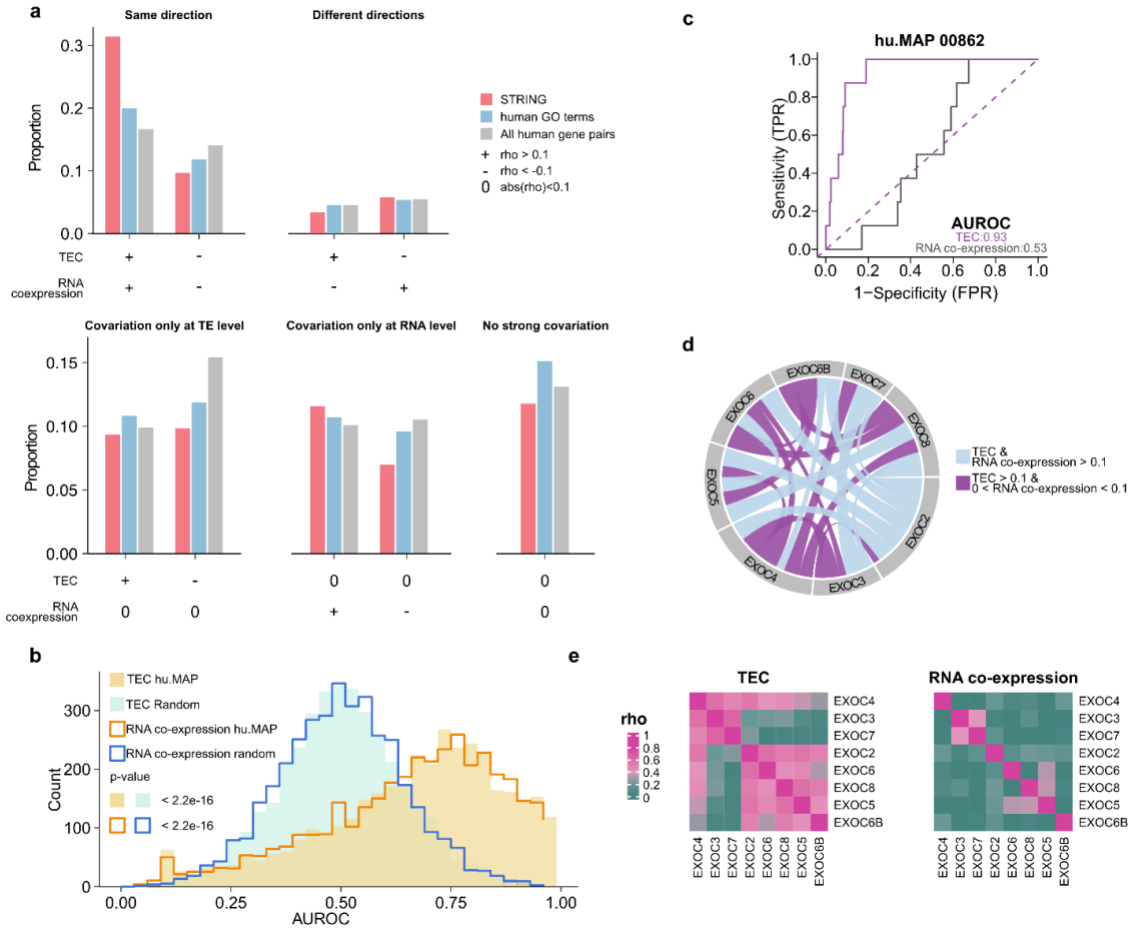

Fig. 6 | Physically interacting proteins display TEC. a, Number of pairs of genes among three sets (physical interaction-red; shared function-blue; all genes-gray) categorized based on the direction of similarity (Rho scores). **b,** The distribution AUROC calculated with either TEC or RNA co-expression for 3,755 hu.MAP terms (Methods). The distribution was compared to AUROC for each term that is randomly assigned genes with size matched to the original hu.MAP term. P-values were calculated using a two-sided Wilcoxon test. **c,** AUROC plot for hu.MAP term

00862, which includes eight genes within the exocyst complex. **d,** Connections represent gene pairs with rho scores above 0.1. Purple lines indicate pairs connected at TE level alone, while blue lines depict those at both the RNA co-expression and TE levels. **e,** Heatmaps display the rho calculated among genes at the TE (left) and RNA expression levels (right).

DISCUSSION

In this study, we analyzed thousands of matched ribosome profiling and RNA sequencing experiments across diverse human and mouse cell lines and tissues to quantify TE. A particular challenge in this effort was inadequate metadata associated with these experiments, which hampers their reuse. A particularly recurrent issue was inconsistencies in cell line identification (supplementary text). Additionally, metadata matching of RNA-seq and ribosome profiling data is necessary to quantify TE, yet this information is missing in current databases. To address these issues, we conducted a manual curation process. Given that the analyzed experiments were predominantly described in peer-reviewed publications, we anticipated the publicly accessible data would be of sufficient quality for large-scale analyses. However, more than 20% of the human and mouse experiments did not meet quality control criteria, such as ribosome footprints arising from coding regions and adequate transcript coverage, thereby deeming these studies unsuitable for further analyses. Our findings point to a pressing need for stricter data quality standards and more comprehensive, structured metadata in genomic databases.

We made several advances including the selection of RPF read lengths, data normalization, and estimation of TE (supplementary text). TE is typically defined as a log-ratio of read counts from ribosome profiling and RNA expression measurements which often leads to spurious correlations between TE and RNA levels[55]. We instead employed a compositional data analysis framework for both ribosome profiling and RNA-seq[50,56,107], allowing for a more accurate estimation of TE as evidenced by improved correlation of these values with corresponding protein abundance. In this study, we used the term “translation efficiency” consistent with its established use in prior literature. Given the compositional nature of all next generation sequencing experiments, TE also reflects the relative allocation of translational resources. Hence, a transcript can exhibit relatively higher TE even without changes in its polysome distribution, as observed in global translational capacity shifts during viral infections and other biological contexts[34,108]. In the accompanying manuscript[109], we have developed machine learning approaches to predict TE from mRNA sequences.

Recent work has suggested that ribosome occupancy normalized for mRNA abundance may not directly indicate the efficiency of protein synthesis at least in the context of base-modified reporter constructs[110]. There are several mechanisms that lead to decoupling between ribosome density and the rate of protein synthesis. For example, modulation of tRNA abundance or charging may alter ribosome elongation rates, resulting in apparent increases in TE. However, our work and others indicate that TE as defined here is significantly correlated with protein abundance and synthesis rate for endogenous transcripts[111]. Thus, for most endogenous mRNAs, TE (ribosome density) is positively associated with protein production.

In this study, we introduce the concept of TEC which quantifies the similarity of translation

efficiency patterns across cell types. Among orthologous gene pairs, RNA co-expression relationships were shown to be conserved across evolution[11]. Our analyses demonstrated that covariation patterns of TE are also globally conserved, highlighting the functional relevance of these patterns. Future research leveraging network level conservation metrics could provide further insights into TEC and RNA co-expression networks. Specifically, identifying conserved and divergent subnetwork properties between TE and RNA co-expression networks could elucidate specific regulatory interactions.

RNA co-expression among genes is known to be associated with shared functions[9–11]. Our analysis indicates that TEC is also informative regarding gene function (Table 1; supplementary text). Interestingly, while for a given transcript, average RNA expression and TE across cell types are only weakly correlated, genes with particular biological functions display highly coordinated patterns of both RNA expression and translation efficiency. This coordination may enhance cellular energy conservation and responsiveness to environmental cues.

In addition, TEC revealed unique insights into protein function that elude RNA or protein-based analyses. A notable example is the covariation of TE between *LRRC28* and glycolytic genes, whose RNAs are not co-expressed. We experimentally validated the role of LRRC28 in attenuating glycolysis in two cell lines. Further, we discovered a high confidence predicted interaction between LRRC28 and FOXK1, the key transcription factor controlling glycolytic enzyme expression, providing a future direction in characterizing the mechanism. Interestingly LRRC28 is down-regulated in several cancers compared to normal tissues[112–114]. Determining how LRRC28 translation influences glycolysis rates in cancer [91,115,116] will be an important focus for future research. Importantly, these patterns were also not detectable at the protein-level as LRRC28 is absent from most proteomic databases such as PAXdb and ProteomeHD[23,62]. Taken together, these findings emphasize the unique insights provided by TEC that escape RNA and protein co-expression analyses.

TEC between LRRC28 and its potential physically interacting partner prompted us to systematically analyze the similarity of translation efficiency patterns across protein complexes. We found a significant enrichment of positive TEC between physically interacting protein pairs, establishing that physically interacting proteins often exhibit coordinated translation efficiencies across different cell types. This coordination may facilitate the co-translational assembly[101] of certain protein complexes and contribute to their stoichiometric production. Such RNA and translation level coordination between physically interacting proteins likely enhances the efficiency of complex formation and optimizes the energetic costs associated with these processes. This optimization is particularly advantageous given that protein biosynthesis is the largest consumer of energy during cellular proliferation[41,45,106].

We acknowledge several limitations in our study. First, the limited number of samples for certain cell lines may reduce the accuracy of translation estimates for those cell types. Second, our analysis focused on genes robustly expressed across most cell types, limiting our ability to assess TEC for genes with highly cell-type-specific or consistently low expression levels. Third, the quality of available RNA-seq data is insufficient for reliable reconstruction of high-quality, cell-type-specific transcriptomes. As a result, we only considered a representative transcript[117] for each gene based

on criteria such as conservation, structure, and functional domains. Additionally, the short length of RPFs complicates mapping to multiple isoforms, which may affect conclusions for genes with significant alternative splicing.

In summary, our analyses reveal TEC is informative in uncovering gene functions, is conserved between humans and mice, and suggests simultaneous coordination of both RNA expression and translation among physically interacting proteins, establishing translation efficiency covariation as a fundamental organizing principle of mammalian transcriptomes.

ACKNOWLEDGMENTS

We thank all contributions to metadata curation: Hansel Chiang, Ashley Hoffman, Tori Tonn, Alia Segura, Charisma Tante, Eric Vasquez, and Liaoyi Xu. We also thank Yuna Shin and Victoria D. Chapman for their help with the experiments. We appreciate Dr. Milad Miladi for providing critical feedback. The original text in this paper was written by the authors. A LLM was used to suggest edits for clarity and grammar[118]. The authors acknowledge the Texas Advanced Computing Center (TACC) at The University of Texas at Austin for providing high-performance computing and storage resources that have contributed to the research results reported within this paper. URL: http://www.tacc.utexas.edu.

Research reported in this publication was supported in part by the National Institute Of General Medical Sciences of the National Institutes of Health under Award Number R35GM150667 (CC). This work was also supported by the National Institutes of Health grant [HD110096], and the Welch Foundation grant [F-2027-20230405] (C.C.). C.C. was a CPRIT Scholar in Cancer Research supported by CPRIT Grant [RR180042].

AUTHOR CONTRIBUTIONS

Y.L., I.H., and C.C. co-wrote the original manuscript. Y.L., I.H., and S.R. generated the figures for the manuscript. H.O., M.G., and J.C. downloaded all the data from GEO and processed raw sequencing data. Y.L. and C.C. developed the translation efficiency calculation pipeline. J.C. and C.C. designed and implemented the winsorization method. Y.Z. performed the deduplication comparison. Y.L. and C.C. developed the translation efficiency covariation analysis and function prediction pipelines. Y.L., K.Q., and H.O. performed the quality control analysis for all sequencing data. Y.L. carried out covariation analysis, gene function prediction, and AlphaFold2 analysis. I.H. conducted the RBP analysis. L.P., J.W., D.Z., and V.A. assessed the quality of TE measurements by developing machine learning approaches. H.O., J.W., D.Z., V.A., Q.Z., and E.S.C. provided suggestions for the manuscript. Y.L., Q.Z., and E.S.C. conducted literature search to evaluate gene function predictions. S.R. conducted the experimental validation of LRRC28. S.R., I.H., V.G., and D.P. performed other experiments. C.C. provided study oversight, conceptualized the study and acquired funding. All authors approved the final manuscript.

DATA AVAILABILITY

Metadata about RiboBase can be found in Supplementary table S1. Ribo files for the HeLa cell line are accessible at https://zenodo.org/records/10594392. Full TEC and RNA co-expression

matrices are accessible via Zenodo repository at: https://zenodo.org/uploads/10373032. A RiboFlow configuration file and processed ribo files can be accessed at https://zenodo.org/uploads/11388478. Sequencing data and ribo files for the RBP knockout experiments are available on GEO GSE269734. Data will be publicly released upon successful review of this article.

CODE AVAILABILITY

The code used in the study is available at https://github.com/CenikLab/TE_model/tree/main. Code will be publicly released upon successful review of this article.

DECLARATION OF INTERESTS

D.Z., J.W., and V.A. are employees of Sanofi and may hold shares and/or stock options in the company. H.O. is an employee of Sail Biomedicines. I.H. is an employee of Monoceros Biosystems.

METHODS

Acquisition and curation of ribosome profiling data

We used keyword search ("ribosome profiling", "riboseq", "ribo-seq", "translation", "ribo", "ribosome protected footprint") to determine studies that may employ ribosome profiling in their experimental design, from the Gene Expression Omnibus (GEO) database, with a cutoff date of January 1, 2022. Search results were manually inspected and studies containing ribosome profiling data were kept. Organism, cell line, publication, and short read archive (SRA) identifiers were obtained by automatically parsing the GEO pages of the corresponding study and sample. There was no dedicated experiment-type field for ribosome profiling experiments in GEO. Therefore we determined the experiment type (ribosome profiling, RNA-Seq, or other) of each sample by manually inspecting the GEO metadata and the associated publication of the study. Typically, ribosome profiling samples were indicated in GEO using one of the following terms: "ribosome protected footprints", "ribo-seq", and "ribosome profiling" in various parts of the metadata such as title, extraction protocol, and library strategy. If there were RNA-Seq samples in the same study, they were matched with ribosome profiling experiments, where available, after inspecting the sample names, metadata, and the publication of the study.

Adapters are commonly observed on the 3' end of sequencing reads in ribosome profiling experiments, a consequence of the inherently short length of RPFs. If the 3' adapter sequence was listed in GEO, we extracted it as part of the manual data curation process. If this sequence was unavailable, we attempted to determine it from the corresponding publication of the study. If no explicit sequence was available, we computationally analyzed the sequencing reads and searched for commonly used adapters which are CTGTAGGCACCATCAAT, AAGATCGGAAGAGCACACGTCT, AGATCGGAAGAGCACACGTCTGAACTCCAGTCAC, TGGAATTCTCGGGTGCCAAGG and AAAAAAAAAA. If any of these adapters were found in at least 50% of the reads, we used the detected sequence as the 3' adapter. If no match was found, we removed the first 25 nucleotides

of the reads anchored 6 mers and tried to extend them. If any of these extensions reached 10 nucleotides and were still detected in at least 50% of the reads, we took the highest matching sequence as the 3' adapter. On the other hand, for sequencing reads from SRA having a length of less than 35 nucleotides, we assumed the 3' adapters had already been removed. Detailed code can be accessed from: https://github.com/RiboBase/snakescale/blob/main/scripts/guess_adapters.py.

RiboBase was pre-populated after mining GEO. Then data curators were assigned specific studies and used the web-based interface to access the database. Each study was curated independently by at least two people. In case of disagreements, an additional experienced scientist inspected the corresponding studies and publications to make the final decision. We supplemented any missing metadata from GEO by checking the corresponding publications to ensure completeness. The result of this data curation process with information such as cell line, organism, and matched RNA-seq can be found in table S1, which forms the metadata backbone of RiboBase.

Ribosome profiling and RNA-seq data processing

For each selected study in GEO, ribosome profiling and matching RNA-Seq reads (where available) were downloaded, from SRA, using the SRA-Tools version 2.9.1[119], in FASTQ format using their accession numbers. FASTQ files were processed using RiboFlow[51] where parameters were determined using the metadata in RiboBase. The reference files for human and mouse transcriptomes, annotations, and non-coding RNA sequences are available at https://github.com/RiboBase/reference_homo-sapiens and https://github.com/RiboBase/reference_mus-musculus, respectively. The detailed documentation and code used to select representative transcripts are also provided: https://github.com/ribosomeprofiling/references_for_riboflow/tree/master/transcriptome/human/v2 and https://github.com/ribosomeprofiling/references_for_riboflow/tree/master/transcriptome/mouse/v1. Briefly, the 3' adapters of the ribosome profiling reads were trimmed using Cutadapt version 1.18[120] and reads having lengths between 15 and 40 nucleotides were kept. Then, reads were aligned against noncoding RNAs, and unaligned reads were kept. Next, reads were aligned against transcriptome reference, and alignments having mapping quality score above 20 were kept. Reads having the same length and mapping to the same transcriptome position were collapsed, which we refer to as "PCR deduplication". In the final step, we compiled the alignments into ribo files using RiboPy[51]. All alignment steps used bowtie2 version 2.3.4.3[121]. For each sample, we also performed the same run without the PCR deduplication step. We developed a pipeline, Snakescale, available at https://github.com/RiboBase/snakescale, to automate the entire process from downloading the data from SRA to generating the ribo files. Snakescale went over the selected list of studies and obtained their metadata from Ribobase, downloaded the sequencing data from SRA, generated Riboflow parameters file, and ran Riboflow to generate the ribo files. Examples of non-deduplicated ribo files for the HeLa cell line can be accessed at https://zenodo.org/records/10594392[122].

To visualize the length distribution of the RPFs, we applied the scale function (z-score) in R to normalize the count of RPFs mapped to CDS regions with PCR-deduplicated ribosome profiling data. Subsequently, we plotted the distribution of these normalized RPFs using the heatmap (Fig.

1c; ExtendedDataFig. 2).

Determination of cutoff for RPF lengths and quantification of ribosome occupancy

Ribosome profiling experiments employ a range of ribonucleases including RNase I, RNase A, RNase T1, and MNase (i.e., micrococcal nuclease) (S7). These different enzymes lead to variable RPF lengths[53,123–125]. To ensure that we retain high-quality RPFs for further analyses, we implemented a dynamic extraction module that automatically selected lower and higher boundaries of RPFs for each sample. Initially, we determined the first RPF length, ranging from 21 to 40 nucleotides, that contained the highest number of CDS mapping reads. Then, we examined the two positions adjacent to this selected position. The extension of the position was carried out on either side to include a higher number of CDS-aligned reads. This extension process was repeated until it encompassed at least 85% of the total CDS reads within the 21 to 40 nucleotides range (ExtendedDataFig. 3a). The final two positions identified were designated as the lower and upper boundaries. If these boundaries extended to either 21 or 40 nucleotides without including a sufficient number of reads, then 21 or 40 nucleotides, respectively, were set as the final boundaries. This approach was employed to establish the RPF cutoffs for each sample.

Transcript coverage and quality control for ribosome profiling data

We performed quality control using RPFs that were deduplicated based on the length and position (PCR-deduplication) ribo files (Fig. 1d-e). We set two cutoffs for ribosome profiling quality control. We required that on average each nucleotide of the transcript should be covered at least 0.1 times (0.1X). Coverage was calculated with the formula:

$$coverage = \frac{total\ nucleotides\ from\ reads\ mapped\ to\ transcripts}{total\ length\ of\ transcripts}$$

Additionally, samples with CDS mapping read percentage of 70% or higher were retained for subsequent analysis.

To assess the pattern of three nucleotide periodicity that is typically associated with ribosome profiling experiments, we first selected the length of RPFs with the highest number of counts from the PCR deduplicated ribo files. We then assigned all CDS mapping reads to one of three coding frames based on the position of their 5’ end. We aggregated the results for all genes for each sample. To facilitate comparison, we reordered the counts for each position of the three nucleotide periodicity from highest to lowest and converted these counts into percentages for each sample.

We initially classified samples based on the differences between positions 1 and 2. We identified Group 1 by selecting samples where the difference exceeded the 10th percentile of these differences between positions 1 and 2. For the remaining samples, we further classified them based on the differences between positions 2 and 3. Similarly, samples that did not exceed the 10th percentile of these differences between positions 2 and 3 among remaining samples were classified as Group 3, while the rest samples were Group 2. We further summarized the samples based on their QC status.

We classified samples from Group 1 as exhibiting three-nucleotide periodicity. The percentage of samples following three-nucleotide periodicity was calculated by dividing the number of Group 1 samples by the total number of samples across all three groups.

PCR and Unique Molecular Identifiers (UMIs) deduplication comparison

We selected eight ribosome profiling experiments that incorporated UMIs into the sequence library preparation to assess the impact of different deduplication methods. Specifically, these samples are GSM4282032, GSM4282033, and GSM4282034 from GSE144140[126]; GSM3168387, GSM3168389, GSM3168390 from GSE115162[124]; and GSM4798525, GSM4798526 from GSE158374[34]. We processed the data using Riboflow, applying three different deduplication methods: non-deduplication, PCR deduplication, and UMI deduplication. The yaml files are available at https://github.com/CenikLab/TE_model/tree/main/riboflow_scr. The RPF length cutoffs for samples from GSE144140 and GSE115162 are listed in table S6. Since GSE158374 is not currently included in RiboBase, we manually performed the dynamic module and selected 28 to 32 as the RPF cutoff for this study.

Winsorization of CDS mapping read counts

To address the issue of reduced usable reads resulting from PCR deduplication (supplementary text), we employed a winsorization method, which was previously proposed for tackling this problem[40,127]. For each gene's CDS region, we obtained the distribution of non-deduplicated nucleotide counts and calculated the 99.5th percentile value. This calculation was based on reads whose lengths fell within the RPF range determined by the RPF boundary selection function. RPF counts that exceed the 99.5th percentile were capped to the value corresponding to the 99.5th percentile. This method was designed to mitigate the impact of outlier values that might arise due to disproportionate amplification during the PCR process[40].

Gene filtering and normalization for ribosome profiling and RNA-seq

RNA-seq experiments in RiboBase utilized several different strategies to enrich mRNAs. The two most common approaches were the depletion of ribosomal RNAs and the enrichment of transcripts by polyA-tail selection. This difference leads to dramatically different quantification of a subset of genes that lack polyA-tails (e.g. histone genes, ExtendedDataFig. 6c). Hence, we removed 166 human and 51 mouse genes identified as lacking polyA tails (table S8-9)[128,129].

We normalized both PCR-deduplicated RNA-seq data and winsorized non-deduplicated ribosome profiling data with counts per million (CPM) after removing the genes without polyA-tails. Genes with CPM less than one in over 30% of the total samples in both RNA-seq and ribosome profiling for either human or mouse were removed in further analyses. 11,149 human and 11,434 mouse genes were retained using this approach. We have summed the counts of all polyA genes that were filtered out and grouped them under 'others' in the count table.

Validation of manual curation and quality control by matching between RNA-seq and ribosome profiling from RiboBase

We assessed the manual matching of ribosome profiling (winsorization) and RNA-seq (PCR deduplication) data in RiboBase by establishing a matching score for the samples that successfully passed quality control (transcript coverage > 0.1X and CDS percentage > 70% with PCR-deduplicated ribosome profiling data). We calculated the coefficient of determination (R^2) using the Centered Log Ratio (CLR) transformed gene counts. This was done for each ribosome profiling sample against all corresponding RNA-seq samples within the same study. Subsequently, for each ribosome profiling sample, we calculated the difference between the R^2 of its matching pair from RiboBase and the mean R^2 of the non-matching pairs within the same study. The difference was defined as the matching score.

To remove poorly matched samples in both human and mouse datasets, we established a cutoff based on the R^2 from the matched ribosome profiling and RNA-seq data in RiboBase. Any sample with an R^2 lower than 0.188 in either human or mouse, which is Q1 - 1.5 * IQR of mouse R^2 distribution, was considered a poor match and consequently excluded from further analysis (ExtendedDataFig. 6b). Finally 1,054 human and 835 mouse ribosome profiling experiments with their matched RNA-seq were used for TE calculation.

Translation Efficiency (TE) calculation

CLR normalized counts from PCR-deduplicated RNA-seq and winsorized non-deduplicated ribosome profiling were used to calculate TE with compositional linear regression[49,107,130]. Missing values can limit the power of TE calculations, and there is ongoing debate on how to address zeros in compositional data [131]. Previous studies have shown that approximately 15–40% of genes in bulk RNA-seq datasets from various tissues are not expressed [132]. To address the issue of missing values, we followed the guidance from the propr library, replacing zeros with the lowest observed read count (one). This approach ensures that these zeros are represented as a low proportion within the sample. We also applied two other zero imputation methods: Geometric Bayesian-Multiplicative and Square-root Bayesian-Multiplicative from zCompositions package (version:1.5.0.4) for TE and TEC calculations.

In our linear regression approach, ribosome profiling data served as the dependent variable, while the corresponding RNA-seq data provided the explanatory variable. The first step involved transforming the gene count, which includes 'others', into CLR normalized compositional vectors. Given the constraints of count data within a simplex, a further transformation from CLR to Isometric Log Ratio (ILR) was necessary for linear regression[49]. This transformation is crucial as it allows the compositional data to be decomposed into an array of uncorrelated variables while preserving relative proportions. The ILR transformation projects the original data onto a set of orthonormal basis vectors derived from the Aitchison simplex. Then the linear regression model applied to these transformed variables can be represented as:

$$Y = b + B \times X$$

Where Y is the ILR-transformed ribosome profiling data and X is the ILR-transformed RNA-seq data. The model assumes a normal distribution:

$$Y \sim N^{(D-1)}(Y, \Sigma\varepsilon)$$

Where Σε represents the residual variances. These residuals were then extracted from each sample and reconverted to CLR coordinates which are used as the definition of TE for each gene in each sample. Finally, we averaged TE for different cell lines and tissues (Fig. 2b, ExtendedDataFig. 7), and reported the TE in table S10-11. The scripts to generate TE are available at https://github.com/CenikLab/TE_model. We also provide uncertainty estimates calculated using the metric standard deviation designed for compositional data from the Compositions (version: 2.0.8) library (table S21-22).

Correlation between translation efficiency and protein abundance

We assessed the correlation between TE and protein abundance from seven human cell lines (A549, HEK293, HeLa, HepG2, K562, MCF7, and U2OS). The protein measurements were obtained from PAXdb[62]. 9924 genes were shared between our TE and the protein abundance data. We calculated the Spearman correlation coefficient for each cell line using the 'stats' package in R to evaluate the relationship between TE and protein abundance. For a more detailed discussion of how to interpret similarity between protein abundance and sequencing based measurements of RNA-expression and translation see Csardi et al.[133].

Conservation of translation efficiency between orthologous genes from human and mouse

Orthologous genes between human and mouse were identified using the 'orthogene' package from Bioconductor[134] using the parameters 'standardise_genes=TRUE, method_all_genes="homologene", non121_strategy="keep_both_species"'. A single human gene could correspond to multiple mouse orthologs or vice versa. To maintain all one-to-many matches in our analysis, each correspondence is represented by multiple rows in our table (if a human gene 'A' is orthologous to mouse genes 'B' and 'C', we generate two separate rows: 'A-B' and 'A-C'). Human genes lacking corresponding mouse orthologs were excluded or vice versa. As a result, a total of 9,194 gene pairs were identified as orthologous between human and mouse (table S12)

To capture the variability in TE and mRNA expression between orthologous genes in human and mouse, we measured the standard deviation using the metric standard deviation (msd) function from the 'compositions' package in R[135]. We observed a negative Spearman correlation coefficient between msd of TE and mean TE, as well as msd of RNA expression and mean RNA expression, in both species. To address the dependency between msd and mean values, we conducted a partial correlation analysis. For example, we adjusted the human msd values using the mean TE from both human and mouse with the 'pcor.test' function from the 'ppcor' package[136].

GO term analysis was performed using FuncAssociate 3.0, accessible at http://llama.mshri.on.ca/funcassociate/[137]. For this analysis, we set either 9,194 mouse or 9,189 human orthologous genes as the background. We generated association files for these genes with the December 4, 2022 version of human or mouse GO terms. In the human or mouse association file, we only kept those GO terms containing at least 10 genes for further analysis.

Assessment of methods for calculating genes' similarity with ribosome occupancy data

We used eight commonly used methods to quantify the similarity of ribosome occupancy across

cell types for all pairs of 11,149 human or 11,434 mouse genes in RiboBase.

Method 1 - CPM-normalized ribosome footprint counts were used to calculate the Pearson correlation coefficient as implemented in the stats R package.

Method 2 - Quantile-normalized (customized Python script) ribosome footprint counts were used to calculate the Pearson correlation coefficient.

Method 3 - Ranking of ribosome footprint counts was used to calculate the Spearman correlation coefficient as implemented in the stats R package.

Method 4 - CLR-normalized ribosome footprint counts were used to calculate the proportionality (rho scores) between genes as implemented in the propr package with lr2rho function[50].

Method 5 - CPM-normalized ribosome footprint counts were used to calculate the similarity between genes with a decision tree-based method as implemented in the treeClust package[23,138]. We applied the 'treeClust.dist' function with a dissimilarity specifier set to d.num=2.

Method 6 - Quantile-normalized ribosome footprint counts were used to calculate the similarity between genes with the decision tree-based method.

Method 7 - CPM-normalized ribosome footprint counts were used to calculate gene similarity with the generalized least squares (GLS) method[139].

Method 8 - Quantile-normalized ribosome footprint counts were used to calculate gene similarity with the GLS method.

We compared these eight ribosome occupancy similarity matrices to determine the most effective method for constructing gene relationships with respect to biological functions. This assessment employed the guilt by association principle to ascertain the functional coherence within a gene matrix, determining if genes associated with a particular biological function (GO terms[140], TOP mRNAs[69]) exhibit similar expression patterns and network interactions[141].

The complete ontology was sourced from the Gene Ontology website, with the files goa_human.gpad.gz and mgi.gpad.gz, generated on December 4, 2022[140]. The annotation of Gene Ontology terms was accomplished with the aid of the org.Hs.eg.db and org.Mm.eg.db R packages[142,143]. We restricted the selection of GO terms to those associated with the 11,149 human and 11,434 mouse genes that had passed gene filtering. We used GO terms associated with at least 10 but less than 1,000 genes for evaluation, yielding a total of 2,989 human and 3,340 mouse GO terms.

We then employed the neighbor-voting algorithm to assess the covariations of ribosome occupancy among genes from the same GO term with AUROC[141]. Specifically, we first converted the similarity scores to absolute values. Then we extracted genes associated with a specific function and implemented the leave-one-out cross-validation method. For this analysis, we iteratively masked one gene at a time, treating it as if it did not belong to the function. In each iteration, we calculated the total sum of similarity scores from all genes not belonging to the

function to all the remaining genes within the function. We normalized the sum of similarity scores for each gene against the sum of similarity scores for that gene with all genes. After normalization, we converted these normalized similarity scores into rankings. We retained the rankings only for genes that belong to this specified functional property. Finally, we computed the AUROC for all genes within this functional property based on these rankings. A detailed script for genes' functional similarity pattern analysis can be found: https://github.com/CenikLab/TE_model/blob/main/other_scr/benchmarking.R.

RNA co-expression and translation efficiency covariation

We introduce the concept of TEC, which employs a compositional data analysis approach[49,50] to quantify the similarity patterns of TE across various cell and tissue sources, as described in Method 4 above. The proportionality scores were calculated with the following formula from the propr package with lr2rho function[50]:

$$Rho(A_i, A_j) = \frac{1 - var(A_i - A_j)}{(var(A_i) + var(A_j))}$$

Where Ai and Aj represent TE values for genes i and j from the TE matrix A.

In this study, the TEC was calculated with 77 human cell lines for 11,149 genes or 68 mouse cell lines for 11,434 genes. The proportionality coefficients (rho scores) generated from this method range from -1 to 1. Full TEC and RNA co-expression matrices are accessible via Zenodo repository at: https://zenodo.org/uploads/10373032.

Evaluation of the ability of TEC to predict novel gene functions

We compared the AUROC between an older version of GO terms (January 1, 2021) to the newer version of GO terms (December 4, 2022) to identify genes that had been newly added to the GO terms in this timeframe. GO terms were downloaded and filtered to include only those terms containing between 10 and 1,000 genes with either human or mouse backgrounds (11,149 human genes or 11,434 mouse genes). We selected 184 human and 238 mouse GO terms from the older version that demonstrated high TEC similarity (AUROC > 0.8) among genes within the same term for predicting novel gene functions. We first converted the rho scores for TEC between gene pairs to absolute values. For genes not currently included in the GO terms, we calculated the sum of rho for each gene relative to all genes within the term, based on either TE or mRNA expression levels. We then normalized these rho sums for each gene against the total rho sum of that gene across all 11,149 human genes or 11,434 mouse genes. These normalized values were converted into ranking percentages to reflect the likelihood of these genes being associated with the respective GO term. Finally, we identified the top-ranking genes as potentially new additions and cross-validated them with the newer version of the GO terms to confirm our predictions.

Prediction of novel gene functions with TEC

We analyzed 243 human and 310 mouse GO terms as of December 4, 2022, which demonstrated high similarity patterns between genes in TE level (AUROC > 0.8) to predict novel gene functions.

Absolute TEC rho scores served as the input for biological function prediction (GO terms). The prediction method followed the same protocol as our previous evaluations of TEC's ability to predict novel gene functions. However, we added a filter step: a newly predicted gene was retained only if its average rho score with other genes within the same term exceeded the overall average rho score for all existing genes in that term. This prediction analysis was performed using a custom script that can be found at https://github.com/CenikLab/TE_model/blob/main/other_scr/prediction.R.

Computational evaluation of the interaction between LRRC28, glycolytic proteins, and proteins from forkhead TF family

We computed the pair-wise interaction probabilities between LRRC28 or LRRC42 and glycolytic proteins (HK1, HK2, PFKL, PFKM, PFKP, TPI1, PGK1, ENO1, ENO2, and PKM) with AlphaFold2-Multimer 2.3.0[93,144]. In addition, we also calculated pairwise interaction probabilities for LRRC28 with 35 proteins from the forkhead transcription TF family[99]. We extracted the canonical amino acid sequence for each gene from UniPort[145] as the input file. We set 0.7 as the cutoff of ipTM+pTM as a high-confidence protein structure and binding probability cutoff[96]. We then evaluated the interfaces predicted by AlphaFold2-Multimer, using a pDOCKQ score greater than 0.23 as our criterion for reliability[97,98].

Benchmarking TEC and RNA co-expression for protein interactions

Using a similar approach to our benchmarking with biological functions, we employed the neighbor-voting algorithm to assess physical protein interactions based on rho scores among genes at either the TE or mRNA expression level. We first kept the non-negative rho between genes and set negative rho to zero. We then analyzed similarity patterns between genes from the same protein complex, downloading from the hu.MAP 2.0 website[103]. In this process, we excluded genes from hu.MAP terms that were not in the 11,149 human gene list, resulting in 8,024 overlapping genes between our list and hu.MAP terms. Furthermore, we removed hu.MAP terms that included fewer than three genes. This filtering process left us with 3,880 hu.MAP terms, among which 3,755 contained unique genes.

Since proteins within the same complex may not physically interact, we used physical interaction pairs downloaded from the STRING website instead of gene pairs from hu.MAP terms to summarize the interactions in Fig. 6a.

Identification of enriched RNA motifs among genes with high degree of TEC

To reduce bias in motif enrichment analysis that may arise by ribosome footprint mapping to paralogous genes, we removed predicted paralogs from each GO term using Paralog Explorer[146] (DIOPT score > 1). Then, we enumerated heptamers in each transcript region using the Transite kmer-TSMA method[81] with default parameters for each species (human, mouse), transcript region (5' UTR, CDS, 3' UTR), and GO term (selected terms with TE AUROC > 0.7, TE-RNA AUROC difference > 0.2, and number genes after paralog removal >= 12). For mice there were three terms and for humans there were eight. We selected the three mouse terms and top five terms in humans with the highest number of genes and greatest AUROC difference.

After counting heptamers with Transite, we selected motifs that had >20 hits among genes in the GO term to address assumptions of uniformity near p-values of 1 for some multiple-test correction methods. Then, we used the Holm method to correct p-values for each species separately, and selected motifs with an adjusted p-value < 0.05. Finally, heptamers were annotated with RBPs included in the Transite[81] and oRNAment databases[80]. For annotation of RBPs in the oRNAment database, we required that the heptamer have a matrix similarity score[80] of 0.8 or greater when matching to each RBP position weight matrix. RBP motif hits from other species (*Drosophila*, artificial constructs) were removed from RBP annotations, and the hits to the heptamer of *Drosophila* tra2 were annotated as TRA2A for human genes with the term GO: 0140678.

eCLIP data for PABPN1, SRSF1, and TRA2A were downloaded from ENCODE[82] as BED files (K562 and HepG2 cell lines, GRCh38 reference). The BED files for biological replicates were concatenated and peaks that overlapped by at least one base pair were merged with 'bedtools merge -s -c 4,6,7 -o collapse'[147]. The resulting merged peaks were intersected with transcripts in the GO term of interest and an equal number of control transcripts (Gencode v34 GTF). The control transcripts were selected by matching on length and GC content for each transcript region (5' UTR, CDS, 3' UTR) using MatchIt[148] with default parameters. Because the gene *CARMIL2* in GO term GO:0010592 does not have a 5' UTR, required for matching, we assigned it a dummy 5' UTR with length and GC content equal to the median across all transcripts. The number of eCLIP peaks in the CDS for each RBP were summed for genes in the GO term and control genes.

Identification of RBP-gene pairs with high correlation between RBP RNA expression and gene TE

The Pearson correlation coefficient between gene TE and the RNA expression of RBPs from human and mouse[68] was tested using R stats::cor.test after taking the mean of these values by cell types and tissues. P-values were corrected with the Benjamini-Hochberg procedure, and correlations were deemed significant at a FDR < 0.05. To select RBP candidates for experimental validation, the human and mouse TE regulons were intersected for each RBP, and those that had more than twenty genes in the intersection and that had a mean TEC > 0.35 between genes in the intersection were chosen.

Generation of RBP knockout cell lines

For cloning the guides required for knockout cell line generation, top two ranked guides were selected from the Brunello library[149] for each RBPs (table S18). The guides were cloned in LentiCRISPRv2 (Addgene, 52961) as per protocol[150] and confirmed by Sanger sequencing. Briefly, for lentiviral production, HEK293T cells were seeded at a density of 1.2 x 10^6 cells per well in a 6-well plate in OPTI-MEM media supplemented with 5% FBS and 100 mM Sodium Pyruvate, 24 h prior to transfection. Both the cloned gRNA plasmids for each RBP (700 ng of each transfer plasmid) were co-transfected with the packaging plasmids pMD2.G and psPAX2 (Addgene; 12259 and 12260) using Lipofectamine 3000 (Invitrogen) and the virus was collected as per the manufacturer's protocol. For generation of the knockout clones, HEK293T cells were seeded at a density of 5 x 10^4 cells per well in a 6-well plate in DMEM media supplemented with 10% FBS, 24 h prior to infection. Next day, the media was replaced with 1.5 ml of 1:2 diluted

lentivirus containing polybrene (8 µg/mL). After 16 h, the lentivirus was replaced with fresh media and puromycin (2 µg/mL) was added to the cells 48 h after transduction. The selection continued for 5 days followed by a period of recovery for 24 h before harvesting the cells.

Ribosome profiling and RNA sequencing of RBP knockout cell lines

Three million cells for the PARK7, USP42, and VIM knockout cell lines, along with an AAVS1 (safe harbor control) knockout line, were plated in three 10 cm^2 dishes. 27 h later cells at ~60% confluency were treated with 100 µg/mL cycloheximide (CHX) for 10 min at 37 ˚C, then collected in ice-cold PBS with 100 µg/mL CHX. Cells were spun at 100 x g for 7 min at 4 ˚C, then flash frozen in liquid nitrogen and stored at -80 ˚C. Cell pellets were lysed with 400 µL lysis buffer (20 mM Tris-HCl pH 7.4, 150 mM NaCl, 5 mM $MgCl_2$, 1 mM DTT, 1% Triton-X, 100 µg/mL CHX, 1x protease inhibitor EDTA free) for 10 min on ice. Lysates were clarified by centrifugation at 1,300 rpm for 10 min at 4 ˚C. 40 µL lysate was saved for total RNA extraction, and the rest of the lysate was digested with 7 µL RNaseI for 1 h at 4 ˚C. Digestion was stopped by adding ribonucleoside vanadyl complex to a final concentration of 20 mM. Digested lysates were then loaded onto a 10 mL sucrose cushion (20 mM Tris-HCl pH 7.4, 150 mM NaCl, 5 mM $MgCl_2$, 1 mM DTT, 1 M sucrose) and centrifuged at 38,000 rpm for 2.5 h at 4 ˚C using a SW41-Ti rotor. The pellet and the total RNA aliquot were both solubilized with 1 mL Trizol, and RNA was purified with the Zymo Direct-zol RNA Miniprep Kit, including DNaseI digestion.

RNA-seq

Quality of total RNA was confirmed with Bioanalyzer RNA Pico. All RIN scores were >= 9.8. Libraries were prepared from 1 µg total RNA using the NEBNext Ultra II RNA Library Prep Kit for Illumina according to manufacturer's protocol and using 8 cycles for PCR.

Ribosome profiling

RPFs were size-selected on a 15% TBE urea gel by electrophoresing at 150 V for 1.5 h. RPFs between 28-32 nt were sliced, using 28 nt and 35 nt markers as a guide. Slices were frozen at -20 ˚C for 1 h, crushed with pestles, and the RPFs were eluted in gel extraction buffer (300 mM sodium acetate pH 5.5, 5 mM $MgCl_2$) by rotating overnight at room temperature. Eluates were passed through Costar Spin-X filter tubes at 12,000 x g for 1 min 30 s. Then 1 µL 1 M $MgCl_2$, 2.5 µL GlycoBlue, and 1 mL ethanol were added and the RPFs precipitated for two days at -20 ˚C. Pellets were dried and resuspended in 16 µL water.

Libraries were generated from 8 µL RPF eluate using the Diagenode D-Plex Small RNA Kit with minor modifications: in the 3' dephosphorylation step 0.5 µL T4 PNK was supplemented and incubated for 25 min. The RTPM reverse transcription primer was used and 8 cycles were performed for PCR. Libraries were quantified by Bioanalyzer High Sensitivity DNA Kit, pooled equimolar according to the quantity of the peak for libraries with full-length inserts (~204 nt), and cleaned up with 1.8X AMPure XP beads. Adapter dimers and empty libraries were removed by size selection on a 12% TBE PAGE gel, followed by extraction with the crush and soak method, and final libraries were resuspended in 20 µL water.

Ribosome profiling and RNA sequencing analysis for RBP knockouts

Analysis was conducted using RiboFlow v0.0.1 with deduplication of both Ribo-seq and RNA-seq data. A RiboFlow configuration file and processed ribo files can be accessed at https://zenodo.org/uploads/11388478.

We used edgeR to measure RBP KO effects on 1) RNA abundance and 2) gene TE. To do this, we respectively modeled 1) RNA-seq counts of a specific RBP KO line to that of the other two RBP KO lines; and 2) Ribo-seq counts, contrasted with RNA-seq counts, for a specific RBP KO line compared to the other two RBP KO lines. All counts were enumerated from mapped reads to the coding regions. We originally included a control KO line (AAVS1 locus) for comparison; however, by PCA, this KO line showed a distinct gene expression signature from that of the other KO lines, indicating it may not be suitable as a control (ExtendedDataFig. 16d-e). Further, using the AAVS1 KO line as a control, we observed highly similar hits for each RBP KO tested. We included filtering of counts using edgeR::filterByExpr with default parameters, the TMM method for calculation of size factors, and quasi-likelihood negative binomial models for fitting. Genes were considered differential at FDR < 0.05.

Cell Culture

HEK293T and MCF-7 cell lines were obtained from ATCC. Human hepatoma Huh-7.5 cells were a gift from Charles Rice, Rockefeller University and human SH-SY5Y neuroblastoma cells were obtained from Tanya Paull (University of Texas at Austin, Austin, TX, USA). All cell lines were maintained in Dulbecco's modified Eagle's media (DMEM, GIBCO) supplemented with 10% Fetal Bovine Serum (FBS, GIBCO, Life Technologies) and 1% Penicillin and Streptomycin (GIBCO, Life Technologies) at 37°C in 5% CO_2 atmosphere. Cell lines were tested for mycoplasma contamination every 6 months.

Plasmid cloning

pCMV SPORT6 vector with LRRC28 was obtained from transOMIC (TCH1003). LRRC42 ORF was amplified using cDNA from HEK293T cells. The oligos used for PCR amplification of the two genes had a FLAG sequence to be incorporated as a N-terminal tag along with BamHI and EcoRI restriction sites in forward and reverse primers, respectively.

PCR amplification of the LRRC28 and LRRC42 ORF using the above mentioned templates were carried out using Q5 polymerase (NEB) with the following protocol; 98 °C for 30 sec, 30 cycles of 98 °C for 10 sec, 55 °C for 10 sec and 72 °C for 40 sec and a final extension at 72 °C for 2 min. The PCR amplified products were gel extracted followed by double digestion of the amplicon and the pLVX-M vector (Addgene, 125839) with EcoRI -HF (NEB) and BamHI-HF (NEB) at 37 °C for 1 h. Post digestion, the fragments were purified and cloned using T4 DNA ligase at a ratio of 1:3 at 25 °C for 1 h followed by heat inactivation at 65 °C for 15 min and transformation by heat shock method. For LRRC42 cloning, ORF was amplified using cDNA from HEK293T cell line and two sequences (seq1 and seq 2) from the pCMV-SPORT6 adjacent to EcoRI and NotI site were amplified with LRRC42 overhangs using oligos in table S23. The vector; pCMV SPORT6 vector with LRRC28 was digested with EcoRI and NotI followed by cloning of LRRC42 and two

sequences by Gibson cloning. All clones were verified by Sanger sequencing (ACGT Inc.) and full plasmid sequencing (Plasmidsaurus).

Lentivirus and stable cell line generation:

For lentiviral generation, 1.2 X 10^6 HEK293T cells were seeded in a 6-well plate followed by transfection of the cloned plasmid along with psPAX2 (Addgene, 12260) and pMD2.G (Addgene, 12259) plasmids using Lipofectamine 3000 (Invitrogen) as per the manufacturer's protocol. The generated lentivirus was used for infection using 8 µg/ ml of polybrene for HEK293T, MCF-7 and Huh 7.5 and 2 µg/ ml of polybrene for SH-SY5Y. After 48 h of infection, puromycin was added at concentrations of 2µg/ ml for HEK293T, Huh 7.5 and 1µg/ ml for MCF-7, SH-SY5Y. The selection was continued for 5 days following recovery in antibiotic-free media.

Measurement of extracellular acidification rates (ECAR):

20,000 cells of HEK293T, MCF-7 and 40,000 cells of SH-SY5Y stably expressing LRRC28 or LRRC48 and 20,000 cells of Huh 7.5 were seeded onto poly-L lysine coated XF Pro Cell Culture Microplates with Dulbecco's modified Eagle's media (DMEM, GIBCO) supplemented with 10% Fetal Bovine Serum (FBS, GIBCO, Life Technologies). Huh 7.5 was transiently transfected with either pCMV SPORT6 vector with LRRC28 or LRRC42 using lipofectamine 3000 as per manufacturer's protocol. The ECAR was measured using Seahorse XF Pro (Agilent). The cartridges were hydrated a day prior to the experiment as per the manufacturer's instructions. On the day of the experiment, prior to performing the assay, the cells were washed with Seahorse XF DMEM Medium pH 7.4 (Agilient, 103575), supplemented with 2 mM of L- Glutamine (Agilient; 103579-100) followed by incubation in non-CO2 incubator for 1 h. To determine glycolytic capacity of cells expressing LRRC28 or LRRC42, glucose (Agilient, 103577-100) was injected at a final concentration of 10 mM (Injection 1) followed by injection of 100 mM 2-Deoxy-D- Glucose (Sigma, D6134-1G) (Injection 2). Three measurement cycles for each assay point i.e. baseline, injection 1 and 2 were carried out with each measurement cycle consisting of a mixing time of 3 minutes and a data acquisition period of 3 minutes. The results were analyzed using Wave Pro 10.2.1.

REFERENCES CITED

1. Tang, F. *et al.* mRNA-Seq whole-transcriptome analysis of a single cell. *Nat. Methods* **6**, 377–382 (2009).
2. Nagalakshmi, U. *et al.* The transcriptional landscape of the yeast genome defined by RNA sequencing. *Science* **320**, 1344–1349 (2008).
3. Mortazavi, A., Williams, B. A., McCue, K., Schaeffer, L. & Wold, B. Mapping and

quantifying mammalian transcriptomes by RNA-Seq. *Nat. Methods* **5**, 621–628 (2008).

4. Schena, M., Shalon, D., Davis, R. W. & Brown, P. O. Quantitative monitoring of gene expression patterns with a complementary DNA microarray. *Science* **270**, 467–470 (1995).
5. Chen, K. H., Boettiger, A. N., Moffitt, J. R., Wang, S. & Zhuang, X. RNA imaging. Spatially resolved, highly multiplexed RNA profiling in single cells. *Science* **348**, aaa6090 (2015).
6. Combs, P. A. & Eisen, M. B. Sequencing mRNA from cryo-sliced Drosophila embryos to determine genome-wide spatial patterns of gene expression. *PLoS One* **8**, e71820 (2013).
7. Achim, K. *et al.* High-throughput spatial mapping of single-cell RNA-seq data to tissue of origin. *Nat. Biotechnol.* **33**, 503–509 (2015).
8. Langfelder, P. & Horvath, S. WGCNA: an R package for weighted correlation network analysis. *BMC Bioinformatics* **9**, 559 (2008).
9. Eisen, M. B., Spellman, P. T., Brown, P. O. & Botstein, D. Cluster analysis and display of genome-wide expression patterns. *Proc. Natl. Acad. Sci. U. S. A.* **95**, 14863–14868 (1998).
10. Skinnider, M. A., Squair, J. W. & Foster, L. J. Evaluating measures of association for single-cell transcriptomics. *Nat. Methods* **16**, 381–386 (2019).
11. Stuart, J. M., Segal, E., Koller, D. & Kim, S. K. A gene-coexpression network for global discovery of conserved genetic modules. *Science* **302**, 249–255 (2003).
12. Marcotte, E. M., Pellegrini, M., Thompson, M. J., Yeates, T. O. & Eisenberg, D. A combined algorithm for genome-wide prediction of protein function. *Nature* **402**, 83–86 (1999).
13. Hughes, T. R. *et al.* Functional discovery via a compendium of expression profiles. *Cell*

102, 109–126 (2000).

14. Kim, S. K. *et al.* A gene expression map for Caenorhabditis elegans. *Science* **293**, 2087–2092 (2001).

15. Hartl, C. L. *et al.* Coexpression network architecture reveals the brain-wide and multiregional basis of disease susceptibility. *Nat. Neurosci.* **24**, 1313–1323 (2021).

16. DeRisi, J. L., Iyer, V. R. & Brown, P. O. Exploring the metabolic and genetic control of gene expression on a genomic scale. *Science* **278**, 680–686 (1997).

17. Jansen, R., Greenbaum, D. & Gerstein, M. Relating whole-genome expression data with protein-protein interactions. *Genome Res.* **12**, 37–46 (2002).

18. Szklarczyk, D. *et al.* The STRING database in 2023: protein-protein association networks and functional enrichment analyses for any sequenced genome of interest. *Nucleic Acids Res.* **51**, D638–D646 (2023).

19. Tavazoie, S., Hughes, J. D., Campbell, M. J., Cho, R. J. & Church, G. M. Systematic determination of genetic network architecture. *Nat. Genet.* **22**, 281–285 (1999).

20. Roth, F. P., Hughes, J. D., Estep, P. W. & Church, G. M. Finding DNA regulatory motifs within unaligned noncoding sequences clustered by whole-genome mRNA quantitation. *Nat. Biotechnol.* **16**, 939–945 (1998).

21. Nusinow, D. P. *et al.* Quantitative Proteomics of the Cancer Cell Line Encyclopedia. *Cell* **180**, 387–402.e16 (2020).

22. Gonçalves, E. *et al.* Pan-cancer proteomic map of 949 human cell lines. *Cancer Cell* **40**, 835–849.e8 (2022).

23. Kustatscher, G. *et al.* Co-regulation map of the human proteome enables identification of

protein functions. *Nat. Biotechnol.* **37**, 1361–1371 (2019).

24. Ryan, C. J., Kennedy, S., Bajrami, I., Matallanas, D. & Lord, C. J. A Compendium of Co-regulated Protein Complexes in Breast Cancer Reveals Collateral Loss Events. *Cell Syst* **5**, 399–409.e5 (2017).
25. Furlong, E. E. M. & Levine, M. Developmental enhancers and chromosome topology. *Science* **361**, 1341–1345 (2018).
26. Hnisz, D., Shrinivas, K., Young, R. A., Chakraborty, A. K. & Sharp, P. A. A Phase Separation Model for Transcriptional Control. *Cell* **169**, 13–23 (2017).
27. Grabowski, P., Kustatscher, G. & Rappsilber, J. Epigenetic Variability Confounds Transcriptome but Not Proteome Profiling for Coexpression-based Gene Function Prediction *. *Mol. Cell. Proteomics* **17**, 2082–2090 (2018).
28. Kustatscher, G., Grabowski, P. & Rappsilber, J. Pervasive coexpression of spatially proximal genes is buffered at the protein level. *Mol. Syst. Biol.* **13**, 937 (2017).
29. Sonenberg, N., Hershey, J. W. B. & Mathews, M. B. *Translational Control of Gene Expression*. (CSHL Press, 2001).
30. Kuersten, S. & Goodwin, E. B. The power of the 3’ UTR: translational control and development. *Nat. Rev. Genet.* **4**, 626–637 (2003).
31. Baker, S. A. & Rutter, J. Metabolites as signalling molecules. *Nat. Rev. Mol. Cell Biol.* **24**, 355–374 (2023).
32. Ozadam, H. *et al.* Single-cell quantification of ribosome occupancy in early mouse development. *Nature* **618**, 1057–1064 (2023).
33. King, R. W., Deshaies, R. J., Peters, J. M. & Kirschner, M. W. How proteolysis drives the

cell cycle. *Science* **274**, 1652–1659 (1996).

34. Rao, S. *et al.* Genes with 5' terminal oligopyrimidine tracts preferentially escape global suppression of translation by the SARS-CoV-2 Nsp1 protein. *RNA* **27**, 1025–1045 (2021).

35. Slobodin, B. *et al.* Cap-independent translation and a precisely located RNA sequence enable SARS-CoV-2 to control host translation and escape anti-viral response. *Nucleic Acids Res.* **50**, 8080–8092 (2022).

36. Singh, G., Pratt, G., Yeo, G. W. & Moore, M. J. The Clothes Make the mRNA: Past and Present Trends in mRNP Fashion. *Annu. Rev. Biochem.* **84**, 325–354 (2015).

37. Keene, J. D. & Tenenbaum, S. A. Eukaryotic mRNPs may represent posttranscriptional operons. *Mol. Cell* **9**, 1161–1167 (2002).

38. Keene, J. D. RNA regulons: coordination of post-transcriptional events. *Nat. Rev. Genet.* **8**, 533–543 (2007).

39. Wurth, L. *et al.* UNR/CSDE1 Drives a Post-transcriptional Program to Promote Melanoma Invasion and Metastasis. *Cancer Cell* **36**, 337 (2019).

40. Li, G.-W., Burkhardt, D., Gross, C. & Weissman, J. S. Quantifying absolute protein synthesis rates reveals principles underlying allocation of cellular resources. *Cell* **157**, 624–635 (2014).

41. Taggart, J. C. & Li, G.-W. Production of Protein-Complex Components Is Stoichiometric and Lacks General Feedback Regulation in Eukaryotes. *Cell Syst* **7**, 580–589.e4 (2018).

42. Ishikawa, K. Multilayered regulation of proteome stoichiometry. *Curr. Genet.* **67**, 883–890 (2021).

43. Amirbeigiarab, S. *et al.* Invariable stoichiometry of ribosomal proteins in mouse brain

tissues with aging. *Proc. Natl. Acad. Sci. U. S. A.* **116**, 22567–22572 (2019).

44. Soto, I. *et al.* Balanced mitochondrial and cytosolic translatomes underlie the biogenesis of human respiratory complexes. *Genome Biol.* **23**, 170 (2022).

45. Natan, E. *et al.* Cotranslational protein assembly imposes evolutionary constraints on homomeric proteins. *Nat. Struct. Mol. Biol.* **25**, 279–288 (2018).

46. Li, G.-W., Oh, E. & Weissman, J. S. The anti-Shine-Dalgarno sequence drives translational pausing and codon choice in bacteria. *Nature* **484**, 538–541 (2012).

47. Seidel, M. *et al.* Co-translational assembly orchestrates competing biogenesis pathways. *Nat. Commun.* **13**, 1224 (2022).

48. Bertolini, M. *et al.* Interactions between nascent proteins translated by adjacent ribosomes drive homomer assembly. *Science* **371**, 57–64 (2021).

49. van den Boogaart, K. G., Filzmoser, P., Hron, K., Templ, M. & Tolosana-Delgado, R. Classical and Robust Regression Analysis with Compositional Data. *Math. Geosci.* **53**, 823–858 (2021).

50. Quinn, T. P., Richardson, M. F., Lovell, D. & Crowley, T. M. propr: An R-package for Identifying Proportionally Abundant Features Using Compositional Data Analysis. *Sci. Rep.* **7**, 16252 (2017).

51. Ozadam, H., Geng, M. & Cenik, C. RiboFlow, RiboR and RiboPy: an ecosystem for analyzing ribosome profiling data at read length resolution. *Bioinformatics* **36**, 2929–2931 (2020).

52. Gerashchenko, M. V. & Gladyshev, V. N. Ribonuclease selection for ribosome profiling. *Nucleic Acids Res.* **45**, e6 (2017).

53. Mohammad, F., Green, R. & Buskirk, A. R. A systematically-revised ribosome profiling method for bacteria reveals pauses at single-codon resolution. *Elife* **8**, (2019).

54. Ingolia, N. T., Ghaemmaghami, S., Newman, J. R. S. & Weissman, J. S. Genome-wide analysis in vivo of translation with nucleotide resolution using ribosome profiling. *Science* **324**, 218–223 (2009).

55. Larsson, O., Sonenberg, N. & Nadon, R. Identification of differential translation in genome wide studies. *Proc. Natl. Acad. Sci. U. S. A.* **107**, 21487–21492 (2010).

56. Quinn, T. P. *et al.* A field guide for the compositional analysis of any-omics data. *Gigascience* **8**, (2019).

57. Sudmant, P. H., Alexis, M. S. & Burge, C. B. Meta-analysis of RNA-seq expression data across species, tissues and studies. *Genome Biol.* **16**, 287 (2015).

58. Wang, Z.-Y. *et al.* Transcriptome and translatome co-evolution in mammals. *Nature* **588**, 642–647 (2020).

59. Lu, P., Takai, K., Weaver, V. M. & Werb, Z. Extracellular matrix degradation and remodeling in development and disease. *Cold Spring Harb. Perspect. Biol.* **3**, (2011).

60. Artieri, C. G. & Fraser, H. B. Evolution at two levels of gene expression in yeast. *Genome Res.* **24**, 411–421 (2014).

61. McManus, C. J., May, G. E., Spealman, P. & Shteyman, A. Ribosome profiling reveals post-transcriptional buffering of divergent gene expression in yeast. *Genome Res.* **24**, 422–430 (2014).

62. Wang, M., Herrmann, C. J., Simonovic, M., Szklarczyk, D. & von Mering, C. Version 4.0 of PaxDb: Protein abundance data, integrated across model organisms, tissues, and cell-

lines. *Proteomics* **15**, 3163–3168 (2015).

63. Breschi, A., Gingeras, T. R. & Guigó, R. Comparative transcriptomics in human and mouse. *Nat. Rev. Genet.* **18**, 425–440 (2017).

64. Crow, M., Suresh, H., Lee, J. & Gillis, J. Coexpression reveals conserved gene programs that co-vary with cell type across kingdoms. *Nucleic Acids Res.* **50**, 4302–4314 (2022).

65. Thoreen, C. C. *et al.* A unifying model for mTORC1-mediated regulation of mRNA translation. *Nature* **485**, 109–113 (2012).

66. Pierson, E. *et al.* Sharing and Specificity of Co-expression Networks across 35 Human Tissues. *PLoS Comput. Biol.* **11**, e1004220 (2015).

67. Kershaw, C. J. *et al.* Translation factor and RNA binding protein mRNA interactomes support broader RNA regulons for posttranscriptional control. *J. Biol. Chem.* **299**, 105195 (2023).

68. Hentze, M. W., Castello, A., Schwarzl, T. & Preiss, T. A brave new world of RNA-binding proteins. *Nat. Rev. Mol. Cell Biol.* **19**, 327–341 (2018).

69. Philippe, L., van den Elzen, A. M. G., Watson, M. J. & Thoreen, C. C. Global analysis of LARP1 translation targets reveals tunable and dynamic features of 5′ TOP motifs. *Proceedings of the National Academy of Sciences* **117**, 5319–5328 (2020).

70. Song, K. Y., Choi, H. S., Law, P.-Y., Wei, L.-N. & Loh, H. H. Vimentin interacts with the 5’-untranslated region of mouse mu opioid receptor (MOR) and is required for post-transcriptional regulation. *RNA Biol.* **10**, 256–266 (2013).

71. Hsieh, A. C. *et al.* The translational landscape of mTOR signalling steers cancer initiation and metastasis. *Nature* **485**, 55–61 (2012).

72. Korbel, J. O., Jensen, L. J., von Mering, C. & Bork, P. Analysis of genomic context: prediction of functional associations from conserved bidirectionally transcribed gene pairs. *Nat. Biotechnol.* **22**, 911–917 (2004).

73. Szklarczyk, R. *et al.* WeGET: predicting new genes for molecular systems by weighted co-expression. *Nucleic Acids Res.* **44**, D567–73 (2016).

74. Zhang, M. *et al.* RNA-binding protein IMP3 is a novel regulator of MEK1/ERK signaling pathway in the progression of colorectal Cancer through the stabilization of MEKK1 mRNA. *J. Exp. Clin. Cancer Res.* **40**, 200 (2021).

75. Cargnello, M. & Roux, P. P. Activation and function of the MAPKs and their substrates, the MAPK-activated protein kinases. *Microbiol. Mol. Biol. Rev.* **75**, 50–83 (2011).

76. Bodén, M. & Bailey, T. L. Associating transcription factor-binding site motifs with target GO terms and target genes. *Nucleic Acids Res.* **36**, 4108–4117 (2008).

77. Machanick, P. & Bailey, T. L. MEME-ChIP: motif analysis of large DNA datasets. *Bioinformatics* **27**, 1696–1697 (2011).

78. Eichhorn, S. W. *et al.* mRNA destabilization is the dominant effect of mammalian microRNAs by the time substantial repression ensues. *Mol. Cell* **56**, 104–115 (2014).

79. Bartel, D. P. Metazoan MicroRNAs. *Cell* **173**, 20–51 (2018).

80. Benoit Bouvrette, L. P., Bovaird, S., Blanchette, M. & Lécuyer, E. oRNAment: a database of putative RNA binding protein target sites in the transcriptomes of model species. *Nucleic Acids Res.* **48**, D166–D173 (2020).

81. Krismer, K. *et al.* Transite: A Computational Motif-Based Analysis Platform That Identifies RNA-Binding Proteins Modulating Changes in Gene Expression. *Cell Rep.* **32**, 108064

(2020).

82. Van Nostrand, E. L. *et al.* A large-scale binding and functional map of human RNA-binding proteins. *Nature* **583**, 711–719 (2020).

83. Mecham, R. *The Extracellular Matrix: An Overview*. (Springer Science & Business Media, 2011).

84. Kagan, H. M. & Li, W. Lysyl oxidase: properties, specificity, and biological roles inside and outside of the cell. *J. Cell. Biochem.* **88**, 660–672 (2003).

85. Kikuchi, A. *et al.* Structural basis for activation of DNMT1. *Nat. Commun.* **13**, 7130 (2022).

86. Wu, Y.-Y. *et al.* The hTERT-p50 homodimer inhibits PLEKHA7 expression to promote gastric cancer invasion and metastasis. *Oncogene* **42**, 1144–1156 (2023).

87. Kurita, S., Yamada, T., Rikitsu, E., Ikeda, W. & Takai, Y. Binding between the junctional proteins afadin and PLEKHA7 and implication in the formation of adherens junction in epithelial cells. *J. Biol. Chem.* **288**, 29356–29368 (2013).

88. Pulimeno, P., Paschoud, S. & Citi, S. A role for ZO-1 and PLEKHA7 in recruiting paracingulin to tight and adherens junctions of epithelial cells. *J. Biol. Chem.* **286**, 16743–16750 (2011).

89. Jeung, H.-C. *et al.* PLEKHA7 signaling is necessary for the growth of mutant KRAS driven colorectal cancer. *Exp. Cell Res.* **409**, 112930 (2021).

90. Tavano, S. *et al.* Insm1 Induces Neural Progenitor Delamination in Developing Neocortex via Downregulation of the Adherens Junction Belt-Specific Protein Plekha7. *Neuron* **97**, 1299–1314.e8 (2018).

91. Sukonina, V. *et al.* FOXK1 and FOXK2 regulate aerobic glycolysis. *Nature* **566**, 279–283

(2019).

92. Kobe, B. & Kajava, A. V. The leucine-rich repeat as a protein recognition motif. *Curr. Opin. Struct. Biol.* **11**, 725–732 (2001).

93. Evans, R. *et al.* Protein complex prediction with AlphaFold-Multimer. *bioRxiv* 2021.10.04.463034 (2021) doi:10.1101/2021.10.04.463034.

94. Carlsson, P. & Mahlapuu, M. Forkhead transcription factors: key players in development and metabolism. *Dev. Biol.* **250**, 1–23 (2002).

95. The Human Transcription Factors. http://humantfs.ccbr.utoronto.ca/cite.php.

96. Hou, Y., Xie, T., He, L., Tao, L. & Huang, J. Topological links in predicted protein complex structures reveal limitations of AlphaFold. *Commun Biol* **6**, 1098 (2023).

97. Burke, D. F. *et al.* Towards a structurally resolved human protein interaction network. *Nat. Struct. Mol. Biol.* **30**, 216–225 (2023).

98. Bryant, P., Pozzati, G. & Elofsson, A. Improved prediction of protein-protein interactions using AlphaFold2. *Nat. Commun.* **13**, 1265 (2022).

99. Lambert, S. A. *et al.* The Human Transcription Factors. *Cell* **172**, 650–665 (2018).

100. Szklarczyk, D. *et al.* STRING v10: protein-protein interaction networks, integrated over the tree of life. *Nucleic Acids Res.* **43**, D447–52 (2015).

101. Shiber, A. *et al.* Cotranslational assembly of protein complexes in eukaryotes revealed by ribosome profiling. *Nature* **561**, 268–272 (2018).

102. Ewing, R. M. *et al.* Large-scale mapping of human protein–protein interactions by mass spectrometry. *Mol. Syst. Biol.* **3**, 89 (2007).

103. Drew, K., Wallingford, J. B. & Marcotte, E. M. hu.MAP 2.0: integration of over 15,000

proteomic experiments builds a global compendium of human multiprotein assemblies. *Mol. Syst. Biol.* **17**, e10016 (2021).

104. Heider, M. R. *et al.* Subunit connectivity, assembly determinants and architecture of the yeast exocyst complex. *Nat. Struct. Mol. Biol.* **23**, 59–66 (2016).

105. Kee, Y. *et al.* Subunit structure of the mammalian exocyst complex. *Proc. Natl. Acad. Sci. U. S. A.* **94**, 14438–14443 (1997).

106. Lalanne, J.-B. *et al.* Evolutionary Convergence of Pathway-Specific Enzyme Expression Stoichiometry. *Cell* **173**, 749–761.e38 (2018).

107. Cenik, C. *et al.* Integrative analysis of RNA, translation, and protein levels reveals distinct regulatory variation across humans. *Genome Res.* **25**, 1610–1621 (2015).

108. Mills, E. W. & Green, R. Ribosomopathies: There's strength in numbers. *Science* **358**, (2017).

109. Zheng, D. *et al.* Predicting the translation efficiency of messenger RNA in mammalian cells. *bioRxiv* 2024.08.11.607362 (2024) doi:10.1101/2024.08.11.607362.

110. Bicknell, A. A. *et al.* Attenuating ribosome load improves protein output from mRNA by limiting translation-dependent mRNA decay. *Cell Rep.* **43**, 114098 (2024).

111. Liu, T.-Y. *et al.* Time-Resolved Proteomics Extends Ribosome Profiling-Based Measurements of Protein Synthesis Dynamics. *Cell Syst* **4**, 636–644.e9 (2017).

112. Piepoli, A. *et al.* The expression of leucine-rich repeat gene family members in colorectal cancer. *Exp. Biol. Med.* **237**, 1123–1128 (2012).

113. Liu, Y. *et al.* Identification of differential expression of genes in hepatocellular carcinoma by suppression subtractive hybridization combined cDNA microarray. *Oncol. Rep.* **18**, 943–

951 (2007).

114. Chen, H. *et al.* miR-218 contributes to drug resistance in multiple myeloma via targeting LRRC28. *J. Cell. Biochem.* **122**, 305–314 (2021).

115. Vander Heiden, M. G., Cantley, L. C. & Thompson, C. B. Understanding the Warburg effect: the metabolic requirements of cell proliferation. *Science* **324**, 1029–1033 (2009).

116. Liu, Y. *et al.* Histone H2AX promotes metastatic progression by preserving glycolysis via hexokinase-2. *Sci. Rep.* **12**, 3758 (2022).

117. Rodriguez, J. M. *et al.* APPRIS: annotation of principal and alternative splice isoforms. *Nucleic Acids Res.* **41**, D110–7 (2013).

118. ChatGPT. https://chat.openai.com.

119. *Sra-Tools: SRA Tools*. (Github).

120. Martin, M. Cutadapt removes adapter sequences from high-throughput sequencing reads. *EMBnet.journal* **17**, 10–12 (2011).

121. Langmead, B. & Salzberg, S. L. Fast gapped-read alignment with Bowtie 2. *Nat. Methods* **9**, 357–359 (2012).

122. Creators Liu, O. *HeLa Ribosome Profiling Data*. doi:10.5281/zenodo.10594392.

123. Gerashchenko, M. V. & Gladyshev, V. N. Translation inhibitors cause abnormalities in ribosome profiling experiments. *Nucleic Acids Res.* **42**, e134 (2014).

124. Wu, C. C.-C., Zinshteyn, B., Wehner, K. A. & Green, R. High-Resolution Ribosome Profiling Defines Discrete Ribosome Elongation States and Translational Regulation during Cellular Stress. *Mol. Cell* **73**, 959–970.e5 (2019).

125. Wolin, S. L. & Walter, P. Ribosome pausing and stacking during translation of a eukaryotic

mRNA. *EMBO J.* **7**, 3559–3569 (1988).

126. Sharma, J. *et al.* A small molecule that induces translational readthrough of CFTR nonsense mutations by eRF1 depletion. *Nat. Commun.* **12**, 4358 (2021).

127. Tukey, J. W. The Future of Data Analysis. *Ann. Math. Stat.* **33**, 1–67 (1962).

128. Zhang, X.-O., Yin, Q.-F., Chen, L.-L. & Yang, L. Gene expression profiling of non-polyadenylated RNA-seq across species. *Genom Data* **2**, 237–241 (2014).

129. Yang, L., Duff, M. O., Graveley, B. R., Carmichael, G. G. & Chen, L.-L. Genomewide characterization of non-polyadenylated RNAs. *Genome Biol.* **12**, R16 (2011).

130. van den Boogaart, K. G. & Tolosana-Delgado, R. *Analyzing Compositional Data with R.* (Springer Berlin Heidelberg).

131. Greenacre, M. Compositional data analysis. *Annu. Rev. Stat. Appl.* **8**, 271–299 (2021).

132. Ramsköld, D., Wang, E. T., Burge, C. B. & Sandberg, R. An abundance of ubiquitously expressed genes revealed by tissue transcriptome sequence data. *PLoS Comput. Biol.* **5**, e1000598 (2009).

133. Csárdi, G., Franks, A., Choi, D. S., Airoldi, E. M. & Drummond, D. A. Accounting for experimental noise reveals that mRNA levels, amplified by post-transcriptional processes, largely determine steady-state protein levels in yeast. *PLoS Genet.* **11**, e1005206 (2015).

134. orthogene. *Bioconductor* https://bioconductor.org/packages/release/bioc/html/orthogene.html.

135. van den Boogaart, K. G. & Tolosana-Delgado, R. ‘compositions’: A unified R package to analyze compositional data. *Comput. Geosci.* **34**, 320–338 (2008).

136. Kim, S. ppcor: An R Package for a Fast Calculation to Semi-partial Correlation

Coefficients. *Commun Stat Appl Methods* **22**, 665–674 (2015).

137. Berriz, G. F., Beaver, J. E., Cenik, C., Tasan, M. & Roth, F. P. Next generation software for functional trend analysis. *Bioinformatics* **25**, 3043–3044 (2009).

138. Buttrey, S. & Whitaker, L. TreeClust: An R package for tree-based clustering dissimilarities. *R J.* **7**, 227 (2015).

139. Wainberg, M. *et al.* A genome-wide atlas of co-essential modules assigns function to uncharacterized genes. *Nat. Genet.* **53**, 638–649 (2021).

140. Gene Ontology Consortium *et al.* The Gene Ontology knowledgebase in 2023. *Genetics* **224**, (2023).

141. Ballouz, S., Weber, M., Pavlidis, P. & Gillis, J. EGAD: ultra-fast functional analysis of gene networks. *Bioinformatics* **33**, 612–614 (2017).

142. Carlson, M. org. Mm. eg. db: Genome wide annotation for Mouse. R package version 3.8. 2. 2019.

143. Carlson, M. org. Hs. eg. db: Genome wide annotation for Human. R package version 3.8. 2. 2019.

144. Jumper, J. *et al.* Highly accurate protein structure prediction with AlphaFold. *Nature* **596**, 583–589 (2021).

145. UniProt Consortium. UniProt: the Universal Protein Knowledgebase in 2023. *Nucleic Acids Res.* **51**, D523–D531 (2023).

146. Hu, Y. *et al.* Paralog Explorer: A resource for mining information about paralogs in common research organisms. *Comput. Struct. Biotechnol. J.* **20**, 6570–6577 (2022).

147. Quinlan, A. R. & Hall, I. M. BEDTools: a flexible suite of utilities for comparing genomic

features. *Bioinformatics* **26**, 841–842 (2010).

148. Stuart, E. A., King, G., Imai, K. & Ho, D. MatchIt: nonparametric preprocessing for parametric causal inference. *J. Stat. Softw.* (2011).

149. Sanson, K. R. *et al.* Optimized libraries for CRISPR-Cas9 genetic screens with multiple modalities. *Nat. Commun.* **9**, 5416 (2018).

150. Sanjana, N. E., Shalem, O. & Zhang, F. Improved vectors and genome-wide libraries for CRISPR screening. *Nat. Methods* **11**, 783–784 (2014).

151. Rossi, G. P. *et al.* Endothelin-1 stimulates steroid secretion of human adrenocortical cells ex vivo via both ETA and ETB receptor subtypes. *J. Clin. Endocrinol. Metab.* **82**, 3445–3449 (1997).

152. Sánchez-Caballero, L. *et al.* TMEM70 functions in the assembly of complexes I and V. *Biochim. Biophys. Acta Bioenerg.* **1861**, 148202 (2020).

153. Carroll, J., He, J., Ding, S., Fearnley, I. M. & Walker, J. E. TMEM70 and TMEM242 help to assemble the rotor ring of human ATP synthase and interact with assembly factors for complex I. *Proc. Natl. Acad. Sci. U. S. A.* **118**, (2021).

154. Mii, Y. & Takada, S. Heparan Sulfate Proteoglycan Clustering in Wnt Signaling and Dispersal. *Front Cell Dev Biol* **8**, 631 (2020).

155. Kamimura, K. *et al.* Perlecan regulates bidirectional Wnt signaling at the Drosophila neuromuscular junction. *J. Cell Biol.* **200**, 219–233 (2013).

156. Camlin, N. J., McLaughlin, E. A. & Holt, J. E. Kif4 Is Essential for Mouse Oocyte Meiosis. *PLoS One* **12**, e0170650 (2017).

157. Tang, F. *et al.* Involvement of Kif4a in Spindle Formation and Chromosome Segregation in

Mouse Oocytes. *Aging Dis.* **9**, 623–633 (2018).

158. Robertson, A. K., Geiman, T. M., Sankpal, U. T., Hager, G. L. & Robertson, K. D. Effects of chromatin structure on the enzymatic and DNA binding functions of DNA methyltransferases DNMT1 and Dnmt3a in vitro. *Biochem. Biophys. Res. Commun.* **322**, 110–118 (2004).

159. Schrader, A., Gross, T., Thalhammer, V. & Längst, G. Characterization of Dnmt1 Binding and DNA Methylation on Nucleosomes and Nucleosomal Arrays. *PLoS One* **10**, e0140076 (2015).

160. Ciossani, G. *et al.* The kinetochore proteins CENP-E and CENP-F directly and specifically interact with distinct BUB mitotic checkpoint Ser/Thr kinases. *J. Biol. Chem.* **293**, 10084–10101 (2018).

161. Liao, H., Winkfein, R. J., Mack, G., Rattner, J. B. & Yen, T. J. CENP-F is a protein of the nuclear matrix that assembles onto kinetochores at late G2 and is rapidly degraded after mitosis. *J. Cell Biol.* **130**, 507–518 (1995).

162. Chen, M. *et al.* FAT1 inhibits the proliferation and metastasis of cervical cancer cells by binding β-catenin. *Int. J. Clin. Exp. Pathol.* **12**, 3807–3818 (2019).

163. Nishikawa, Y. *et al.* Human FAT1 cadherin controls cell migration and invasion of oral squamous cell carcinoma through the localization of β-catenin. *Oncol. Rep.* **26**, 587–592 (2011).

164. Morris, L. G. T. *et al.* Recurrent somatic mutation of FAT1 in multiple human cancers leads to aberrant Wnt activation. *Nat. Genet.* **45**, 253–261 (2013).

165. Hou, R., Liu, L., Anees, S., Hiroyasu, S. & Sibinga, N. E. S. The Fat1 cadherin integrates

vascular smooth muscle cell growth and migration signals. *J. Cell Biol.* **173**, 417–429 (2006).

166. Vallet, S. D., Berthollier, C., Salza, R., Muller, L. & Ricard-Blum, S. The Interactome of Cancer-Related Lysyl Oxidase and Lysyl Oxidase-Like Proteins. *Cancers* **13**, (2020).

167. Vallet, S. D. *et al.* Insights into the structure and dynamics of lysyl oxidase propeptide, a flexible protein with numerous partners. *Sci. Rep.* **8**, 11768 (2018).

168. Yang, C. *et al.* Transcriptomic Analysis Identified ARHGAP Family as a Novel Biomarker Associated With Tumor-Promoting Immune Infiltration and Nanomechanical Characteristics in Bladder Cancer. *Front Cell Dev Biol* **9**, 657219 (2021).

169. Lamarche-Vane, N. & Hall, A. CdGAP, a novel proline-rich GTPase-activating protein for Cdc42 and Rac. *J. Biol. Chem.* **273**, 29172–29177 (1998).

170. Yang, S. *et al.* Control of antiviral innate immune response by protein geranylgeranylation. *Sci Adv* **5**, eaav7999 (2019).

171. Bouhaddou, M. *et al.* The Global Phosphorylation Landscape of SARS-CoV-2 Infection. *Cell* **182**, 685–712.e19 (2020).

172. Swaine, T. & Dittmar, M. T. CDC42 Use in Viral Cell Entry Processes by RNA Viruses. *Viruses* **7**, 6526–6536 (2015).

173. Redmond, S. A. *et al.* Somatodendritic Expression of JAM2 Inhibits Oligodendrocyte Myelination. *Neuron* **91**, 824–836 (2016).

174. Skoufos, G. *et al.* TarBase-v9.0 extends experimentally supported miRNA-gene interactions to cell-types and virally encoded miRNAs. *Nucleic Acids Res.* **52**, D304–D310 (2024).

175. Miettinen, T. P. & Björklund, M. Modified ribosome profiling reveals high abundance of

ribosome protected mRNA fragments derived from 3' untranslated regions. *Nucleic Acids Res.* **43**, 1019–1034 (2015).

176. van der Brug, M. P. *et al.* RNA binding activity of the recessive parkinsonism protein DJ-1 supports involvement in multiple cellular pathways. *Proc. Natl. Acad. Sci. U. S. A.* **105**, 10244–10249 (2008).

177. Niere, F. *et al.* Aberrant DJ-1 expression underlies L-type calcium channel hypoactivity in dendrites in tuberous sclerosis complex and Alzheimer's disease. *Proc. Natl. Acad. Sci. U. S. A.* **120**, e2301534120 (2023).

178. Jin, W. *et al.* HydRA: Deep-learning models for predicting RNA-binding capacity from protein interaction association context and protein sequence. *Mol. Cell* **83**, 2595–2611.e11 (2023).

179. Avsec, Ž. *et al.* Effective gene expression prediction from sequence by integrating long-range interactions. *Nat. Methods* **18**, 1196–1203 (2021).

180. Agarwal, V. & Shendure, J. Predicting mRNA abundance directly from genomic sequence using deep convolutional neural networks. *Cell Rep.* **31**, 107663 (2020).

181. Dong, X., Li, C., Chen, Y., Ding, G. & Li, Y. Human transcriptional interactome of chromatin contribute to gene co-expression. *BMC Genomics* **11**, 704 (2010).

182. Zhang, K., Wang, C., Sun, L. & Zheng, J. Prediction of gene co-expression from chromatin contacts with graph attention network. *Bioinformatics* **38**, 4457–4465 (2022).

183. Blum, M. *et al.* The InterPro protein families and domains database: 20 years on. *Nucleic Acids Res.* **49**, D344–D354 (2021).

184. Cock, P. J. A. *et al.* Biopython: freely available Python tools for computational molecular

biology and bioinformatics. *Bioinformatics* **25**, 1422–1423 (2009).

Table 1: Literature support for gene functions predicted using TEC.

In the table, we list the predictions that are supported by literature. To do the new gene function prediction, we selected GO terms with AUROC measured with TEC >=0.8, then focused on the subset with differences between AUROC measured with TEC and RNA co-expression >= 0.1.

Term	Species	Description	New adding gene (top ranking in TE)	TEC AUROC	RNA co-expression AUROC	Ranking of new adding gene in RNA	Reference
GO:0005496	Human	steroid binding	EDNRA	0.81	0.50	3991	[151]
GO:0022900	Human	electron transport chain	TMEM70	0.82	0.67	1611	[152,153]
GO:0042813	Human	Wnt-activated receptor activity	HSPG2	0.85	0.74	341	[154,155]
GO:0007129	Human	homologous chromosome pairing at meiosis	KIF4A	0.84	0.73	11	[156,157]
GO:0031492	Human	nucleosomal DNA binding	DNMT1	0.85	0.73	251	[85,158,159]
GO:0050793	Mouse	regulation of developmental	Plekha7	0.85	0.70	3929	[86–90]

Term	Species	Description	New adding gene (top ranking in TE)	TEC AUROC	RNA co-expression AUROC	Ranking of new adding gene in RNA	Reference
		process					
GO:1990023	Mouse	mitotic spindle midzone	Cenpf	0.90	0.74	54	[160,161]
GO:0016342	Mouse	catenin complex	Fat1	0.85	0.73	781	[162–165]
GO:0005539	Mouse	glycosaminoglycan binding	Lox	0.95	0.83	32	[166,167]
GO:0140374	Mouse	antiviral innate immune response	Arhgap31	0.84	0.73	1085	[168–172]
GO:0022010	Mouse	Central nervous system myelination	Jam2	0.88	0.76	584	[173]

Extended Figures

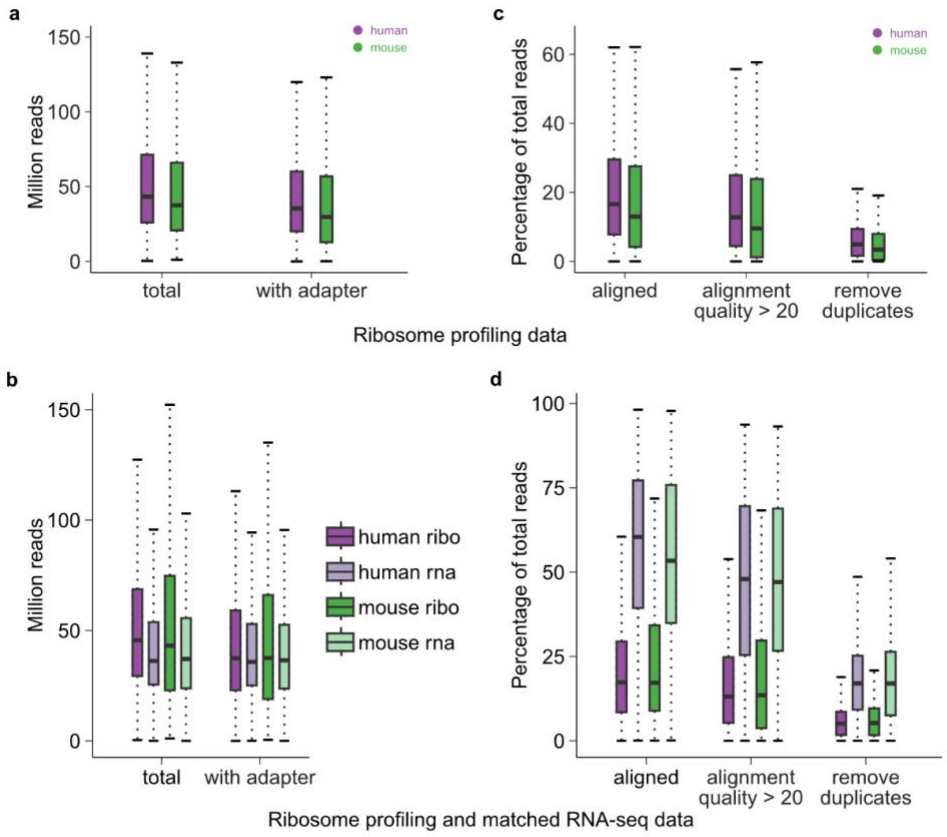

ExtendedDataFig. 1 | Sequencing quality of ribosome profiling data with matched RNA-seq data when available (supplementary text): a, Distribution of read counts for ribosome profiling data in RiboBase. In all figure panels, the horizontal line corresponds to the median. The box represents the interquartile range and the whiskers extend to 1.5 times of it. **b,** Distribution plot similar to panel A for ribosome profiling data with matched RNA-seq. **c,** Distribution of the proportion of read count aligned to transcripts, read counts with high-quality alignments, and the percentage of reads remaining after PCR deduplication, relative to the total number of reads from panel A. **d,** Similar plot as panel C for ribosome profiling with matched RNA-seq.

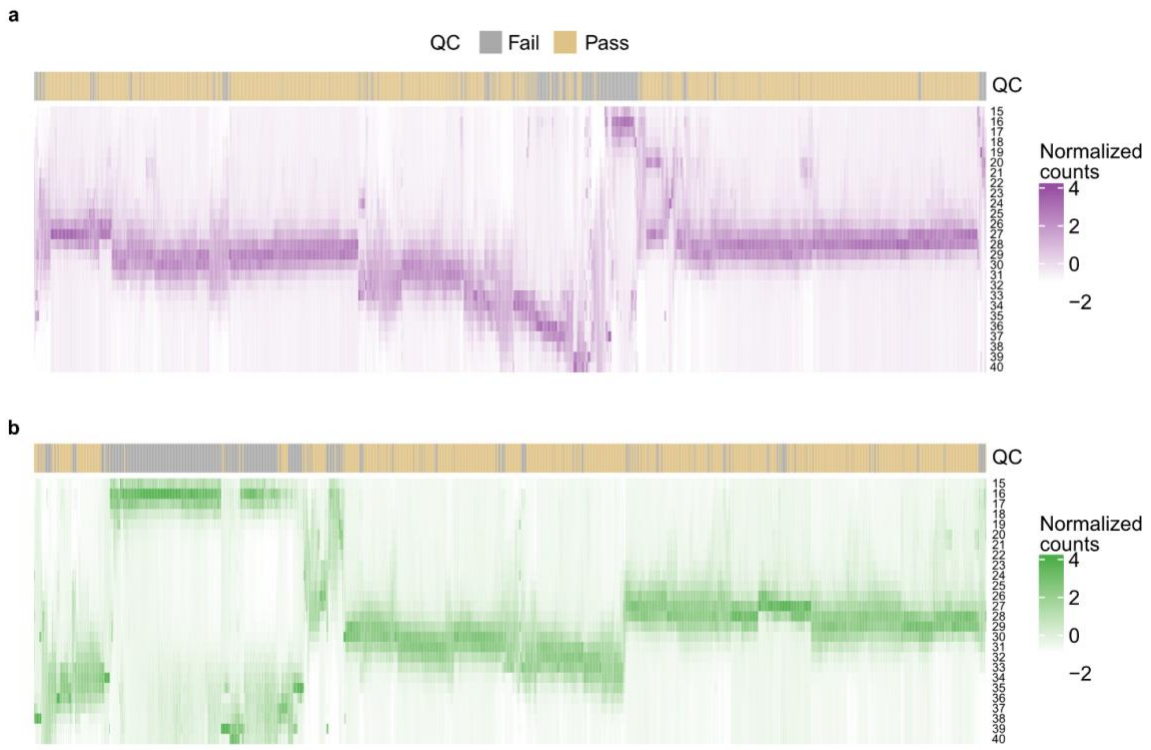

ExtendedDataFig. 2 | Length distribution of RPFs for human and mouse samples: a, The read length distribution of RPFs aligned to coding sequences for all human experiments. The color in the heatmap represents the z-score adjusted RPF counts (Methods). Each experiment where the percentage of RPFs mapping to CDS was greater than 70% and achieving sufficient coverage of the transcript (>= 0.1X) was annotated as QC-pass. **b,** Similar to panel A for mouse samples.

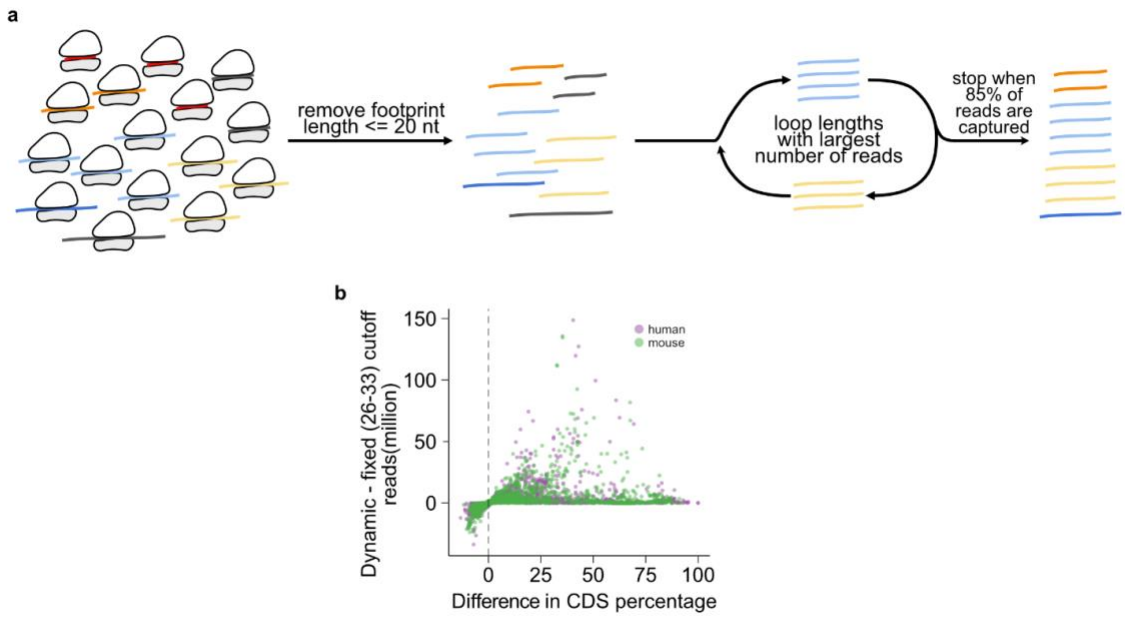

ExtendedDataFig. 3 | Schematic for method to select range of RPF lengths: a, RPFs shorter than 21 nucleotides were removed, then we identified the RPF length with the highest number of reads mapping to CDS to serve as the starting point. Subsequently, we compared one nucleotide longer or shorter than the first and chose the length with the most reads again. This looping process continued until at least 85% of the total CDS mapping RPFs were included. **b,** We compared the usable reads selected with two different boundary cutoffs (y-axis) and the proportion of these selected reads that map to the coding regions (x-axis) for each ribosome profiling experiment.

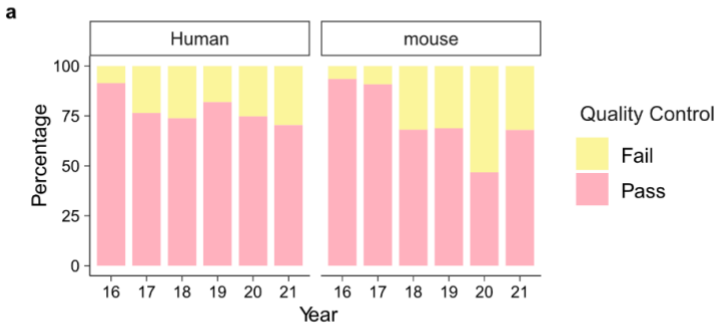

ExtendedDataFig. 4 | Data quality of ribosome profiling experiments from 2016 to 2021: a, The percentage of ribosome profiling experiments from GEO that pass or fail quality control (the percentage of RPFs mapping to CDS was greater than 70% and achieving at least 0.1X coverage of the transcript as QC pass).

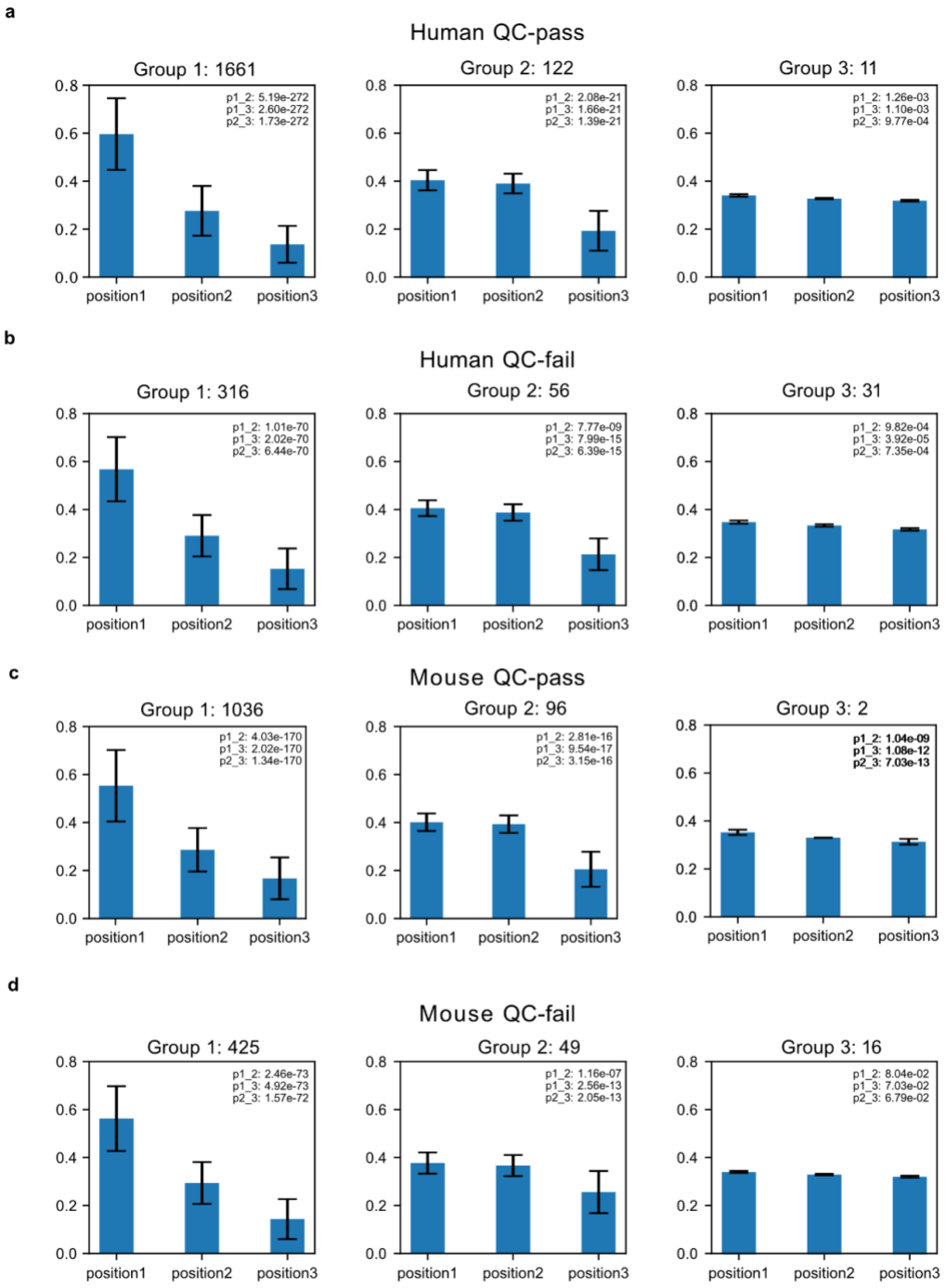

ExtendedDataFig. 5 | Three nucleotide periodicity of ribosome profiling data: a-d, In ribosome profiling experiments from RiboBase, samples were classified according to distinct

periodicity patterns (Methods). For all figure panels, we added error bars to represent the standard deviation across samples. Statistical significance was assessed using the Wilcoxon test, and the p-values were subsequently adjusted for all 33 comparisons using the Benjamini-Hochberg method. We considered the Group 1 pattern as indicative of the expected three-nucleotide periodicity patterns.

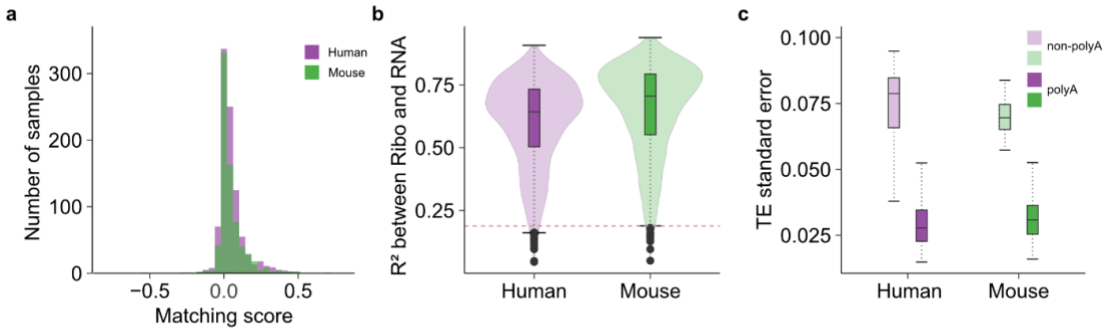

ExtendedDataFig. 6 | Validation of ribosome profiling and RNA-seq matching and gene selection for TE calculation: a, We calculated the coefficient of determination (R^2) between a specific ribosome profiling experiment and its corresponding RNA-seq from RiboBase. Additionally, we determined the average R^2 for all other pairings for the same ribosome profiling sample with other RNA-seq data from the same study. The matching score represents the difference in R^2 values between these two (x-axis; Methods). **b,** A dashed line at 0.188 serves as the threshold to identify samples with poor matching. In each figure panel containing boxplots, the horizontal line corresponds to the median. The box represents the IQR and the whiskers extend to 1.5 times of it. **c,** Distribution of standard error of TE values across tissue and cell lines (y-axis) for genes with polyA and without polyA tails.

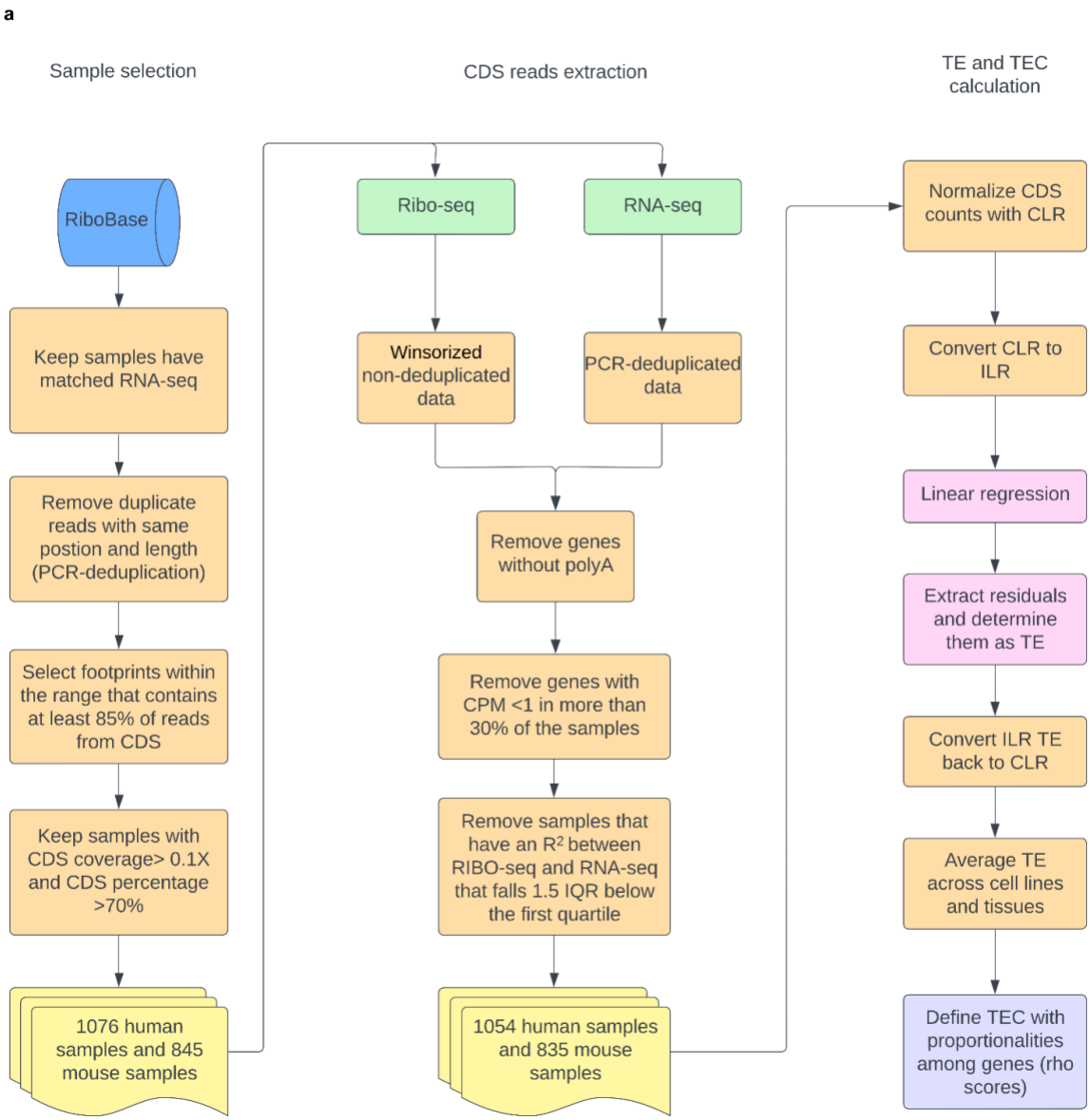

ExtendedDataFig. 7 | Detailed workflow of data processing for TE and TEC calculations: a, We selected ribosome profiling data with matched RNA-seq and removed duplicated reads with identical positions and lengths (PCR-deduplication). We set the RPF read length range for individual samples with our dynamic cutoff and filtered out ribosome profiling experiments that failed quality control. After selecting high-quality samples, we reprocessed all these ribosome profiling experiments using the winsorization method with non-deduplicated data. We removed genes without polyA tails and kept genes with sufficient counts per million RPFs. After obtaining RPF counts from the coding regions for both ribosome profiling and RNA-seq, we performed CLR

normalization and compositional linear regression, defining the residuals as TE for each gene in each sample. We averaged this sample-level TE based on cell lines and tissues. TEC is further calculated with rho scores[50]. To build an RNA co-expression matrix, we transformed CDS counts from RNA-seq experiments using CLR, averaged them based on cell lines and tissue, and calculated pairwise proportionalities (rho scores).

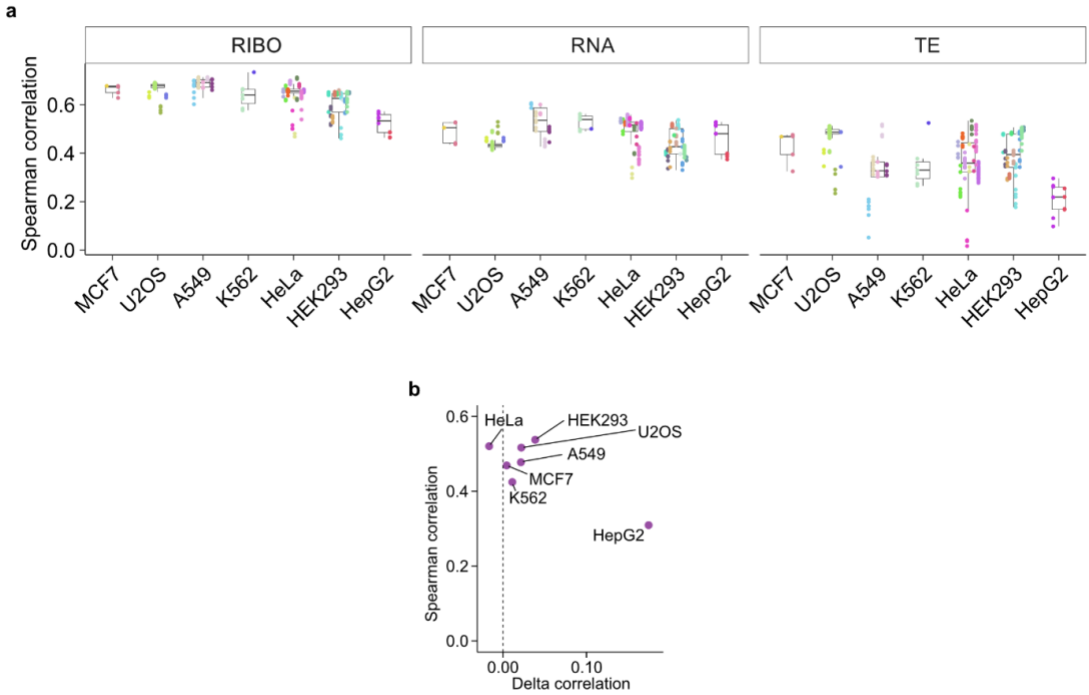

ExtendedDataFig. 8 | Spearman correlation between TE and protein abundance: a, The correlation between protein abundance and clr-transformed RPF counts from ribosome profiling (left), clr-transformed read counts from RNA-seq (middle), or TE calculated with winsorized RPFs counts using the linear regression model (right). Individual dots indicate specific experiments colored according to study. In the boxplot, the horizontal line corresponds to the median. The box represents the IQR and the whiskers extend to 1.5 times of this range. **b,** TE was calculated with winsorized RPF counts without deduplication or with deduplication based on position and fragment length. The Spearman correlation coefficient between TE calculated with winsorized RPF counts and protein abundance[62] (y-axis) was plotted against "delta correlation" (x-axis) defined by subtracting the correlation values obtained with PCR deduplication from those obtained with the method using winsorized RPF counts without deduplication.

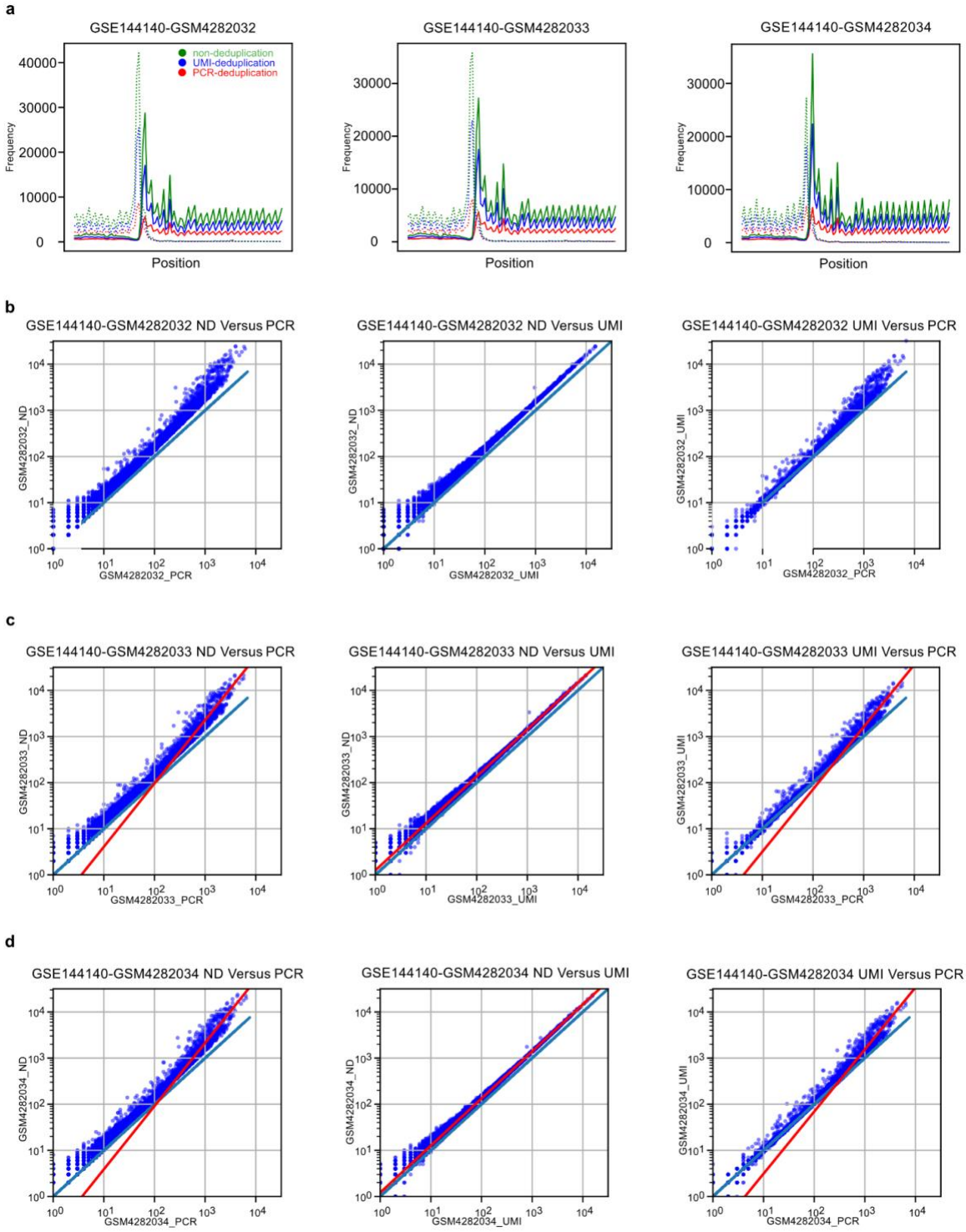

ExtendedDataFig. 9 | PCR vs. UMI deduplication comparison for GSE144140: a, Metagene

plots centered on the start codon for samples GSM4282032 (RPFs range: 28-36 nt), GSM4282033 (RPFs range: 28-36 nt range), and GSM4282034 (RPFs range: 26-35 nt range) were plotted using three different deduplication methods: non-deduplication (ND), UMI-deduplication (UMI), and PCR-deduplication (PCR). **b,** Correlation of gene counts for GSM4282032 between the three deduplication methods. A blue diagonal line represents a 1:1 ratio in all figure panels. Same analysis as panel b for GSM4282033 **c,** and GSM4282034 **d**.

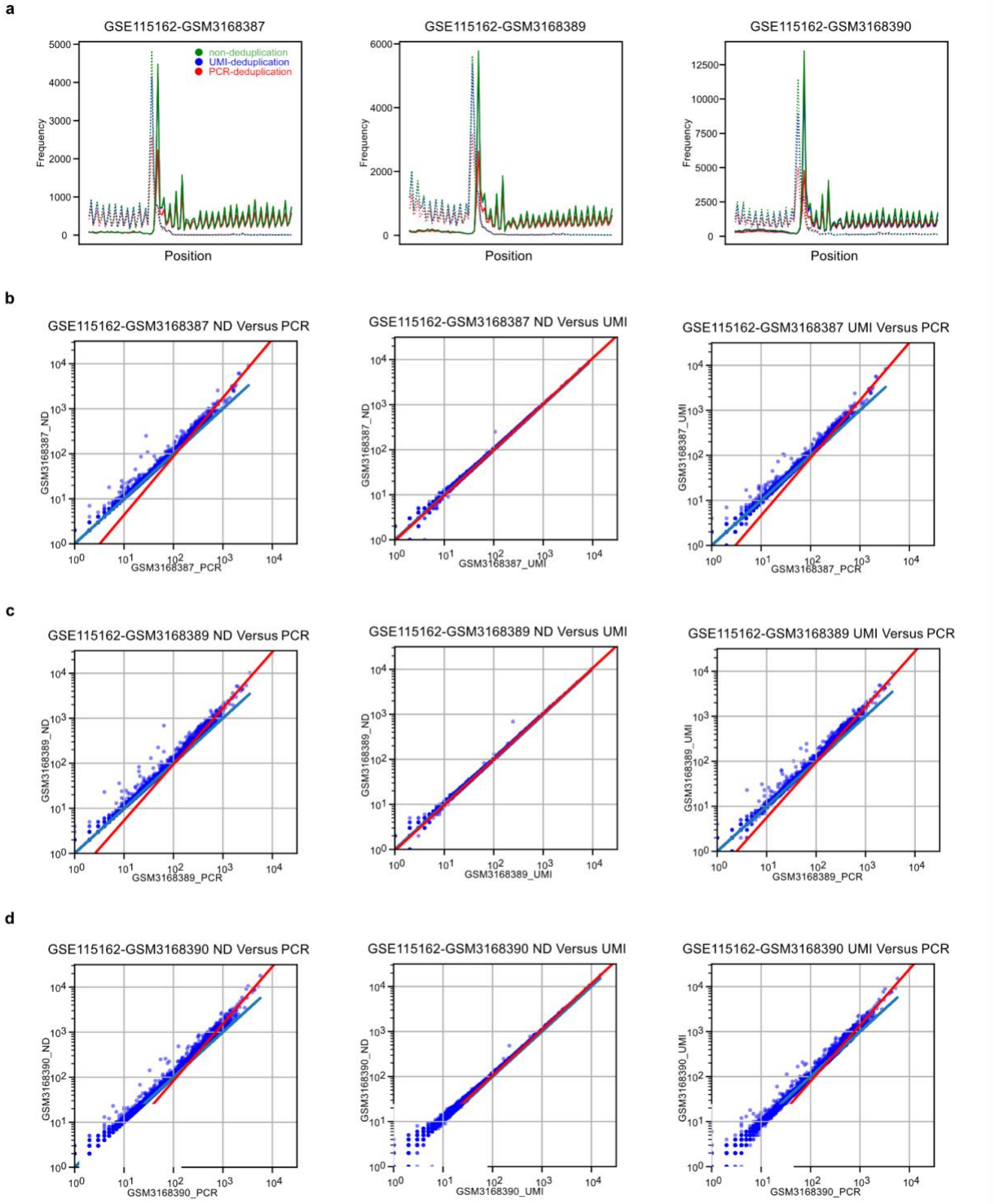

ExtendedDataFig. 10 | PCR vs. UMI deduplication comparison for GSE115162: Similar analysis as ExtendedDataFig. 7 for GSM3168387 (RPFs range: 24-34 nt), GSM3168389 (RPFs

1621 range: 23-33 nt), and GSM3168390 (RPFs range: 23-35 nt).

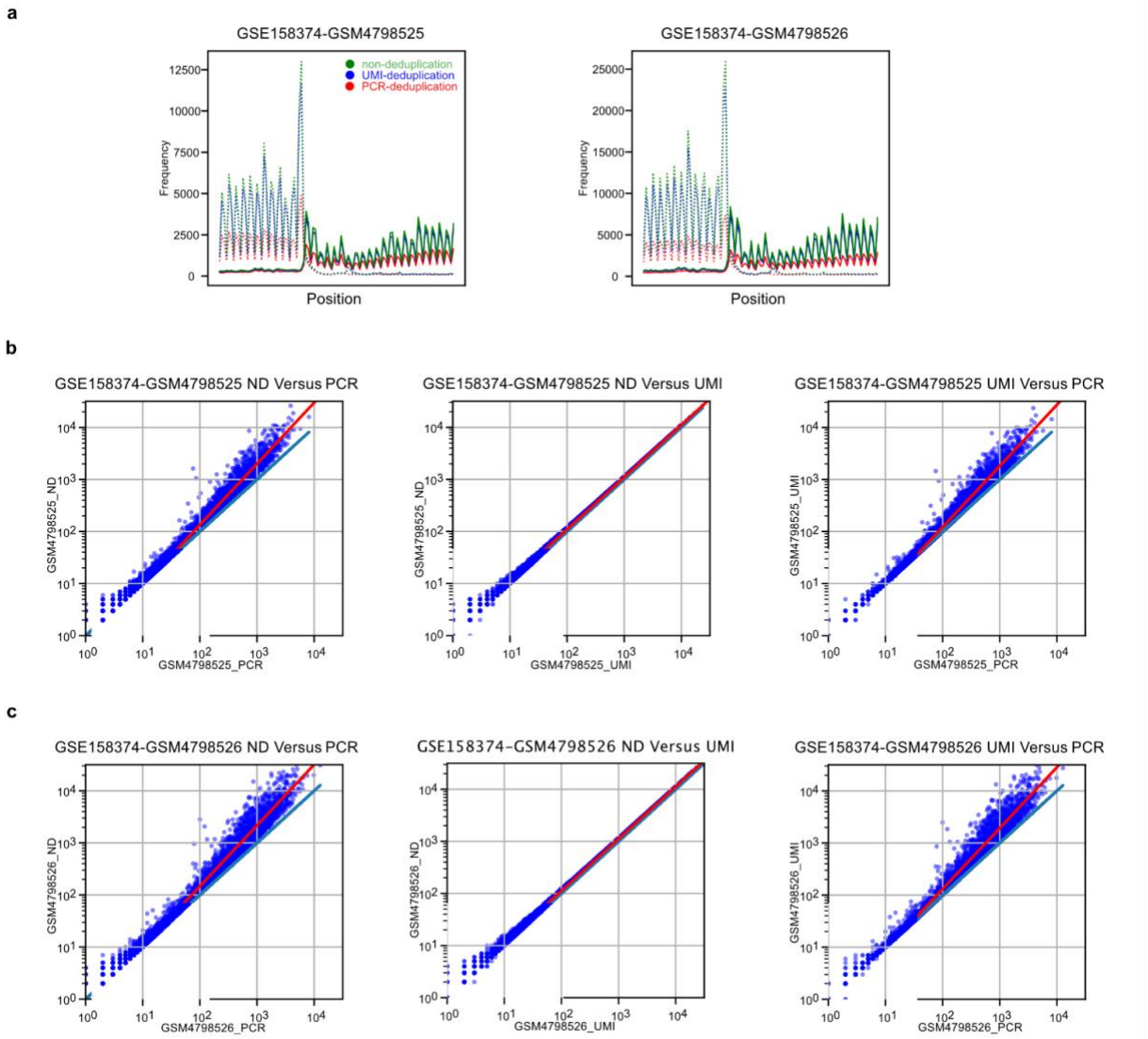

ExtendedDataFig. 11 | PCR vs. UMI deduplication comparison for GSE158374: Similar analysis as figure S7 and S8 for GSM4798525 and GSM4798526, both in the 28-32 nt RPFs range.

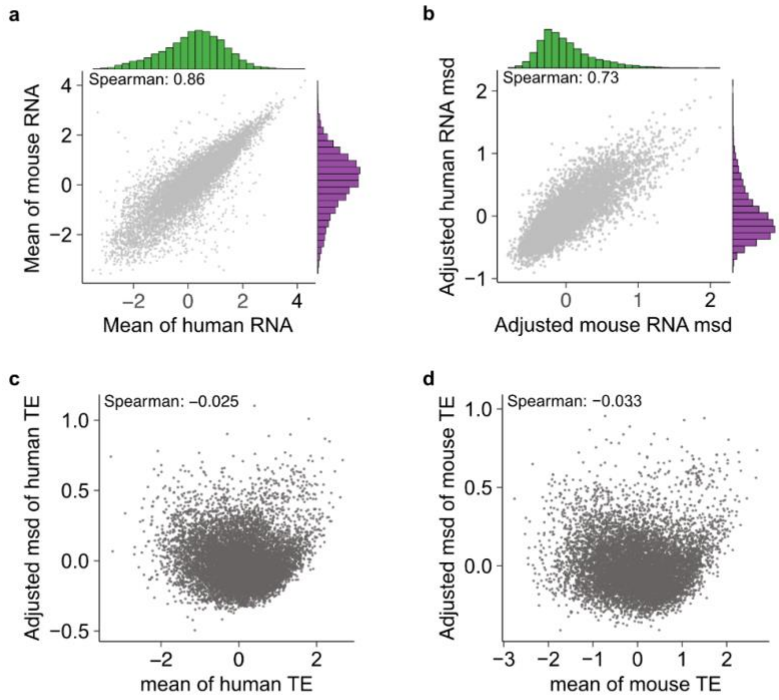

ExtendedDataFig. 12 | Conservation of gene expression between human and mouse: a, The relationship between the mean RNA expressions (clr-transformed counts) of 9,194 orthologous genes across two species is plotted. Dots represent genes in all figure panels. **b,** The variability of genes' RNA expression was quantified with metric standard deviation (msd; Methods) across different cell lines and tissues in either human or mouse. To account for the correlation between mean RNA expression and its variability, we adjusted the msd values with their mean values (Methods). **c,** The scatter plot shows the adjusted msd values (y-axis; Methods) and the average TE across different cell types (x-axis) for human genes. **d,** Similar analysis as in panel c for mouse genes.

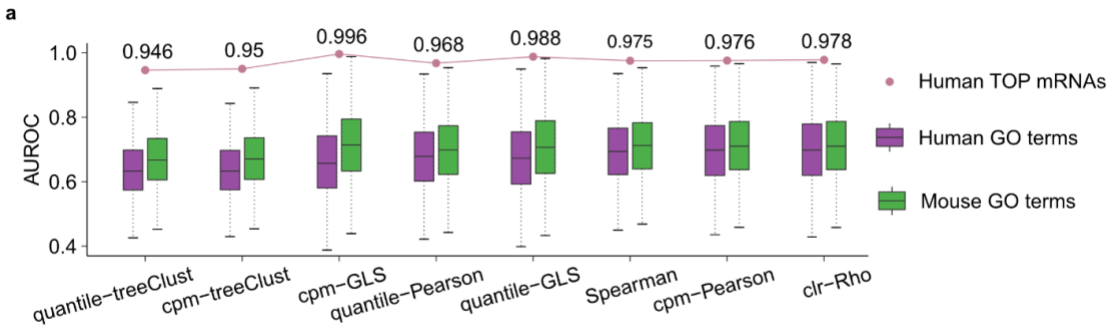

ExtendedDataFig. 13 | Evaluating the performance of eight methods to associate ribosome occupancy covariation with biological function: a, The AUROCs for biological functions were calculated using the similarity scores among genes at ribosome occupancy level determined by eight distinct methods (Methods). In the boxplot, the horizontal line corresponds to the median. The box represents the IQR and the whiskers extend to the largest value within 1.5 times the IQR from the hinge. The dot in this figure represents the AUROC for human 5' TOP mRNAs.

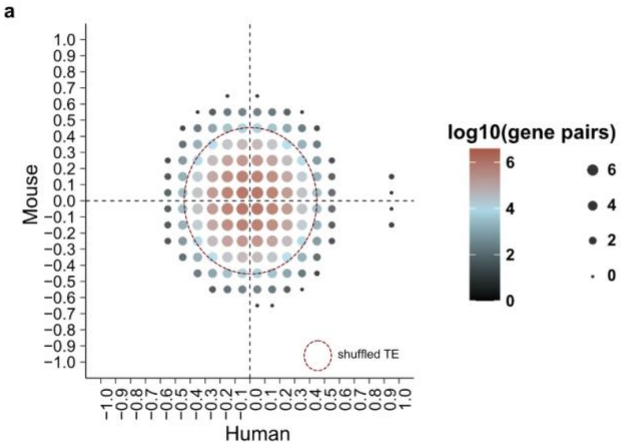

ExtendedDataFig. 14 | Lack of correlation in TEC across orthologous gene pairs between human and mouse using shuffled TE: a, TE values that were randomly reassigned from the original data for each gene (shuffled) and TEC was calculated. In the figure panel, we plotted the number of orthologous gene pairs within specified ranges. Each dot represents the aggregated $\log_{10}$-transformed counts of these gene pairs. The dashed line captures 95% of the data.

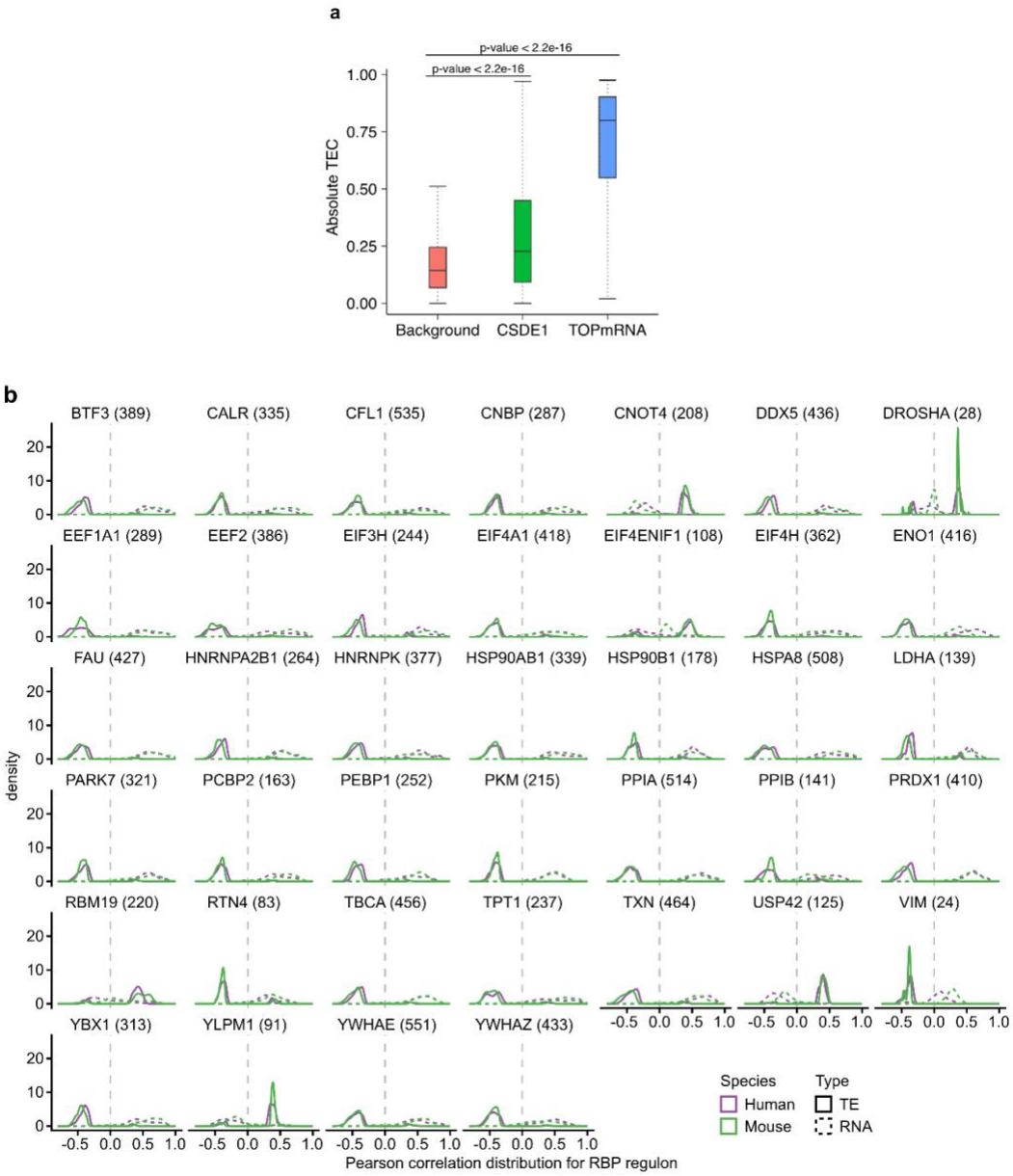

ExtendedDataFig. 15 | TE regulon correlation distribution for regulons with high TEC: a, Distribution of absolute TEC among 110 TOP motif-containing mRNAs[69] and 83 transcripts targeted by CSDE1 (table S6[39]) in comparison to all 11,149 human genes as background. Statistical significance between the groups was assessed using a Wilcoxon two-tailed test. **b,** Distribution of Pearson correlation coefficients between RBP RNA expression and TE of the conserved TE regulon are shown for RBP regulons with mean abs(TE rho) > 90th percentile. Ribosomal protein genes are omitted except for FAU, as a representative example. Numbers in parentheses denote the number of genes in the conserved RBP TE regulon.

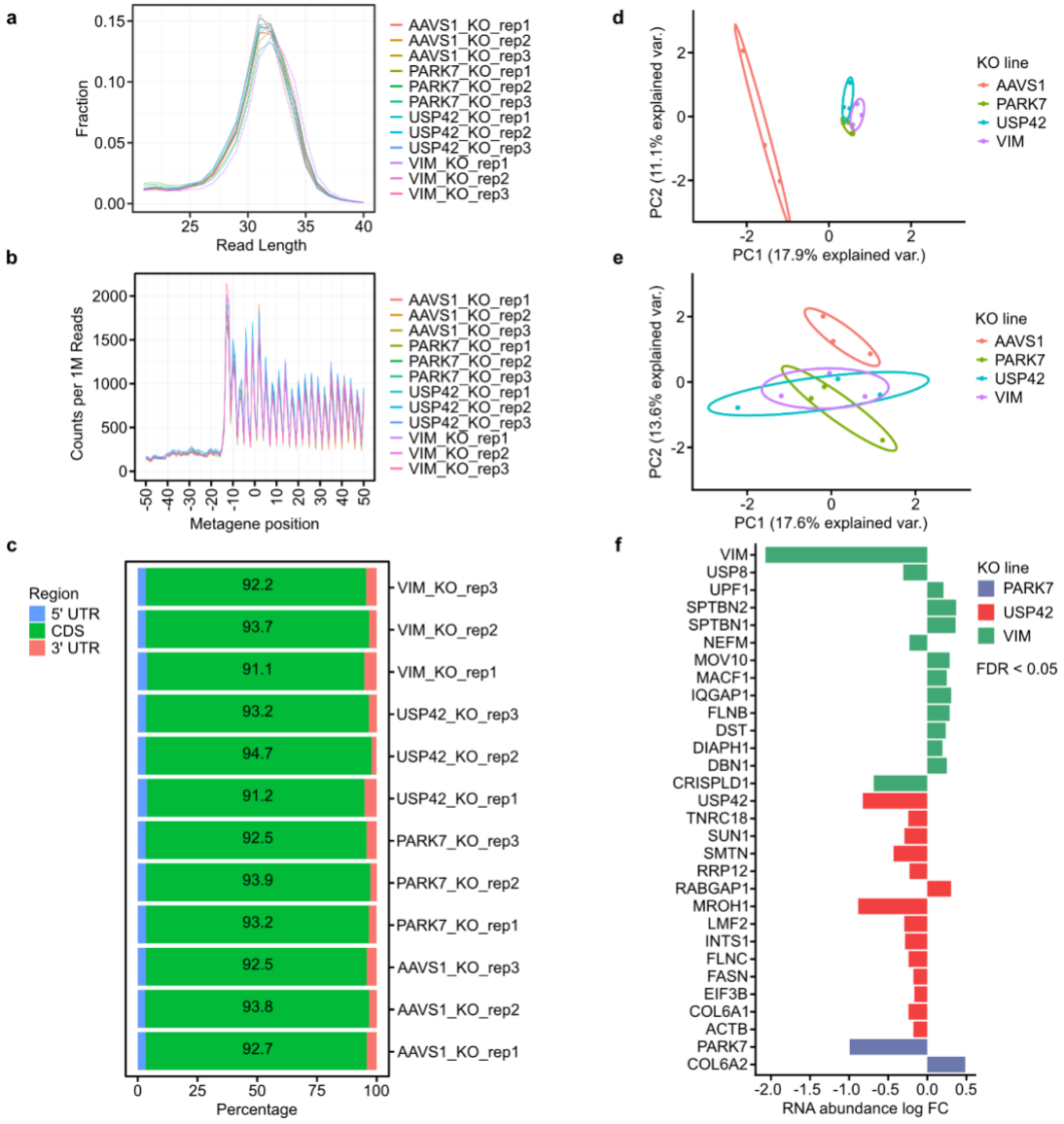

ExtendedDataFig. 16 | Ribosome profiling and RNA-seq of RBP KO cell lines: For b through e, ribosome footprints between 28 and 35 nt were used. **a,** Read length distributions of ribosome footprints. **b,** Metagene plot at the start site. **c,** Location of mapped ribosome footprints. **d,** PCA was performed on standardized CPM reads for transcripts whose sum of CPMs across cell lines and replicates is in the top 80th percentile. PCA of RNA-seq counts. **e,** Same as D for ribosome profiling read counts. **f,** Differential RNA expression of KO cell lines. A significance threshold of FDR < 0.05 was used.

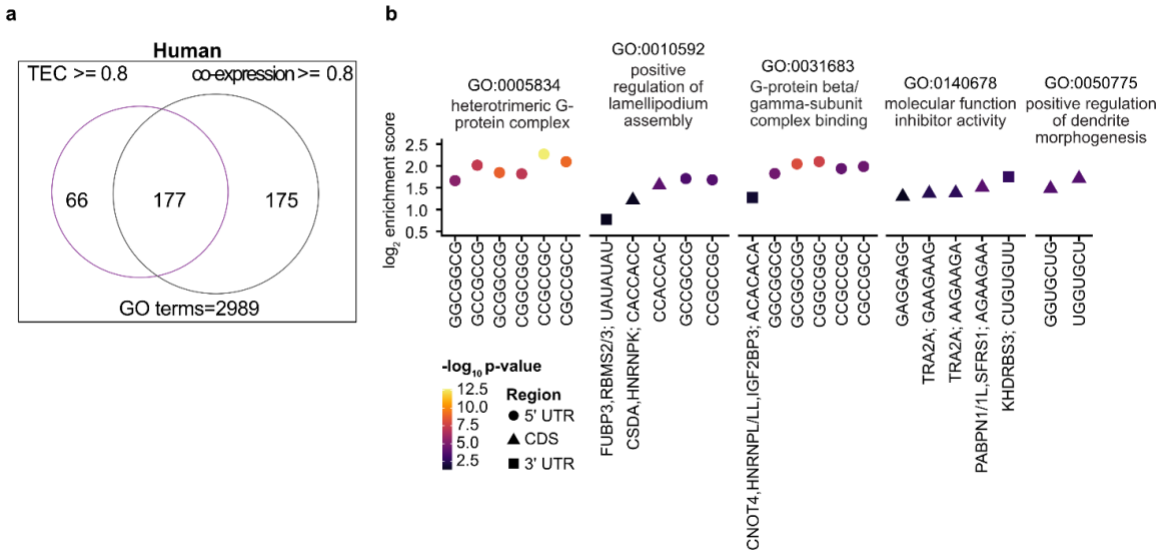

ExtendedDataFig. 17 | TEC and RNA co-expression among genes with shared functions in human: a, A comparison between the number of human GO terms that have AUROC of 0.8 or higher with either TEC or RNA co-expression. **b,** Motif enrichment in human GO terms. RNA binding proteins (RBPs) from oRNAment[80] or Transite[81] are indicated. P-values were corrected using the Holm method and those kmers with a p-value < 0.05 are shown.

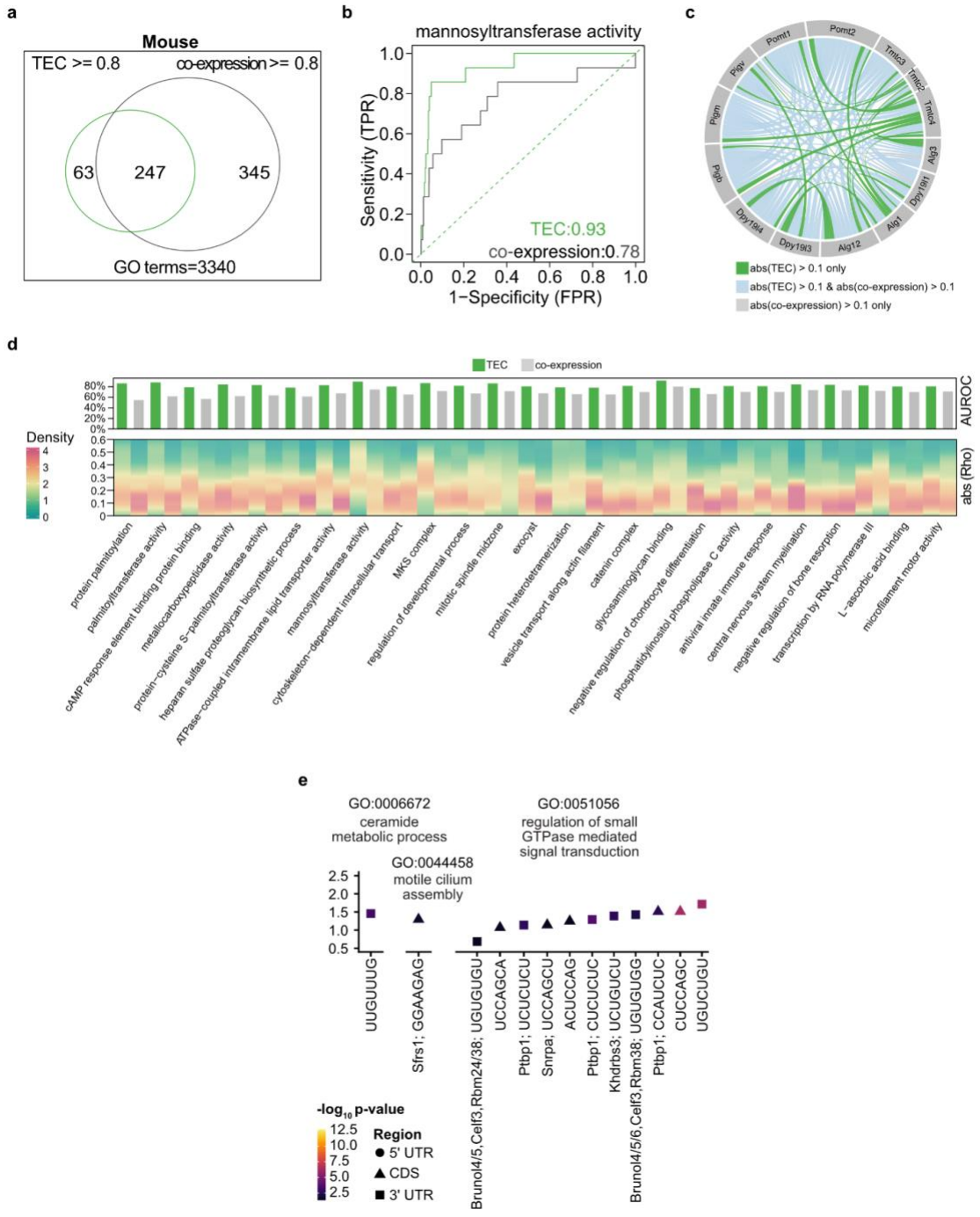

ExtendedDataFig. 18 | TEC and RNA co-expression among genes with shared functions in mouse: a, Venn diagram for mouse GO terms that achieve an AUROC of 0.8 or higher with

proportionality scores (rho) among genes at either TE or RNA expression level. **b,** The AUROC plot was calculated with genes associated with mannosyltransferase activity in mice. **c,** The connections represent absolute rho values above 0.1 in either TE pattern alone (green), in both RNA co-expression and TE pattern (blue), or RNA co-expression alone (gray). **d,** We summarized GO terms where genes exhibit greater similarity at the TE level than at the RNA expression level (AUROC with TEC > 0.8, and different AUROC between TEC and RNA co-expression > 0.1) in mice. We visualized the distribution of absolute rho score for gene pairs within each specific GO term (bottom; gene pairs with abs(rho) > 0.1) at the TE level. **e,** Motif enrichment in mouse GO terms. RNA binding proteins (RBPs) from oRNAment[80] or Transite[81] are indicated. P-values were corrected using the Holm method and those kmers with a p-value < 0.05 are shown.

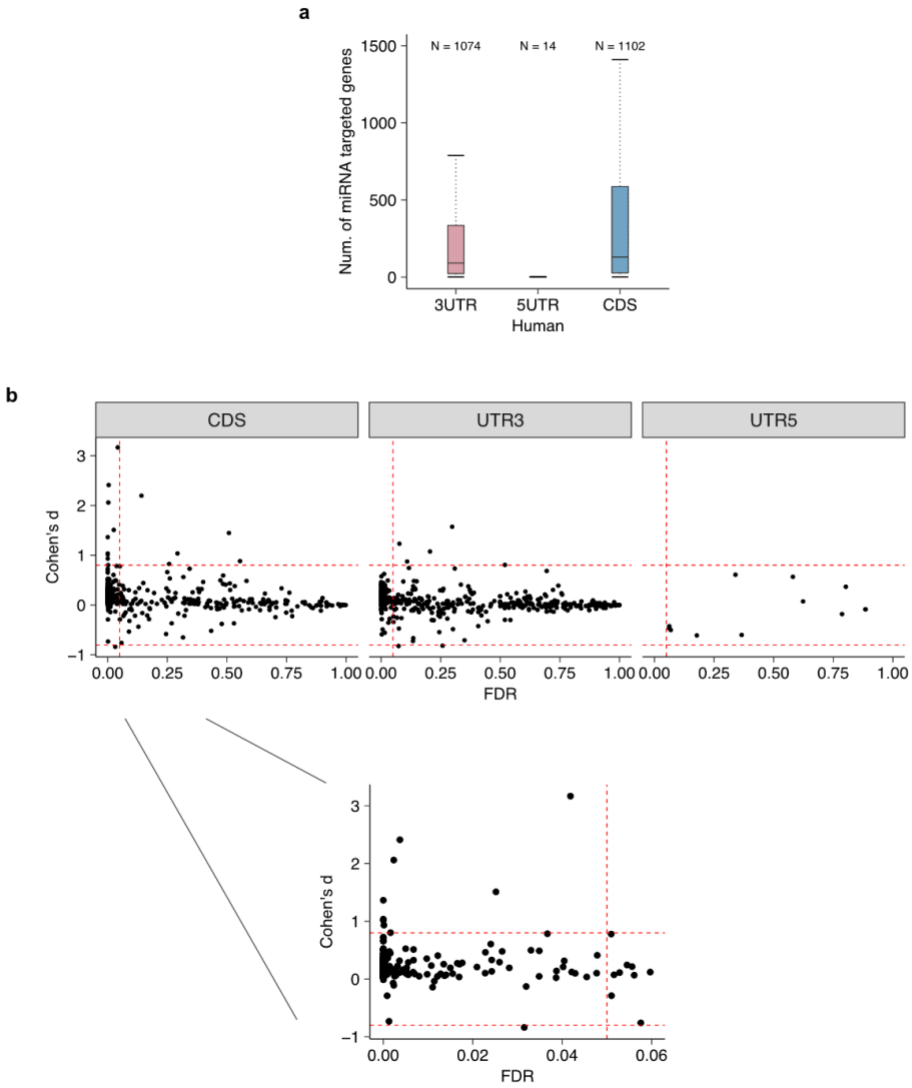

ExtendedDataFig. 19 | TEC is not primarily drive by shared miRNA binding sites: Experimentally validated miRNA targets within 3' UTR, 5' UTR, and CDS were downloaded from https://dianalab.e-ce.uth.gr/tarbasev9[174]. 11,134 out of 11,149 human genes in RiboBase had at least one miRNA binding site. **a,** The distribution of the number of human genes targeted by miRNAs grouped according to transcript region. We only included miRNAs targeting at least 3 genes. ***N*** indicates the number of miRNAs in each boxplot. **b,** The distribution of TEC among 11,134 genes was used as the background. For each set of genes with a shared miRNA-binding site, the distribution of their TEC was compared to the background using a Student's t-test. Given the large number of genes in the background distribution, we incorporated both a FDR (<0.05) and an effect size threshold (Cohen's d > 0.8).

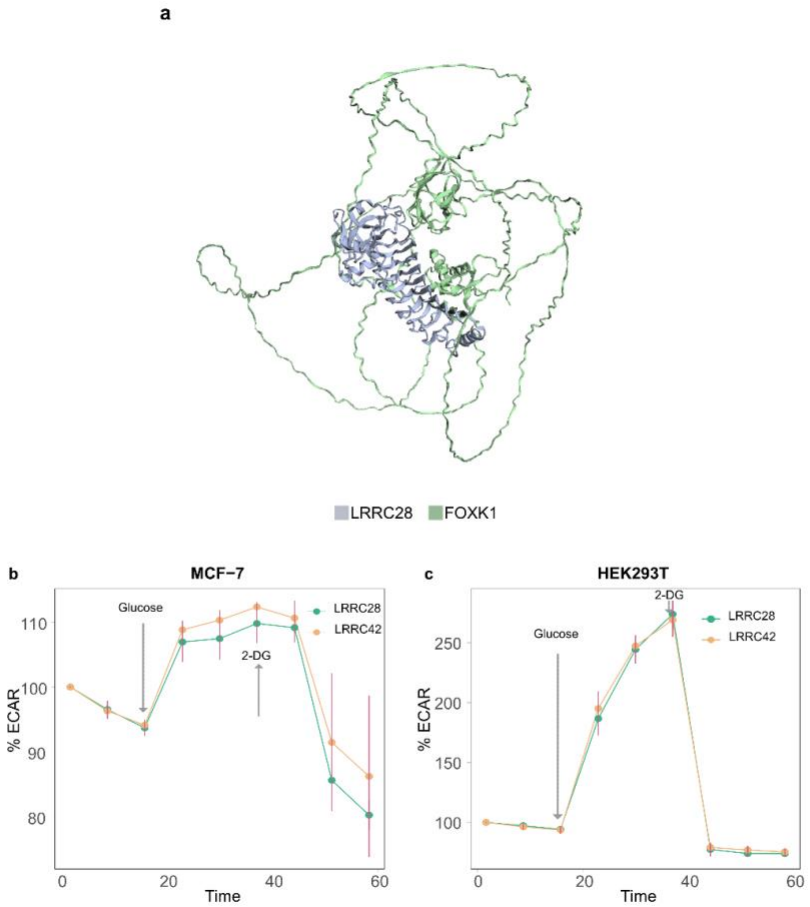

ExtendedDataFig. 20 | 3D structure of the interaction between LRRC28 with FOXK1: a, AlphaFold2-multimer predicted binding between LRRC28 and FOXK1. Kinetic ECAR response of **b,** MCF-7 cell line (n=6, stable overexpression) and **c,** HEK293T cell line (n=6; stable overexpression) overexpressing LRRC28 or LRCC42 to 10 mM glucose and 100 mM 2-DG.

Unpaired two-sided Student's *t*-test, ***$P < 0.005$, **$P < 0.05$. Panel g & h shows mean ± s.d.; *n* shows biological independent experiments.

Supplementary Text

1: Inaccurate and incomplete metadata examples from GEO

We observed recurrent issues regarding cell line identification in GEO. For instance, several studies categorize cell lines merely as "erythroid cells" without providing specifics. Similarly, descriptions of mouse embryonic stem cells (mESCs) often lack detail regarding subtypes, such as v6.5, which are either vague or missing. Inconsistencies in library strategies present additional challenges. While most researchers categorize ribosome profiling under OTHER in the library strategy, some entries label ribosome profiling as RNA-seq, ncRNA-seq, and miRNA-seq. Such nonstandard information leads to significant errors in large-scale data reanalysis, emphasizing the need for data curation.

2: Summary of sequencing quality for ribosome profiling and matched RNA-seq

The median number of reads for all human ribosome profiling samples was approximately 43.2 million, and after removing the adapter sequences the corresponding median was 35.5 million (ExtendedDataFig. 1a; table S2). For mouse samples, the median number of reads was around 37.5 million, compared to 29.7 million reads with adapters (ExtendedDataFig. 1a; table S3). On average, only 17% of reads could be aligned to the transcriptome, with 13% having a mapping quality higher than 20 in human samples (ExtendedDataFig. 1c). 5% of the total ribosome profiling reads were retained (ExtendedDataFig. 1c). The mouse data showed a similar trend, with 13% alignment, 10% above a mapping quality of 20, and 3% retention after PCR-deduplication (ExtendedDataFig. 1c).

Furthermore, in our comparative analysis between ribosome profiling and the corresponding RNA-seq data, we observed that ribosome profiling experiments were generally sequenced at a higher depth compared to RNA-seq. The median reads for ribosome profiling were 45.6 million for human experiments and 43.1 million for mouse experiments, compared to 36.2 million and 37.1 million reads for the matched RNA-seq, respectively (ExtendedDataFig. 1b; table S4-5). However, ribosome profiling demonstrated a lower alignment percentage to transcriptome than RNA-seq, with only 13% in human and 14% in mouse experiments, as opposed to 48% and 47% in RNA-seq for human and mouse samples, respectively (ExtendedDataFig. 1d). This discrepancy is explained by the substantial presence of ribosomal RNA in ribosome profiling samples.

3: Comparison of different methods for removing duplicated reads

Removing duplicated reads with the same position and length is commonly used in ribosome profiling data processing to minimize biases introduced by PCR amplification[54,71,175]. A key concern is the inadvertent removal of ribosome footprints that are identical in sequence and length but originate from different templates, leading to misinterpretation of the data. To evaluate the impact of deduplication strategies on ribosome profiling data, we analyzed samples that incorporated UMIs. Our findings indicate a significant loss of reads originating from unique molecules when using PCR deduplication based on position and fragment length (ExtendedDataFig. 9-11). This discrepancy was exacerbated in samples with higher coverage. Given the limited adoption of library preparation method that introduce UMIs in ribosome

profiling experiments, we used a winsorizing-based method to process non-deduplicated ribosome profiling sequencing data, aiming to mitigate this bias by capping excessively high-depth regions (Methods).

We compared linear regression-based TE calculated by winsorized non-deduplicated and PCR-deduplicated data. The winsorized method showed a slightly higher mean correlation than the PCR-deduplicated method (ExtendedDataFig. 8b), indicating the PCR-based deduplication approach, which relies on identical position and length, could obscure the actual biological insights obtainable from ribosome profiling.

4: RBPs may coordinate TEC

We identified RBP TE regulons in which the component genes had high TEC, as this might indicate an influence of the RBP on TE. Salient examples of RBPs which were previously linked to translation regulation and had conserved regulons with high TEC were VIM and PARK7 (also known as DJ-1). Although VIM is a primary component of intermediate filaments, its RNA expression was negatively correlated with TE of genes encoding proteins in the electron transport chain and ribosomal proteins. VIM was previously found to repress translation of the mu opioid receptor[70]. Similarly, expression of *PARK7* was predominantly negatively correlated with TE, in line with a prior study that PARK7 represses translation[176,177] (68% and 79% of regulon genes having negative correlations in human and mouse, respectively). There was not a significant overlap between PARK7 targets determined by RIP-seq analysis in human neuroblastoma cells[176] and the human or mouse PARK7 TE regulons (hypergeometric test p-values 0.84 and 0.23, respectively). Nevertheless, thirty-three PARK7 RIP-seq targets were present in both human and mouse regulons, including glutathione peroxidase 4 (*GPX4*), Sm-like proteins (*LSM1/3/5*), and six genes encoding ubiquinone-oxidoreductase subunits, indicating PARK7 regulates a diverse set of biological processes extending beyond the oxidative stress response. Among genes with positive correlations with PARK7 expression, subunits of calcium channels such as CACNB1 and CACNA2D1 were notable, consistent with data that PARK7 increases nascent protein synthesis of CACNA2D1 despite not significantly binding it[177]. Altogether, these data suggest largely indirect influences of PARK7 on TE, and possibly a smaller set of direct target genes.

We selected VIM, PARK7, and USP42 for further experiments, as their regulons exhibited distinct correlation distributions for RNA expression and gene TE (ExtendedDataFig. 15b) and are not essential genes, facilitating knockout experiments. These RBPs had high HydRA[178] scores (>0.89, scale 0 to 1) and detectable RNA binding domains, supporting their role as *bona fide* RBPs. Knockout of these RBPs and subsequent matched ribosome profiling and RNA-seq (ExtendedDataFig. 16a-e, Methods) indicated no changes in TE for the genes in these RBPs' TE regulons, with one exception (*VIM* KO led to lower *VIM* TE). However, we found a small subset of genes with altered RNA abundance upon knockout of each RBP (ExtendedDataFig. 16f). For example, knockout of *VIM* led to increased RNA abundance of several genes involved in cytoskeletal function, including *SPTBN1*, *SPTBN2*, *MACF1*, *IQGAP1*, *FLNB*, *DST*, *DIAPH1*, and *DBN1*.

We note that the lack of genes with significantly altered TE upon KO of these RBPs may be due

to several reasons: 1) these RBPs may exert an indirect- rather than direct- influence on TE, 2) the associations between RBP expression and gene TE were identified across diverse cell lines, whereas the association was only tested in the HEK293T cell line; 3) use of heterogenous knockout populations (not single clones), and limited efficiency of knockout as measured by the observed RNA-seq fold changes (*PARK7*: 0.37, *USP42*: 0.44, *VIM*: 0.13) may limit sensitivity to observe effects on TE. Further work will be needed to validate the role of PARK7, USP42, and VIM on translational regulation.

5: TEC among genes is associated with shared biological functions in mouse

We identified 25 GO terms including protein palmitoylation, palmitoyltransferase activity, and metallocarboxypeptidase activity which exhibited AUROC scores that were at least 0.1 lower at the RNA expression level compared to the TE level (AUROC calculated with TEC > 0.8; ExtendedDataFig. 18). For example, mannosyltransferase activity demonstrated a significant difference between the two levels (ExtendedDataFig. 18c). This difference was further highlighted by the observation that 22 gene pairs in this biological function had absolute rho above 0.1 exclusively at the TE level, compared to only two at the RNA expression level for this term (ExtendedDataFig. 18d). In summary, we found genes from certain biological functions are more likely to be regulated at the translational level rather than the transcriptional level, in both humans and mice.

We predicted novel functions for genes associated with 31 mouse GO terms. These predictions are based on either significant covariation in TE greater than RNA expression (AUROC measured with TEC > 0.8; different AUROC measured with TEC and RNA co-expression > 0.1; table S16; Methods) or new functional predictions were only achievable with TEC (AUROC measured with TEC > 0.8, difference AUROC measured with TEC and RNA co-expression < 0.1, ranking of the predicted gene with RNA co-expression < top 50%; table S16; Methods). For instance, we identified Cenpf as highly correlated with the function of mitotic spindle midzone. This aligned with findings in human cell lines, where CENP-F has been observed assembling onto kinetochores at late G2 and detected at the spindle midzone during anaphase[161]. Another prediction linked Arhgap31 with the antiviral innate immune response. This prediction has been supported by previous research that has recognized the ARHGAP family as novel biomarkers associated with immune infiltration[168].

6: Impact of low expression on TE calculation

The canonical ratio method of calculating TE leads to biased estimates especially for genes with low RNA expression or ribosome occupancy[55]. To highlight differences between our approach based on compositional regression and the conventional log-ratio, we provide several toy examples in table S19.

To characterize the influence of mRNA expression levels on TE with the real data, we examined the Spearman correlation between mRNA expression and our TE across 11,149 human genes, and found that only 947 genes showed a significant correlation (FDR < 0.05 and absolute correlation > 0.5). We found no evidence of lower mRNA expression for the 947 genes with significant TE-RNA correlations compared to the remaining genes (Wilcoxon one tailed p-value = 1). In contrast,

with the log-ratio method, the mRNA expression distribution for the 1547 genes with a significant correlation between TE and RNA levels had lower RNA abundance compared to the remaining genes, which demonstrated significant difference (Wilcoxon one tailed p-value < 2.2e-16). Hence, the significant correlations for the compositional TE method are more likely driven by biological factors rather than low mRNA expression abundance.

We next compared the interaction between RNA levels and TE in relation to protein abundance. We applied a general linear model to analyze protein abundance in HEK293 cells (protein abundance ~ RNA expression * TE). We found the contribution of TE and mRNA expression to protein level is independent when TE is derived with the compositional regression method (p = 0.228; table S20). In contrast, using the canonical method, the interaction was statistically significant (p = 0.0145; table S20). This result further highlights the non-independence of TE and RNA as calculated using the canonical log-ratio method.

Zeros in bulk sequencing data represent either true biological absence or extremely low expression. In our analysis, we replaced zeros with the lowest read count (Methods). To evaluate the robustness of our TE calculations to zero imputation, we compared our method with two alternatives from zCompositions library (Methods). We found strong consistency across different zero imputation methods (ExtendedDataFig. 21a; median Spearman correlation between our method vs.Geometric Bayesian-Multiplicative is 0.96, and vs. Square-root Bayesian-Multiplicative is 0.95 in human datasets). TEC values were also strongly correlated (Spearman correlation between our method with Geometric Bayesian-Multiplicative method is 0.87, and with Square-root Bayesian-Multiplicative is 0.75). Furthermore, zero imputation methods had minimal impact on analyses presented in Fig. 4a (ExtendedDataFig. 21b-c; Spearman correlation between our method vs. Geometric Bayesian-Multiplicative is 0.87, and vs. Square-root Bayesian-Multiplicative is 0.79). These results suggest that the choice of zero imputation method does not significantly alter our findings. We have provided TE and TEC matrices generated using the Geometric Bayesian-Multiplicative and Square-root Bayesian-Multiplicative methods as supplementary resources for future research (https://zenodo.org/uploads/14270998).

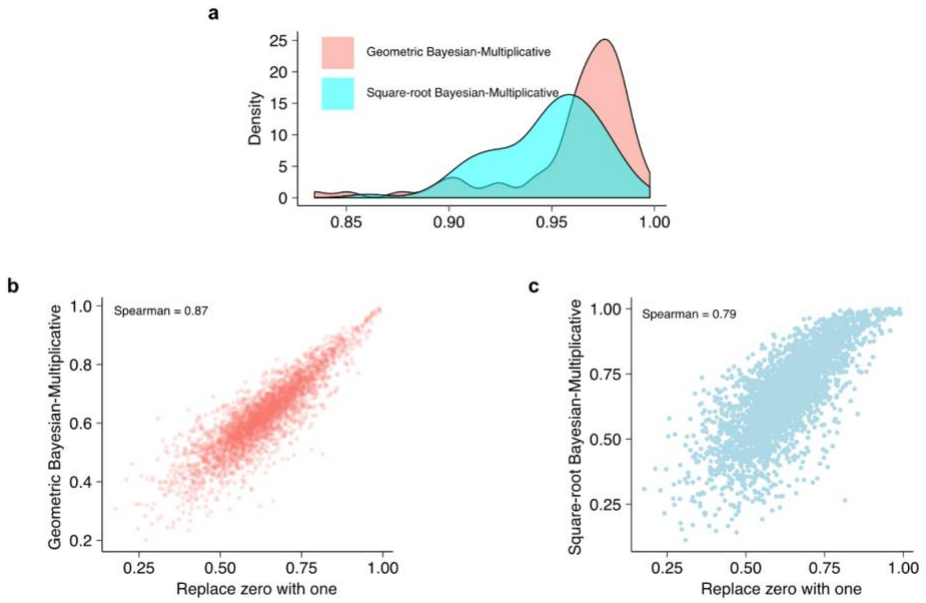

ExtendedDataFig. 21 | Zero imputation methods comparison: a, Spearman correlation distribution for compositional TE across human cell lines and tissues comparing the current zero imputation method with two alternative methods. **b,** Spearman correlation of AUROC for biological functions between the current zero imputation method with Geometric Bayesian-Multiplicative method and **c,** Square-root Bayesian-Multiplicative method.

7: Sequence features that influence TEC

In the accompanying manuscript by Zheng et al.[109], we have demonstrated high accuracy in predicting TE from mRNA features. Analogously, RNA expression can be accurately predicted from genomic sequences[179,180], yet predicting RNA co-expression using genomic features remains far more challenging. Coexpression is strongly influenced by chromatin interactions rather than sequence features alone[181]. For example, using Hi-C data to infer chromatin architecture can significantly improve prediction of RNA co-expression patterns[182].

To identify the potential features that may affect TEC, we tested the association between several mRNA/protein features and TEC. First, using protein domain data from the Pfam database[183], we found that gene pairs sharing the same domains exhibit significantly, though modestly, higher positive TEC (Wilcoxon p-value < 2.2e-16; ExtendedDataFig. 22a). Second, we calculated pairwise sequence similarities between all transcripts as follows. Pairs of sequences were aligned using the Biopython (v1.84) PairwiseAligner module implementing the Gotoh algorithm[184]**.** Score parameters of match=5, mismatch=−4, gap open=−10, and gap extend=−0.5 were used. Using the highest scoring alignment, percent identity was then calculated as the number of matched

nucleotides divided by total alignment length. Transcripts with shared biological functions and high TEC tended to have significantly higher sequence similarity (ExtendedDataFig. 22b-c). However, overall, TEC and sequence similarity were not significantly correlated. (Spearman correlation rho: 0.023; ExtendedDataFig. 22d).

The region lengths and sequence composition of mRNAs are predictive of TE[109]. To test their relevance to TEC, we calculated the absolute difference and mean GC percentage and lengths for the 5′ UTR, 3′ UTR, and CDS between transcript pairs. However, none of these features were significantly associated with TEC (ExtendedDataFig. 22e–l). Similarly, amino acid-level features are predictive of TE[109]. Therefore, we examined protein features, including the absolute difference and mean percentage of hydrophobic amino acids (A, V, I, L, M, F, W, P, G, C), isoelectric point (pI), and charge across gene pairs. None of these features showed a significant correlation with TEC (ExtendedDataFig. 23a–f). Taken together, our new analyses indicate that TEC is not strongly associated with simple mRNA or protein features of gene pairs.

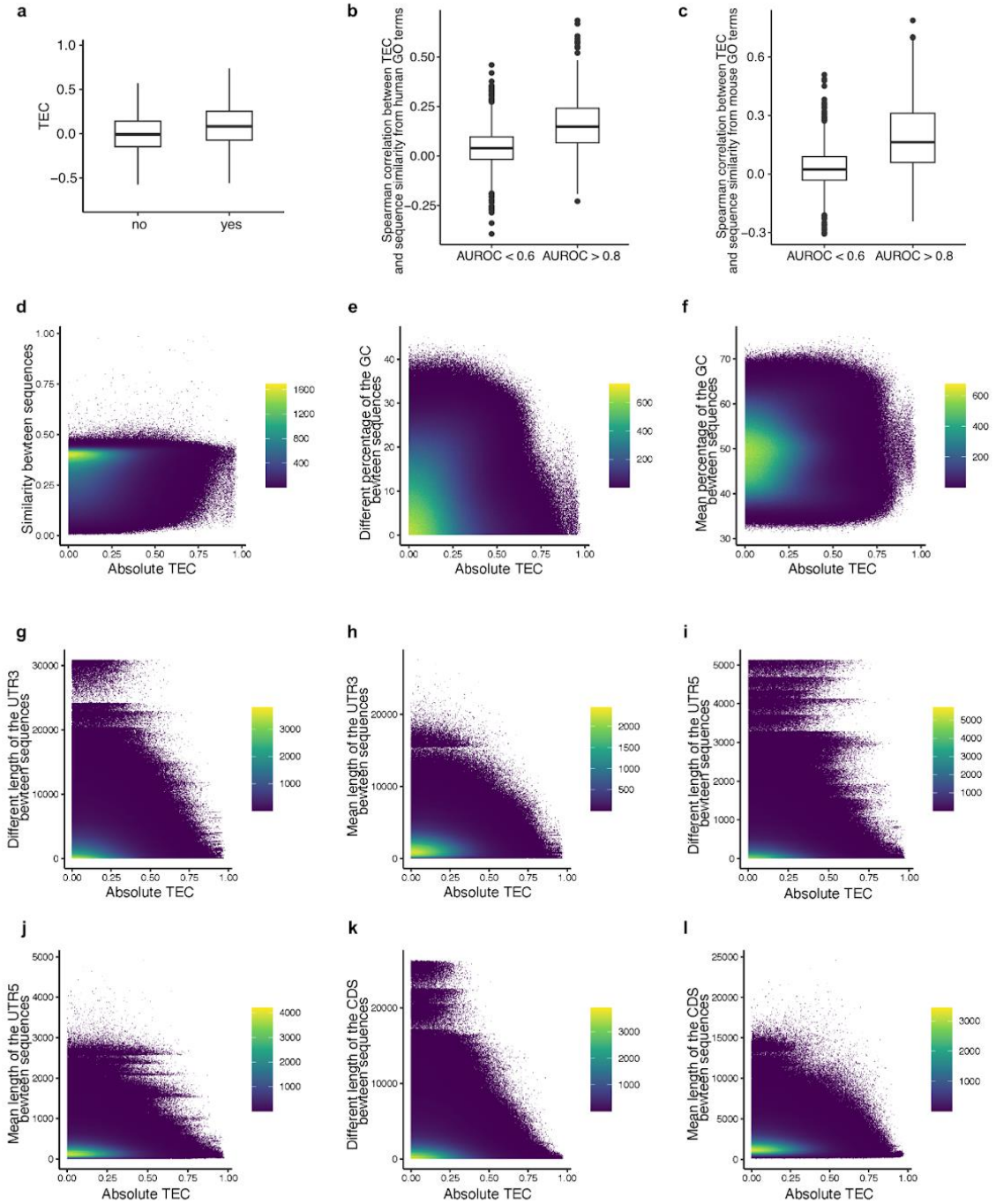

ExtendedDataFig. 22 | Correlations between genomic features and TEC: a, TEC distribution of human gene pairs that either share the same protein domain or do not. **b,** Correlation between absolute TEC and sequence similarity for gene pairs within human biological functions; **c,** within mouse biological functions. **d,** Correlation between absolute TEC and sequence similarity among

human gene pairs. **e,** Correlation between absolute TEC and the absolute difference in GC percentage between human gene pairs; **f,** and the mean GC percentage. **g,** Correlation between absolute TEC and the absolute difference in length of 3'UTR between human gene pairs; **h,** and the mean in length of 3'UTR. **i,** Correlation between absolute TEC and the absolute difference in length of 5'UTR between human gene pairs; **j,** and the mean in length of 5'UTR. **k,** Correlation between absolute TEC and the absolute difference in length of CDS between human gene pairs; **l,** and the mean in length of CDS. In figure panel d-l, we visualized the correlation between these features and TEC using a bin size of 1000.

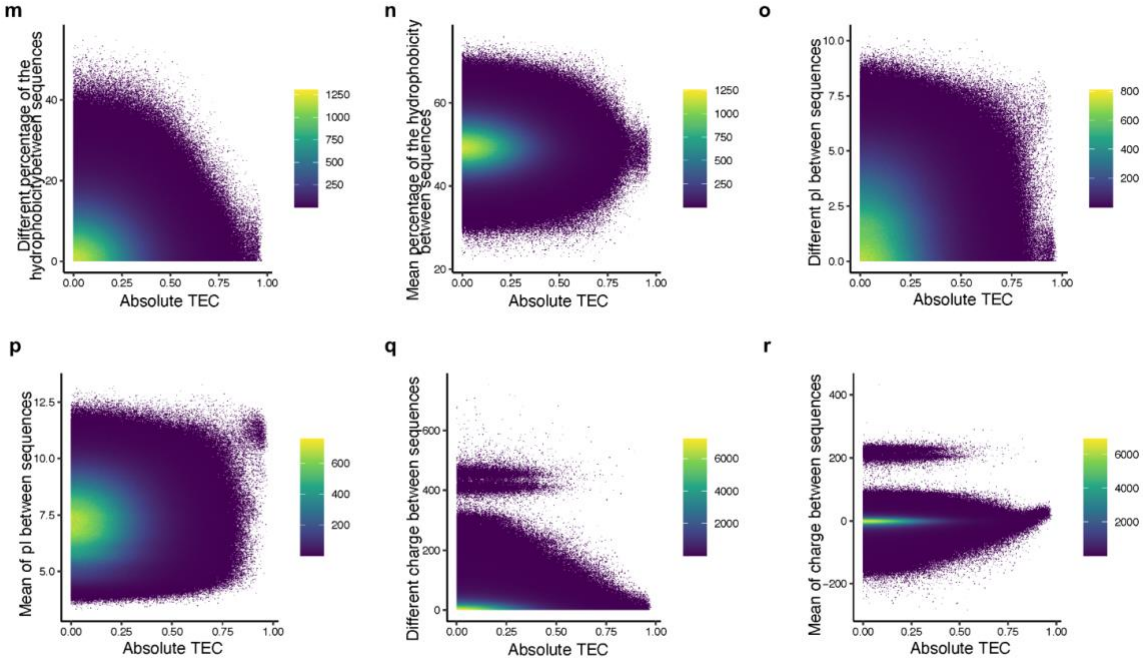

ExtendedDataFig. 23 | Correlations between protein features and TEC: a, Correlation between absolute TEC and the different percentage of hydrophobic amino acids between human gene pairs; **b,** and the mean percentage of hydrophobic amino acids. **c,** Correlation between absolute TEC and the different pI between human gene pairs; **d,** and the mean of pI. **e,** Correlation between absolute TEC and the different charge between human gene pairs; **f,** and the mean charge. In this figure, we visualized the correlation between these features and TEC using a bin size of 1000.